I. SOLUBILITY AND BLEND STUDIES OF NITROCELLULOSE
II. RELAXATION PROPERTIES OF THIN FILM COATINGS: THE ROLE OF SURFACE TOPOGRAPHY

by

Eduardo Balcells

Thesis submitted to the Faculty of the
Virginia Polytechnic Institute and State University
in partial fulfillment of the requirements for the degree of

MASTER OF SCIENCE

in

Chemistry

APPROVED :

T.C. Ward, Chairman

J.D. Graybeal

J.P. Wightman

July, 1988
Blacksburg, Virginia

I. SOLUBILITY AND BLEND STUDIES OF NITROCELLULOSE

II. RELAXATION PROPERTIES OF THIN FILM COATINGS: THE ROLE OF SURFACE TOPOGRAPHY

by

Eduardo Balcells

Committee Chairman: T. C. Ward

Chemistry

(ABSTRACT)

In the first part of this two part thesis, interaction parameters of nitrocellulose with various solvent systems were investigated by Inverse Gas Chromatography. From these data, the solubility parameters of nitrocellulose were determined at a series of nitration levels which were used to guide the selection of suitable plasticizers for nitrocellulose films. Subsequent dynamic mechanical experiments were then used to evaluate the effectiveness of the blend formulations in broadening the glass transition dispersion of the nitrocellulose blended films; in addition, stress-strain experiments were done in order to evaluate the tensile modulus of the nitrocellulose blends.

In the second part of this thesis, both dynamic mechanical thermal analysis and dielectric thermal analysis were used to evaluate the relaxation properties of thin film polysulfone coatings and the effect of substrate surface topography on these properties. Both dynamic mechanical and dielectric thermal analysis revealed that the topographical nature of the substrate influenced the linear viscoelastic properties of the thin film coatings and that the extent of this influence was dependent on the coating thickness.

ACKNOWLEDGEMENTS

The completion of this graduate coursework was made possible by the encouragement and assistance of several friends and family members. Those who have my sincere gratitude and esteem are:

Dr. Thomas C. Ward, my graduate advisor, who not only gave me the opportunity and guidance for my graduate studies, but who more importantly served and will continue to serve as a role model for character both as a professional and fellow human being;

Dr. James P. Wightman and Dr. Jack D. Graybeal for serving on my committee and providing guidance in my research;

Mia Siochi, for her friendship and whose generous assistance in typing this thesis will not be forgotten;

Chan Ko, for his collaboration in parts of the research presented and for his expertise on surface analysis;

Erick Grumblatt, for his friendship and support, and for always being there when I needed a BREAK;

and my family, especially:

My beautiful wife Giuliana C. Balcells, who has shared my entire experience and made the good times better and the difficult times bearable;

Mi madre Cecilia, por su amor, prayers, support, que siempre a estado foremost en qualquer endeavor que he hecho.

TABLE OF CONTENTS

LIST OF FIGURES

LIST OF TABLES

CHAPTER 1

INTRODUCTION

The research presented herein is composed of two distinct projects. Chapters 2 and 3 are concerned with solubility and blend studies of nitrocellulose, respectively, while Chapter 4 deals with the relaxation properties of thin film coatings. While no attempt was made to couple these two projects, the research presented in this thesis is generally focused on the relaxation properties of polymer films and coatings with the chapter on the solubility parameter being a complementary study to the work presented in Chapter 3. The work in Chapters 2 and 3 was supported by both Hercules Inc. and the Naval Surface Weapons Center which developed from interest in the mechanical properties of nitrocellulose based propellants.

Nitrocellulose (NC) propellants are generally divided into three categories depending on their composition: single based, double based, and triple base. The single based propellants contain mainly NC with stabilizer; the double based materials contain mainly NC and nitroglycerine (NG) - with stabilizer; and the triple based propellants contain nitroguanidine in addition to NC and NG - with stabilizers (1). In all the formulations the propellant is usually blended with plasticizers that act to reduce the brittleness of the propellant material. These plasticizers can be low molecular weight compounds or high molecular weight polymers, and must be miscible with the NC over a given concentration and temperature range. In addition, the plasticizers should allow for uniform plasticity over a range of temperatures. Indeed, one of the chief concerns related to the physical stability of double based propellants is the thermal variations experienced by the propellant material. This environment requires that the propellant be neither too brittle nor too soft when exposed to thermal extremes. The work in Chapter 3 was aimed at investigating various blend formulations (based on propellant grade nitrocellulose) that would exhibit plasticity over a broad temperature range. In the study, nitrocellulose was blended with both low and high molecular weight

(polymeric) plasticizers, and the viscoelastic properties of these films were studied over a temperature span of 100 ^{o}C.

The work in Chapter 2 complements the work done in Chapter 3 in that the solubility parameter of NC and the effect of nitration level on this parameter was studied. Since propellant grade nitrocellulose is thermally unstable -with denitration occurring during prolonged exposure to elevated temperatures- an understanding of how the solubility parameter varies as decomposition proceeds is important. Consequently, the work presented in Chapter 2 dealt with nitrocellulose samples of varying high nitration levels.

The last chapter in this thesis deals with the viscoelastic properties of thin film coatings. The work, which was partially supported by the Adhesive and Sealant Council, was aimed at understanding the "interphase" properties of adhering systems. The interest in this work arose from the fact that many failures occur either at or near the interface of an adhesive joint; hence, some researchers have suggested that the interphase should be modelled as a separate material (2). If the viscoelastic properties of an adhesive are different in or near the interphase these differences must be understood since the viscoelastic nature of an adhesive influences the failure modes (adhesive or cohesive) of an adhesive joint. Moreover, the influence of the adherend surface should be considered since the adhesive substrate is usually pretreated in some manner.

In an attempt to understand the viscoelastic properties of an adhesive near the interface, thin film coatings of polysulfone onto aluminum were investigated by dynamic mechanical thermal analysis and dielectric thermal analysis. Polysulfone was selected as the thermoplastic adhesive since it is totally amorphous and is commercially available. In addition, it was well suited for the dielectric studies due to the polar sulfone groups. Aluminum was considered as the coating substrate since it can be readily pretreated and has a stable oxide (Al_2O_3) that has been well characterized (3). The pretreatments used were vapor degreasing and phosphoric acid anodization. The objective of the pretreatments was to obtain two substrate surfaces with different surface

topographies which would allow for the investigation of the role of surface topography on the viscoelastic properties of the coatings. Phosphoric acid anodization is known to generate wide pore structures on the aluminum surface and an overall rougher surface than other anodizations such as a sulphuric acid anodization (4); while the vapor degreasing pretreatment should yield a smooth surface. While the objective of the pretreatments was to generate topographically different surfaces, it was understood that the pretreatments also lead to other changes in the aluminum surface which could not be factored out of the study . For instance it is known that the surface free energies of an anodized aluminum surface and a solvent extracted aluminum surface can be very different, with the surface free energy of a hexane extracted aluminum surface being 49.5 mJ/m^2 and that of an anodized aluminum surface being 151.6 mJ/m^2 (5). While the study presented in Chapter 4 focused soley on the effect of surface topography on the relaxation properties of the thin film coatings, it does include some surface characterization that supplements the investigation.

Realizing that the problem at hand was multifaceted, a synergistic approach was taken in Chapter 4. The surface characterization was done by Chan Ko of Dr. J.P. Wightman's group. Included in the surface analysis was X-ray photoelectron spectroscopy (XPS) and high resolution scanning electron microscopy (HSEM). XPS was used to investigate the chemical nature of the polysulfone-aluminum oxide interface, while SEM was used to elucidate the morphological features of the polysulfone films (coatings) and the topographical features of the aluminum surface.

It is fortunate that the above oppurtunity for a combined study was possible. In the area of adhesion such an approach is necessary due the complexity of the factors that are pertinent to this area. This interdisciplinary approach has been encouraged by the Center for Adhesion Science here at Virginia Polytechnic Institute and State University and has provided its members with a broad exposure to the practical and fundamental elements of adhesion science.

REFERENCES

1. Radford Arsenal and Ammunition Plant , In House-Report.
2. Brinson, H.F., Class Notes, ESM 5650, Virginia Polytechnic Inst. and S. U., 1986.
3. Boerio, F.J. and Gosselin, C.A., "Polymer Characterization: Spectroscopic, Chromatographic, and Instrumental Methods", Craven, C.D. (Ed.), American Chemical Society, Washington D.C., 54, 1983.
4. Arrowsmith, D.J. and Clifford, A.W., Int. J. Adhesion and Adhesives, 3(4), 193, 1983.
5. van Ooij, W.J., Class Notes, ESM 5650, Virginia Polytechnic Inst. and S. U., 1986.

CHAPTER 2

SOLUBILITY PARAMETERS OF NITROCELLULOSE

2.1 LITERATURE REVIEW

2.1.1 Hildebrand Solubility Parameter

2.1.1.1 Concept

The solubility parameter concept was first introduced by Hildebrand and Scott in the 1920's. It arose from the idea that the solubility of a solute in a given solvent was dependent on the cohesive energy densities (e_{coh}) of each, a quantity related to the internal pressure of a system $(\partial U/\partial V)_{P,T}$. The square root of e_{coh} is the Hildebrand solubility parameter. From the "like" dissolves "like" formalism, Hildebrand proposed that the solubility of a given polymer in a given solvent is favored if the solubility parameters are equal. It was not until 1955 that Burrell recognized the usefulness of the solubility parameter and introduced it to the field of polymer science (1). Since then it has been widely used as a predictive tool in many areas of science.

The Hildebrand solubility parameter can be defined as

$$\delta^2 = \frac{\rho}{M}(\Delta H_v - RT) \qquad [2\text{-}1]$$

where ρ is the density, ΔH_V is the heat of vaporization and M is the molecular weight. Its dimensions are $(\text{energy/volume})^{1/2}$ and the units are either reported as $J^{1/2}/cm^{3/2}$ or $cal^{1/2}/cm^{3/2}$, the latter commonly referred to as Hildebrand units, H. Using Equation 2-1 the solubility parameter of a volatile compound, δ_1, can be readily determined from its heat of vaporization at the desired temperature. For high molecular weight compounds such as polymers, the measurement of ΔH_V is not possible and indirect methods are usually utilized for the determination of δ (eg. swelling and dissolution experiments). The technique of Inverse Gas Chromatography is one of the few techniques that does allow for direct determination of δ_2, the solubility parameter of the polymer.

The Hildebrand solubility parameter was initially intended only for non-polar, non-ionic, non-associating liquid systems which formed "regular solutions" (2). For such binary solutions, Hildebrand and Scatchard related the solubility parameters to the heat of mixing per unit volume as

$$\Delta H_m = \Phi_1 \Phi_2 (\delta_1 - \delta_2)^2 \qquad [2\text{-}2]$$

where Φ_1 and Φ_2 are the volume fractions of component 1 and 2, respectively (3). When δ_1 equals δ_2 maximum solubility is predicted, which from Equation 2-2 results in ΔH_m being equal to 0; hence, the thermodynamic potential responsible for mutual solubility is a negative combinatorial entropy term. This is one of the deficiencies of the solubility parameter theory as applied to polymer-polymer systems, for which the combinatorial entropy term is small and miscibility is mainly governed by enthalpic factors. In this case, the solubility parameter theory is limited since it predicts a heat of mixing equal to zero when δ_2 is equal to δ_3 (throughout the text the subscript 1 refers to solvent, while 2 and 3 refer to polymers).

In light of the significance of specific intermolecular interactions for solubility, Hansen and Beerbow have expanded the one dimensional Hildebrand solubility parameter model to a "three dimensional" definition given below:

$$\delta^2 = \delta_d^2 + \delta_p^2 + \delta_h^2 \qquad [2\text{-}3]$$

where the subscripts d, p and h refer to the dispersion, polar and hydrogen bonding contributions to δ (4). The benefit of such a definition is that the predictive abilities of the resulting solubility parameter improve since specific intermolecular interactions are taken into account. In general, δ_d, δ_p and δ_h cannot be determined directly (although in certain cases, IGC may be applicable); yet, the partitioning of the cohesive energy of a system into specific contributions has introduced the practice of combining δ with other properties (eg. dipole moments and hydrogen bonding capabilities) to represent the cohesive energy of a system and to predict solubility and compatibility more accurately.

Since direct measures of δ for polymer systems is difficult, additivity methods based on chemical structures are often used to determine δ_2. It was Small who first showed that the contribution of each atomic group to the cohesive energy could be summed to obtain the total cohesive energy of the molecule. More specifically, the solubility parameter is given as

$$\delta^2 = \frac{\sum_i E_{coh}}{\sum_i V} \qquad [2\text{-}4]$$

where the summation is over all "i" structural groups comprising the molecule (4). E_{coh} and V are the cohesive energy density and molar volume contribution of the ith group respectively. For the application of Equation 2-4 to polymers, only the repeat unit chemical structure is used. Several authors have compiled group contribution values (Van Krevelen, Hoy, Kaelble and Fedors). While the compilation of Fedors is the most extensive, it gives less accurate predictions of E_{coh}.

2.1.1.2 Applications of the Solubility Parameter

The use of the solubility parameter concept is widespread. While its most immediate use is to predict polymer-solvent solubility where solubility is predicted when the two systems have δ's within 1.8 H, its use has covered several other areas of science. Table 2.1 lists the many applications of the solubility parameter as reviewed by Hansen (5). Seymour has also reviewed the practical applications of the solubility parameter, from its use for solvent selection in heterogeneous solution polymerization of vinyl monomers to block copolymer synthesis via a free radical process (1). The practical uses of the Hildebrand solubility parameter will continue to be explored especially as novel techniques such as Inverse Gas Chromatography are introduced . Hansen stated that the use of the Hilldebrand solubility parameter is important at many "active" levels, and that the "...the highest is still to be found" (5).

Table 2.1. Applications of the Solubility Parameter.

Activity coefficients
Aerosol formulation
Chromatography
Coal solvent extraction
Compressed gases
Cosmetics
Cryogenic solvents
Dispersion
Dyes
Emulsions
Gas-Liquid solubility
Grease removal
Membrane permeability
Paint film appearance
Pharmaceutical
Pigments
Plasticizers, polymers, resins
Plasticization
Polymer and plasticizer compatibility
Printing ink
Reaction rate of radical polymerization
Resistance of plastics to solvents
Rubber blends
Solid surface characterization
Solvent extraction
Solvent formulation
Surface tension
Urea-water solutions

2.1.2 Inverse Gas Chromatography

2.1.2.1 Theory

Inverse gas chromatography is now a widely used technique for the study of thermodynamic parameters pertinent to polymer systems. The advantage of the techique is that such quantities as heats of solution and heats of adsorption of polymer solvent sytems are readily attainable in a thermodynamic state where the polymer concentration approaches unity. In this region of "infinite dilution" (with respect to the interacting probe) the experimentally determined retention times of the interacting probes can be related to the theory of gas-liquid partition chromatography, which yields the infinite dilution activity coefficient of the probe, γ_1^∞ (6,7). In the study of interaction parameters or solubility parameters, subsequent application of polymer-solution thermodynamics in terms of γ_1^∞ then yields the desired properties.

Inverse Gas Chromatography, IGC, as the name implies involves a chromatographic study of the stationary phase, usually the polymer of interest. Figure 2.1 shows the schematic of such an experiment (7). The set-up is the same as that for normal Gas-Liquid Chromatography (GLC) except that the flow rates are usually lower, and the probe concentrations injected are much less (in IGC terminology, the analyte injected is commonly referred to as the probe). In addition, in IGC the column can either be a packed column wherein the polymer is coated onto an inert support or a capillary column wherein the polymer is coated onto the inner walls of the column.

The information obtainable by IGC is best understood by considering a typical retention diagram for a semicrystalline material. Figure 2.2 is such a diagram, with Log (V_g) plotted as a function of 1/ (temperature) , where the specific retention volume is:

$$V_g = \frac{273}{T}\frac{V_r}{w_2} \qquad [2\text{-}5]$$

and V_r is the retention volume corrected for the pressure drop throughout the column and w_2 is the weight of polymer. A few words can be said about Equation 2-5. It is evident that the equation

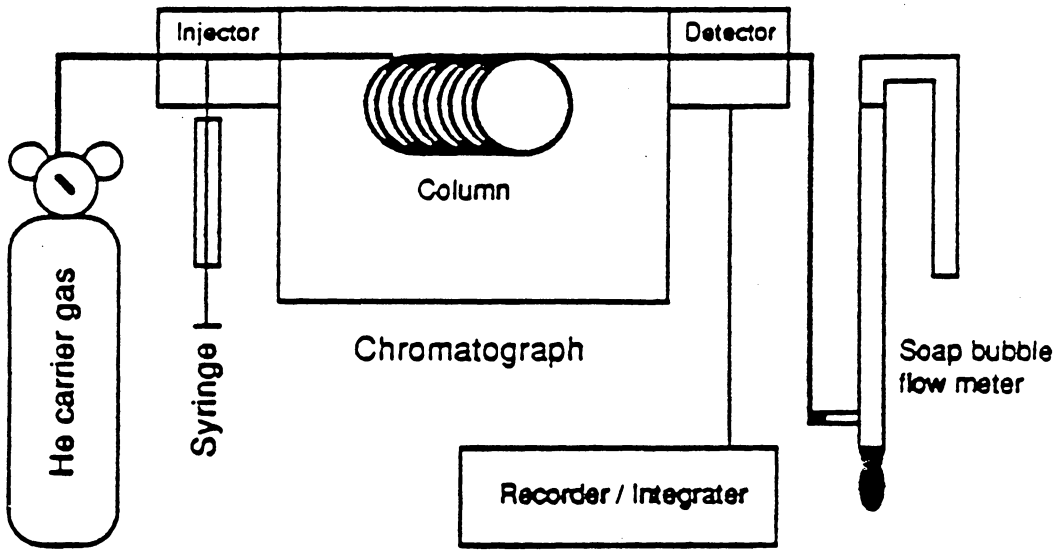

Figure 2.1. Schematic of an IGC experimental set-up.

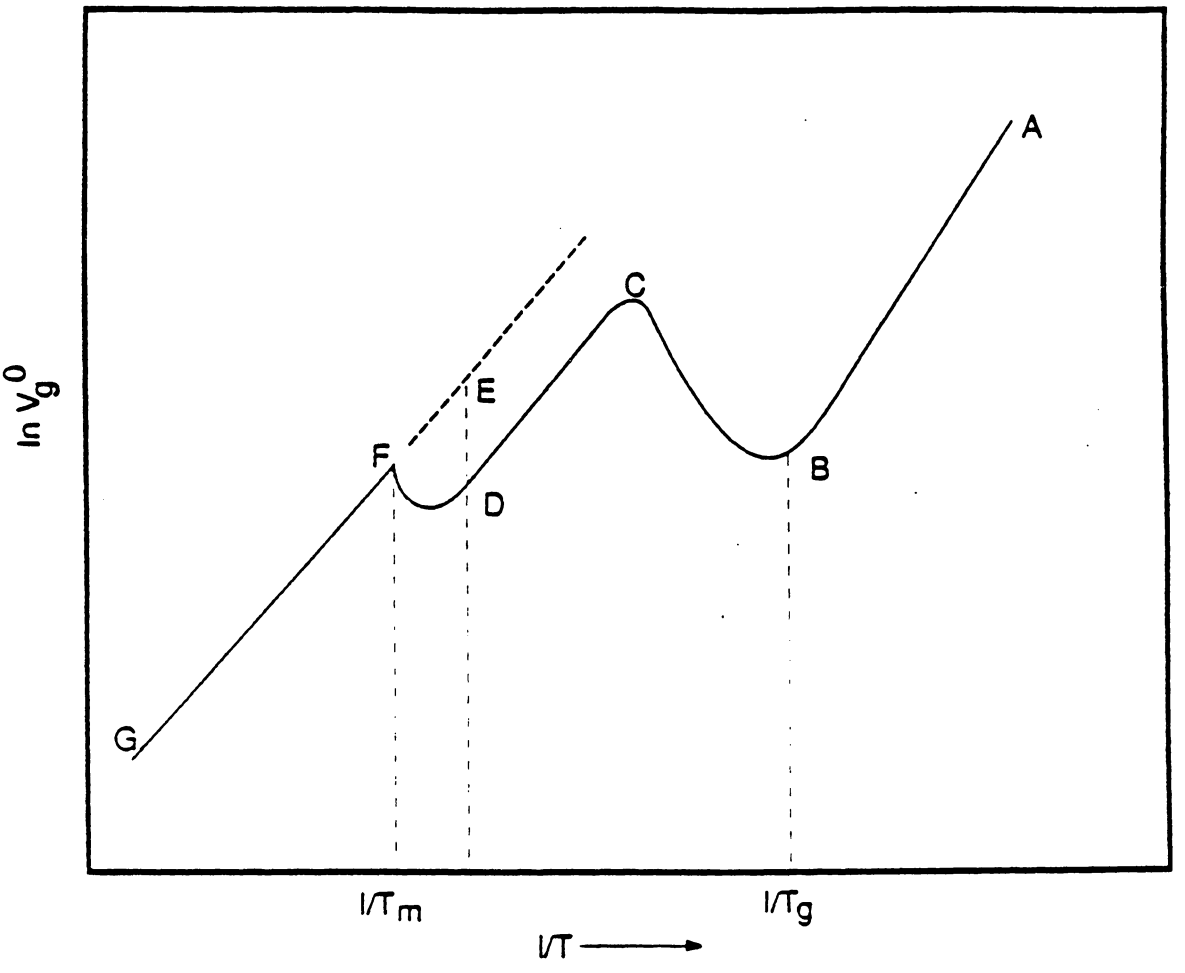

Figure 2.2. Retention diagram for a semicrystalline material.

carries with it a dual normalization. The temperature has been normalized to 0 ^{o}C and the retention volume normalized by the weight of

polymer (w_2) in the column. The normalization of V_r with w_2 results in an intensive property of the system, V_g, which contains information regarding any physiochemical interactions that the probe has with the polymer.

With this in mind one can begin to understand the shape of the retention diagram. Referring to Figure 2.2, in region AB the polymer is below its glass transition temperature. In this region the chief mechanism of retention of the probe is *adsorption* — since the probe moleules are precluded from the polymer bulk phase. The slope of the AB line is related to the heat of adsorption (ΔH_a) and latent heat of vaporization (ΔH_v) by

$$\text{slope} = (\Delta H_v - \Delta H_a) / 2.3\, R \qquad [2\text{-}6]$$

This equation is reminiscent of the Clausius-Clapeyron equation where a ln (P_{equil}) vs. 1/T plot yields a slope proportional to the heat of vaporization for a gas-liquid boundary. Since in IGC theory Vg is a measure of the activity of the probe, it is understandable why heats of adsorption are attainable as decribed above. Furthermore, as non-equilibrium conditions dominate non-linear behavior in the retention diagram is expected. This is true for the behavior of the probe in the CB region where there is non equilibrium *absorption* of the probe molecule due to the temperature dispersion of the second order transition (Tg) of the polymer.

The CD region is the truly amorphous region which "under the usual GLC conditions" corresponds to temperatures 40-50 ^{o}C above the glass transition temperature of the polymer. In this region the chief mechanism of retention is *absorption* and the slope of the CD line yields the heat of solution ΔH_s which in principle is:

$$\text{slope} = - \Delta H_s / R = (\Delta H_m - \Delta H_v) \qquad [2\text{-}7]$$

In this region the probe molecules are able to penetrate into the polymer bulk phase and equilibrium is established between the probe in the vapor phase and the probe in the amorphous liquid phase.

For the purpose of determining δ_2 and χ_{12} values for nitrocellulose, experimentation was done in this region.

The last transition region corresponds to the melting of the crystalline domains in the polymeric system. In this region it is possible to attain information regarding the size and distribution of the crystalline phase of the polymer.

2.1.2.2 IGC and Flory-Huggins Thermodynamics

2.1.2.2.1 The Flory - Huggins Chi Parameter from IGC

The theory of gas-liquid partition chromatography can be applied to IGC data when the chief mechanism of retention is *absorption.* From the theory, the infinite-dilution activity coefficient for the probe can be expressed as

$$\ln\left(\frac{a_1^{\infty}}{w_1}\right) = \ln \Omega_1^{\infty} = \ln\left(\frac{273\,R}{V_g M_1 P_1^{o}}\right) - \frac{P_1^{o}}{RT}(B_{11} - V_1) \qquad [2\text{-}8]$$

where the activity coefficient has been given on a weight basis in order to avoid a high molecular weight induced singularity in the equation (6). In addition, the latter term on the right hand side of the equation is a correction for non-ideality of the solute probe, expressed through the second virial coefficient, B_{11}. P_1 is the equilibrium vapor pressure of the probe at the column temperature,T, M_1 is the molecular weight of the probe, V_1 is the liquid molar volume of the probe at the column temperature and R is the gas constant. The origin and a derivation of the above equation is given in section 2.5.1 of the appendix.

It is more useful to redefine probe-polymer interactions obtained in an IGC experiment (embodied in γ_1^{∞}) in terms of the classical variables used in polymer solution thermodynamics: χ_{12} and δ_2. The Flory-Huggins lattice theory yields an expression for the activity of the solute as

$$\ln a_1 = \left[\ln \phi_1 + \left(1 - 1/\iota\right)\phi_2\right] + \chi_{12}\phi_2^2 \qquad [2\text{-}9]$$

where i the is the number average degree of polymerization (6). When the above equation is applied to an infinitely dilute system with respect to the probe (as $\phi_2 \rightarrow 1$) the activity coefficient on a weight fraction basis becomes

$$\ln\left(\frac{a_1^{\infty}}{w_1}\right) = \ln \Omega_1^{\infty} = \ln\left(\frac{v_1}{v_2}\right) + \left(1 - \frac{V_1}{\langle M_2 \rangle v_2}\right) - \frac{P_1^{o}}{RT}(B_{11} - V_1) \qquad [2\text{-}10]$$

where v_1 and v_2 are the specific volumes of the solute and polymer respectively. Equation 2-10 when combined with Equation 2-8 yields a relation between Flory -- Huggins chi parameter and the experimental IGC datum Vg.

$$\chi_{12}^{\infty} = \ln\left(\frac{273.2\ R\ v_2}{V_g\ V_1\ P_1^{o}}\right) - \left(1 - \frac{V_1}{\langle M_2 \rangle v_2}\right) - \frac{P_1^{o}}{RT}(B_{11} - V_1) \qquad [2\text{-}11]$$

A dicussion and derivation of the Flory Huggins lattice theory is given in section 1.5.2 of the appendix.

A few notes concerning the origin of χ_{12} and its phenomenological significance should be made in order to understand the meaning of such a quantity. The Flory Huggins χ_{12} parameter results from a consideration of the non-ideal behavior of polymer solutions, and arises from arguments concerning the non-combinatorial (or excess) free energy of mixing. More specifically χ_{12} is a measure of the pairwise energy of interaction between a polymer segment and solvent molecule in a lattice field, e_{ij}, which can result from an array of possible intermolecular forces (i.e. London-dispersion forces, dipole-dipole interactions, Lewis acid-base interactions...). χ_{12} is related to the "excess" chemical potential of the solute on a per unit mole basis by the following:

$$\Delta\mu^{ex} = \left(\chi_{12} - \frac{1}{2}\right) RT\Phi_2^2 \qquad [2\text{-}12]$$

(where "excess" refers to any contribution to ΔG_m arising from a non-combinatorial argument) (9). From Equation 2-12 one sees that when χ_{12} is 0.5 the solution behaves ideally and the mixing of the probe with the polymer phase results only from entropic considerations. When χ_{12} is less than

0.5, mixing is promoted due to favorable interactions between probe and polymer and the "excess" chemical potential is lowered. In theory the more negative χ_{12} is the stronger the interactions are between probe and polymer. In addition, χ_{12} is comprised of both an enthalpic and entropic term (χ_S and χ_H respectively) which will be a necessary consideration when the Hildebrand -Scatchard theory is combined with the Flory-Huggins treatment in order to determine solubility parameters from IGC data.

2.1.2.2.2 The Hildebrand Solubility Parameter

In order to obtain the solubility parameter for the polymer of interest, the Flory-Huggins theory is combined with the Hildebrand - Schatchard theory. This allows one to relate the calculated χ_{12} values (from the experimental IGC data) to the solubility parameter of the probe and polymer. From the theory the following can be written:

$$\frac{\delta_1^2}{RT} - \frac{\chi_{12}}{V_1} = \frac{2\delta_2^{\infty}}{RT}\delta_1 - \left(\frac{\delta_2^{\infty 2}}{RT} + \frac{\chi_s}{V_1}\right) \qquad [2\text{-}13]$$

where for an infinite dilution IGC experiment δ_2 is replaced by δ_2^{∞} (7). Hence a plot of (δ_1^2 /RT - χ_{12} /V_1) against δ_1 should yield a straight line with a slope of $2\delta_2^{\infty}$ /RT (throughout the text δ_2 will be used with the understanding that in an IGC experiment infinitely dilute conditions are understood). Therefore, δ_2 can be determined from pure component properties and experimental data (χ_{12}) alone. Figure 2.3 shows a typical plot based on Equation 2-13 obtained from the literature for a typical IGC experiment.

2.2 Experimental

2.2.1 Materials

2.2.1.1 Probes

Probes were obtained from Aldrich and were used without further purification. The probes were chosen such that a large span in solubility parameters was attained. This insured a proper linear fit of the experimental data to Equation 2-13. In addition, many probes were evaluated in

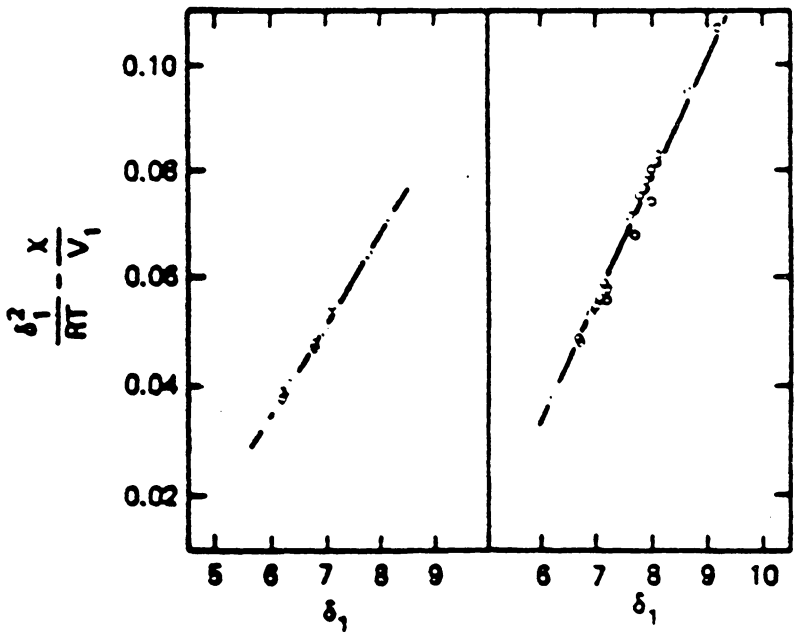

Figure 2.3. Estimation of the solubility parameter from χ_{12} : (a) polystyrene at 193 °C ; (b) poly(methyl acrylate) at 100 °C [δ_2 in (cal cm^{-3})$^{1/2}$].

terms of their retention behavior, and those that eluted at reasonable times with respect to the inert probe were considered as candidates.

2.2.1.2 Columns

In a typical IGC experiment the polymer is deposited onto an inert stationary phase at 5-10 wt/wt % loading then packed into a stainless steel column for analysis. Columns were prepared by dissolving the dry ntrocellulose with 0.5 wt./wt.% stabilizer (Arkadit II) in THF. The solution and inert support were added to a 500 ml flask with internal vigreux fingers and the solvent was removed by a rotary evaporator. The coated support was then vacuum dried at 65 ^{o}C overnight and subsequently sieved through 60/80 mesh and packed into a 4 ft.-0.25- inch outer diameter stainless steel column using a mechanical vibrator. The column was plugged with silane treated glass wool and coiled for insertion in the chromatograph. The column was purged with helium (the carrier gas) for 30 minutes and conditioned overnight above the Tg of the stationary phase, with only the inlet part of the column connected. The conditioning of the column ensured a low detector background signal prior to analysis. The weight of polymer on the inert support and percent loading were determined by ashing using a Perkin Elmer - TGA. All columns were used immediately after preparation and subsequently kept in an inert Helium atmospere at room temperature when not in use. Most experiments were done within a two week period and background noise was not a problem; therefore, decomposition was thought to be minimal.

2.2.2 Instrumentation

A Hewlett-Packard 5890 gas chromatograph with a flame ionization detector was used. Helium was used as the carrier gas and flow rates were determined by use of a soap bubble flow meter connected at the end of the column. Typical flow rates were 9 ml/min.. Samples were injected with a Hamilton 10 µl gas tight syringe. In most cases 1 µl of probe vapor was injected along with CH_4 (g) to act as a marker for the dead volume in the column and retention times were determined from their peak maximum with the use of an HP 3392A integrator. Only retention times

that were independent of sample size were used for the experimental calculations. This ensured that measurements were indeed in the infinitely dilute region.

Inlet and outlet pressures for the column were read with a mercury manometer (± 0.05 mm Hg.) whose values were used for the calculation of the J_3^2 correction factor for pressure drop in the column.

2.2.3 Data reduction

The specific retention volumes, Vg, were calcualted by:

$$V_g = \frac{(t_p - t_m)}{w_2} F J_3^2 \qquad [2\text{-}14]$$

where t_p is the infinite-dilution retention time for the interacting probe, t_m is the retention time for the CH_4 (g) marker probe, F is the flow rate measured by a soap bubble flow meter corrected for the vapor pressure of water and corrected to 273.16 K. The expression for F is:

$$F = \frac{273.2\,(P_o - P_{H_2O})}{T} \qquad [2\text{-}15]$$

where T is the column temperature (K), P_o is the outlet pressure and $P_{(H2O)}$ is the vapor pressure of water at the temperature of the soap bubble flow meter. The correction for the pressure drop in the column, due to the gas compressibilty is given as:

$$J_3^2 = \frac{3}{2}\left(\frac{(\frac{P_i}{P_o})^2 - 1}{(\frac{P_i}{P_o})^3 - 1}\right) \qquad [2\text{-}16]$$

where Po and Pi are the outlet and inlet pressure repectively (10).

Liqiuid molar volumes and solute vapor pressures at the experimental temperature were obtained from the compilations of Smith and Srivastava for all probes except nitromethane and ethyl acetate (11). Vapor pressure and molar volume data for nitromethane and ethyl acetate were

obtained from estimation methods available in The Handbook of Chemical Property Estimation Methods (12). Sections 2.5.4.1 and 2.5.4.2 of the appendix discuss these estimation methods.

Second Virial coefficients were obtained for the probes at the column temperature from published B_{11} versus temperature data compiled by Dymond and Smith (13).

Solubility parameters of the probes at 100 ^{o}C were calculated from ΔH_v values at 100 ^{o}C obtained from Smith and Srivistava. For ethyl acetate and nitromethane ΔH_v values at 100 ^{o}C were estimated using methods available in The Handbook of Chemical Property Estimation Methods. This method is discussed in the appendix.

All probe and Column parameters are given in Tables 2.2-2.4.

2.3 Results and Discussion

2.3.1 Experimentally Determined χ_{12} Values for Nitrocellulose

The χ_{12} parameters obtained from Equation 2-11 are listed in Table 2.5. The lowest χ_{12} values for all three polymer samples are with acetone and ethyl acetate, known to be good solvents for nitrocellulose. In addition, the interaction of the t-butyl alcohol probe seems to increase with decreasing nitration level. This agrees with literature observations that for nitrocellulose of lower nitrogen content (%N) organic alcohols are better solvents. It is important that one realize that the χ_{12} values given in Table 2.5 are for measurements made in the infinite-dilution realm which may differ from values determined from dilute polymer solutions. In dilute polymer solutions intramolecular polymer interactions are minimized in good solvents, whereas in the infinite-dilution realm of IGC the polymer mole fraction concentration approaches unity, and intramolecular polymer interactions are more probable; minimizing the extent of intermolecular contact and interaction between probe and polymer.

2.3.2 Experimentally Determined δ_2 Values for Nitrocellulose

From the experimentally determined χ_{12} values for the NC-probe systems the solubility

Table 2.2. Probe and column parameters for 11.5 %N column loaded with .290 g of polymer.

Probe	$\delta_1^{25°C}\left(\frac{cal}{cm^3}\right)$	$\delta_1^{100°C}\left(\frac{cal}{cm^3}\right)$	$t_{reten}(min.)$	$P_1^\circ(mmHg)$	$V_1^\circ\left(\frac{cm^3}{mol}\right)$	$B_{11}^\circ\left(\frac{cm^3}{mol}\right)$	$Flow\left(\frac{ml}{min.}\right)$
Acetone	9.9	8.09	10.74	2782	83.91	- 885	8.92
Hexane	7.3	6.14	.10	1843	148.10	- 1031	8.79
Octane	7.6	6.67	.29	354	179.90	- 2122	8.89
t-butanol	10.6	8.61	1.17	1448	106.38	- 981	8.89

Table 2.3. Probe and column parameters for 12.5%N column loaded with .378 g of polymer.

Probe	$\delta_1^{25°C}\left(\frac{cal}{cm^3}\right)$	$\delta_1^{100°C}\left(\frac{cal}{cm^3}\right)$	t_{reten}(min.)	P_1°(mmHg)	$V_1^\circ\left(\frac{cm^3}{mol}\right)$	$B_{11}^\circ\left(\frac{cm^3}{mol}\right)$	Flow $\left(\frac{ml}{min.}\right)$
Acetone	9.9	8.09	8.96	2782	83.91	- 885	8.80
Hexane	7.3	6.14	.11	1843	148.10	- 1031	8.72
Octane	7.6	6.67	.26	354	179.90	- 2122	8.91
t-butanol	10.6	8.61	.60	1448	106.38	- 981	8.87
EtAc	9.1	8.24	6.80	1520	92.97	- 1057	8.86
Nitro - methane	12.7	12.1	12.49	760	48.95	- 1525	8.79

Table 2.4. Probe and column parameters for 13.5%N column loaded with .409 g of polymer.

Probe	$\delta_1^{25°C}\left(\frac{cal}{cm^3}\right)$	$\delta_1^{100°C}\left(\frac{cal}{cm^3}\right)$	t_{reten}(min.)	P_1°(mmHg)	$V_1^\circ\left(\frac{cm^3}{mol}\right)$	$B_{11}^\circ\left(\frac{cm^3}{mol}\right)$	Flow $\left(\frac{ml}{min.}\right)$
Acetone	9.9	8.09	4.20	2782	83.91	- 885	8.76
Hexane	7.3	6.14	.25	1843	148.10	- 1031	8.77
Octane	7.6	6.67	.81	354	179.90	- 2122	8.72
t-butanol	10.6	8.61	.45	1448	106.38	- 981	9.56
EtAc	9.1	8.24	3.55	1520	92.97	- 1057	8.72
Nitro - methane	12.7	12.1	8.82	760	48.95	- 1525	8.89

Table 2.5. Experimentally determined chi parameters for 11.5, 12.5, and 13.5%N nitrocellulose/probe systems.

	11.5% NC	12.5% NC	13.5% NC
Hexane	2.15	2.36	1.63
Octane	2.50	2.90	1.85
Acetone	-2.33	-1.86	-1.02
Ethyl Acetate	-	-1.31	-.38
T-butanol	.26	1.20	1.49
Nitromethane	-	-.42	-.01

parameter of nitrocellulose at various nitration levels were calculated using Equation 2-13. Figures 2.4 to 2.6 show the ($\delta_1^2/RT - \chi_{12}/V_1$) versus δ_1 plots for the various nitrocellulose systems. From the plots, curves were obtained which are linear (as expected from theory). The solubility parameters were calculated from the slopes of the curves. For the 11.5%N column plot the datum from the t-butanol probe was excluded from the least squares calculation , while for the 12.5 and 13.5 %N columns the t-butanol probe data have been included in the calculations. The anomaly in the behavior of the t-butyl probe with the 11.5 %N column can be understood by considering the solubility parameter in more detail.

As discussed in the introduction the solubility parameter can be expressed as a sum of specific contributions

$$\delta^2 = \delta_d^2 + \delta_p^2 + \delta_h^2 \qquad [2\text{-}17]$$

Accordingly, the solubility parameter values obtained by IGC using nonpolar probes would be expected to differ from that obtained using polar probes or probes where hydrogen bonding is possible, due to the additional interactions. Guillet et al. examined the effect of using polar and nonpolar probes in IGC experiments to determine δ_2 (4). They found that for the polymers studied there was no dependence of δ_2 on the polarity of the probes used. They argued that in order to see δ_h and δ_p contributions to δ_2 very strong hydrogen bonding or polar interactions would have to be present between probe and polymer. With nitrocellulose and t-butanol strong hydrogen bonding interactions could occur between the hydroxyl groups of the alcohol probe and the nitro and hydroxyl group on the cellulose ring. Figure 2.7 is a comparison of the the chromatograms for t-butanol on all three columns. It is interesting that the chromatogram of t-butanol on the 11.5%N column shows significant tailing compared to that on the other columns indicating that strong intermolecular interactions are present resulting in non-equilibrium *absorption* . While tailing behavior is indicative of specific interactions it also precludes the use of such chromatograms

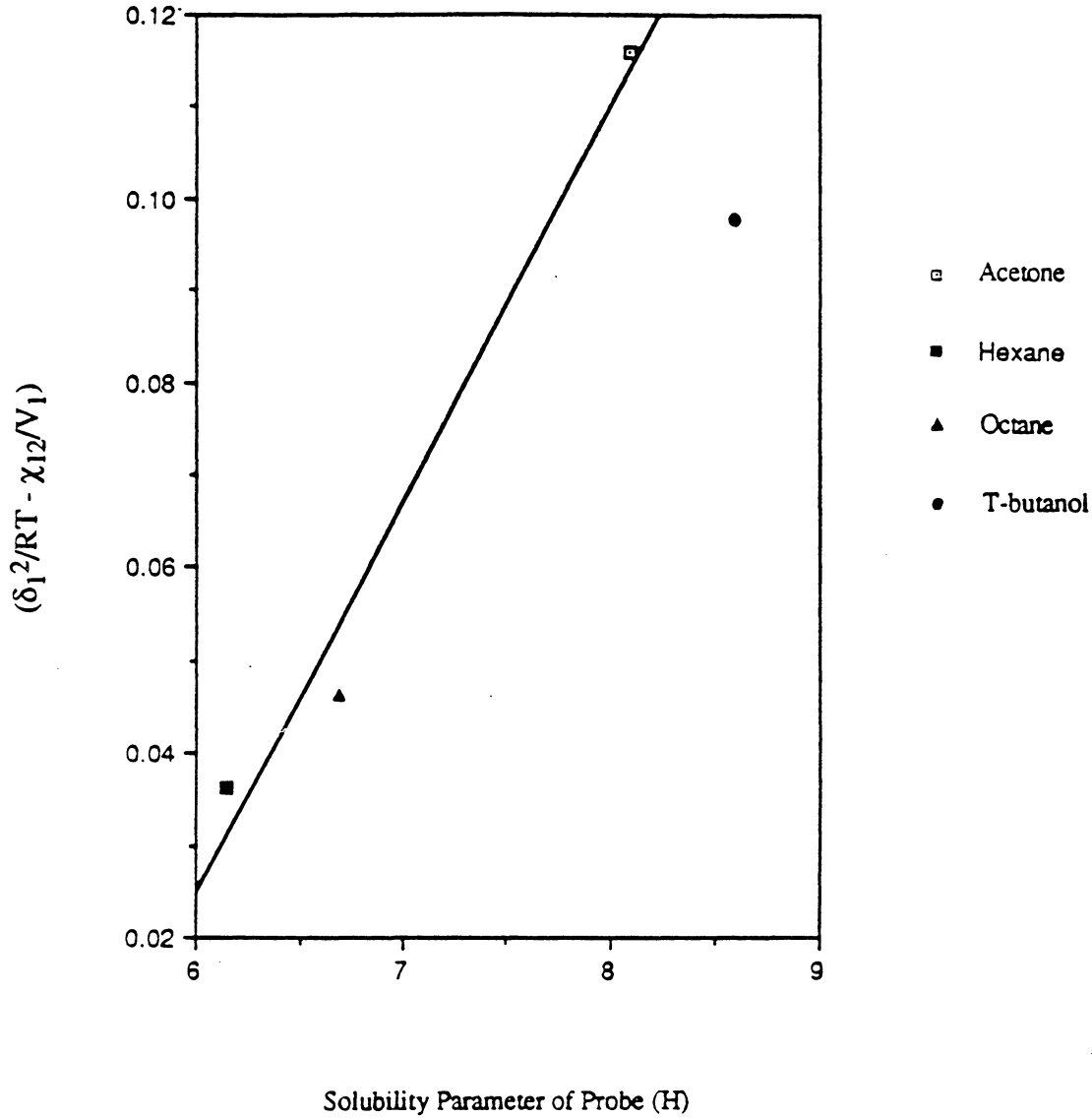

Figure 2.4. $(\delta_1^2/RT - \chi_{12}/V_1)$ versus d_1 plot for 11.5% N column.

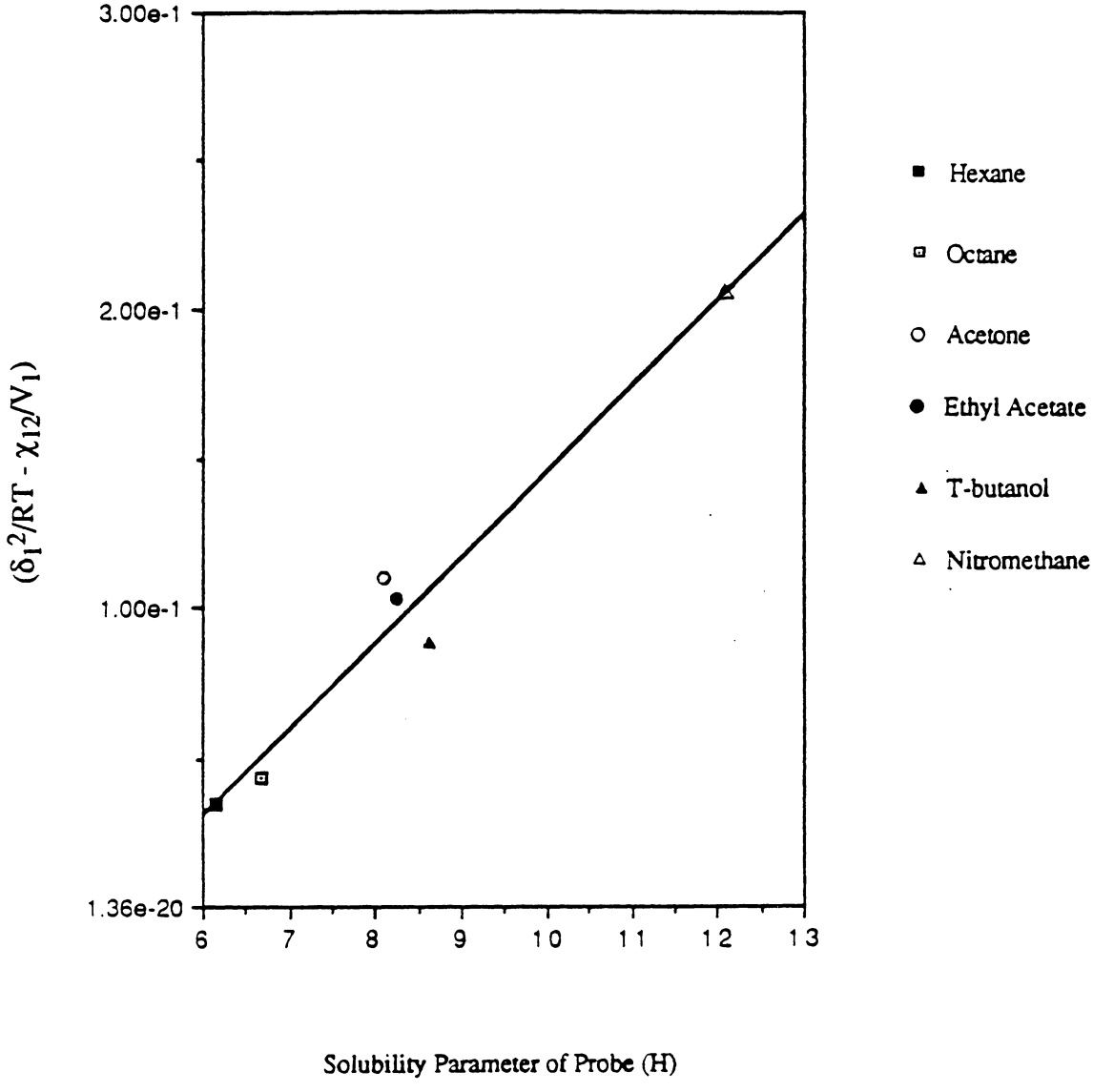

Figure 2.5. $(\delta_1^2/RT - \chi_{12}/V_1)$ versus δ_1 for 12.5%N column.

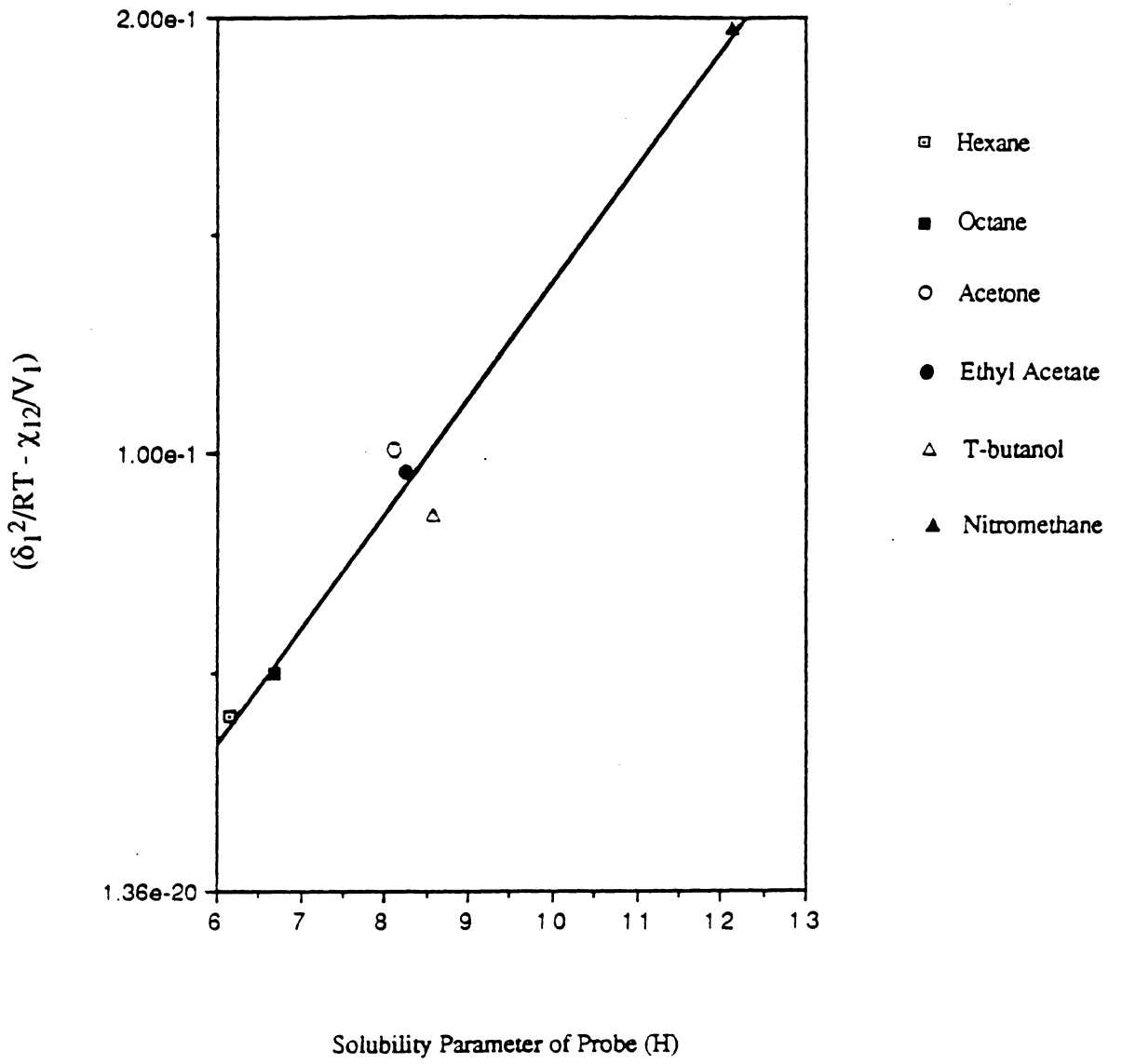

Figure 2.6. $(\delta_1^2/RT - \chi_{12}/V_1)$ vesus δ_1 plot for 13.5%N column.

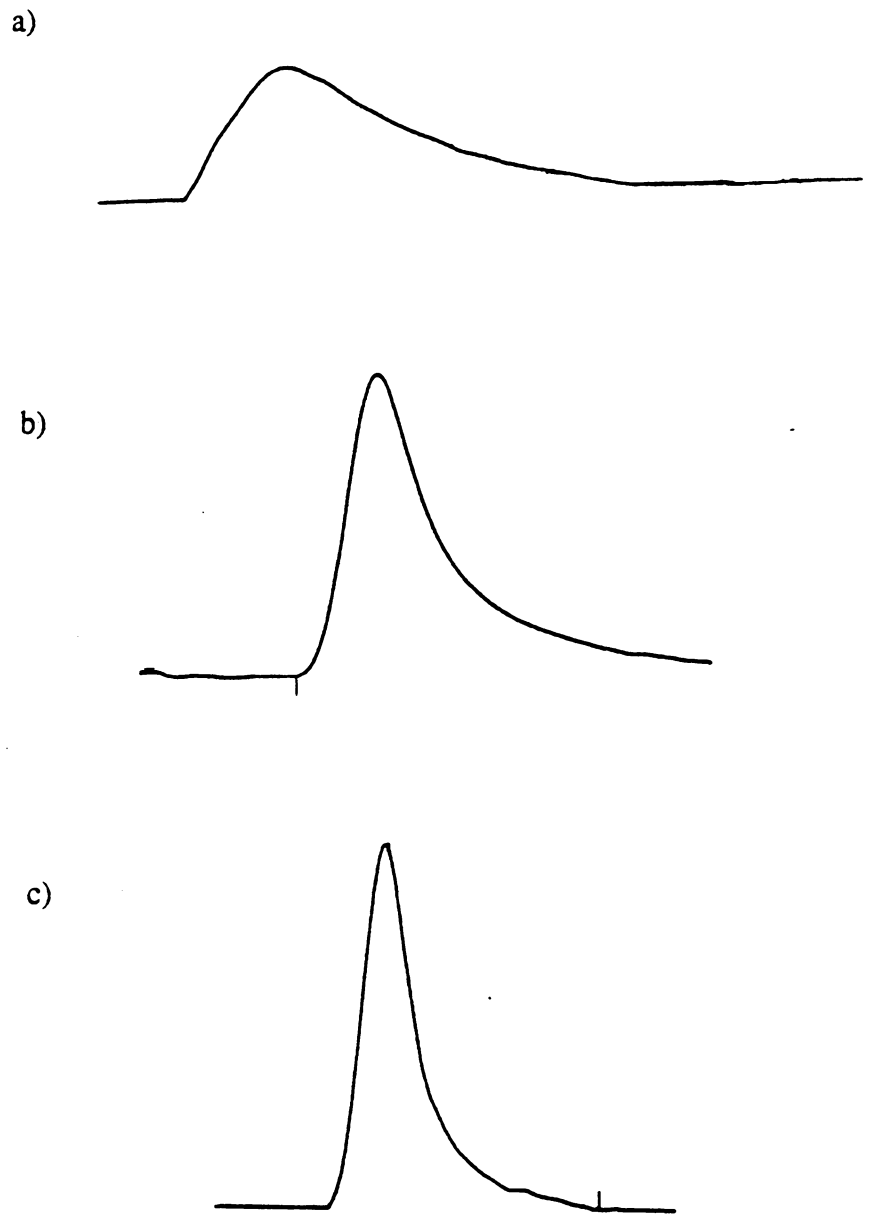

Figure 2.7. Experimental chromatograms for t-butanol on: a) 11.5%N column b) 12.5%N column c) 13.5%N column

for thermodynamic calculations since equilibrium conditions are not present.

The calculated solubility parameters from the slopes of Figures 2.4 to 2.6 are listed in Table 2.6 along with the errors from the standard deviation of the slope. While the values are at infinite dilution and at 100 ^{o}C, it is expected that the values are characteristic of δ_2 values at 25 ^{o}C and under finite concentration conditions as discussed below. Figure 2.8 is a reported "three dimensional" solubility plot for nitrocellulose; although the nitration level was not given, it is evident that the values determined by IGC are within the expected range (15).

2.3.3 Temperature Dependence of χ_{12} and δ_2

According to Giullet, in a typical IGC experiment true liquid-like behavior is attained at temperatures 40 to 50 ^{o}C above the glass transition of the polymer (6). The glass transition temperature of 13.5% N nitrocellulose was determined both by Dynamic Mechanical Analysis and Differential Scanning Calorimetry. Figure 2.9 shows the dynamic mechanical thermal spectrum of a solvent cast nitrocellulose film. In these experiments the temperature at which tan δ is a maximum is taken as the T_g of the material. The dynamic mechanical results (at 1Hz) agree with the DSC results of Figure 2.10, both show a glass transition temperature at approximately 55^{o}C. The IGC experiments for nitrocellulose were therefore done at 100 ^{o}C in order to insure amorphous behavior; it was assumed that decomposition would be minimal due to the incorporation of the antioxidant. Since, the experimentally determined χ_{12} values at 100 ^{o}C were used to determine the solubility parameters, the question concerning the temperature dependence of χ_{12} and the significance of δ_2 from these values arises.

For endothermic heats of mixing χ_{12} is usually taken to have an inverse temperature dependence of the form

$$\chi_{12} = \alpha + \beta/T \qquad [2\text{-}18]$$

Table 2.6. Experimentally determined solubility parameters for 11.5, 12.5, 13.5 %N nitrocellulose.

Nitrocellulose Sample	Solubility Parameter $(cal/cm^3)^{1/2}$
11.55 %N	15.9 ± 2.5
12.58 %N	10.8 ± 1.1
13.49 %N	9.6 ± 0.8

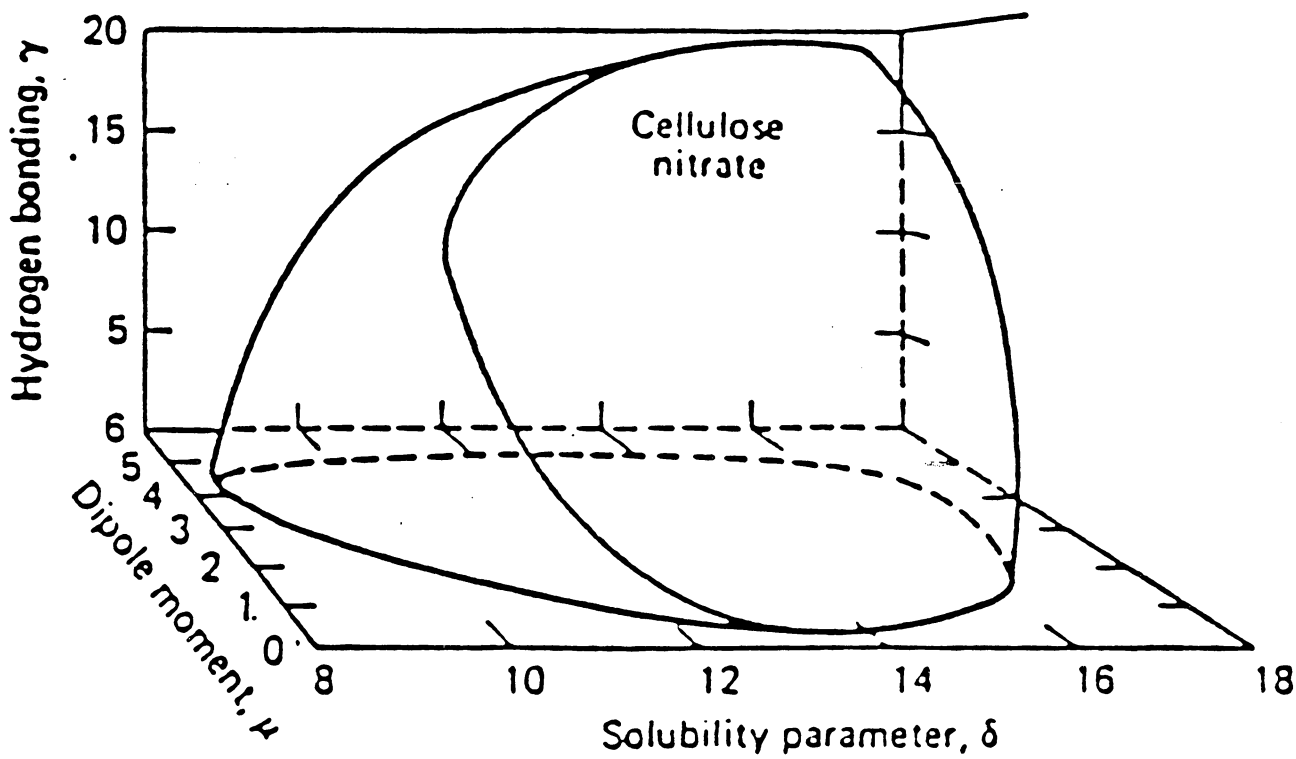

Figure 2.8. Three dimensional solubility plot for nitrocellulose (with γ being a spectroscopic parameter in wavenumber units) (15).

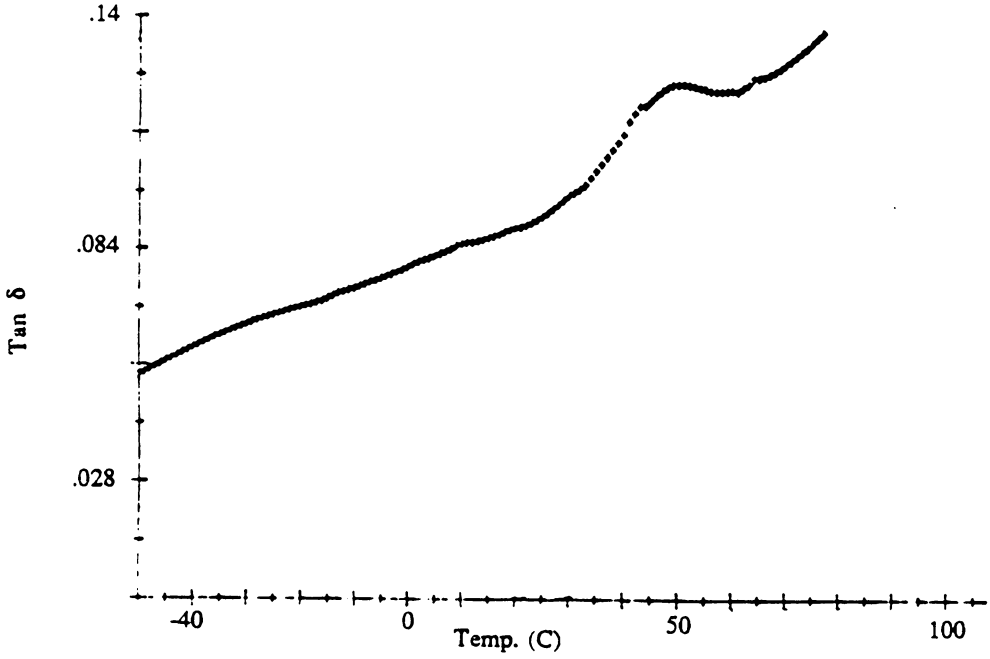

Figure 2.9. D.M.T.A. scan of solvent cast nitrocellulose film (13.5% wt. N).

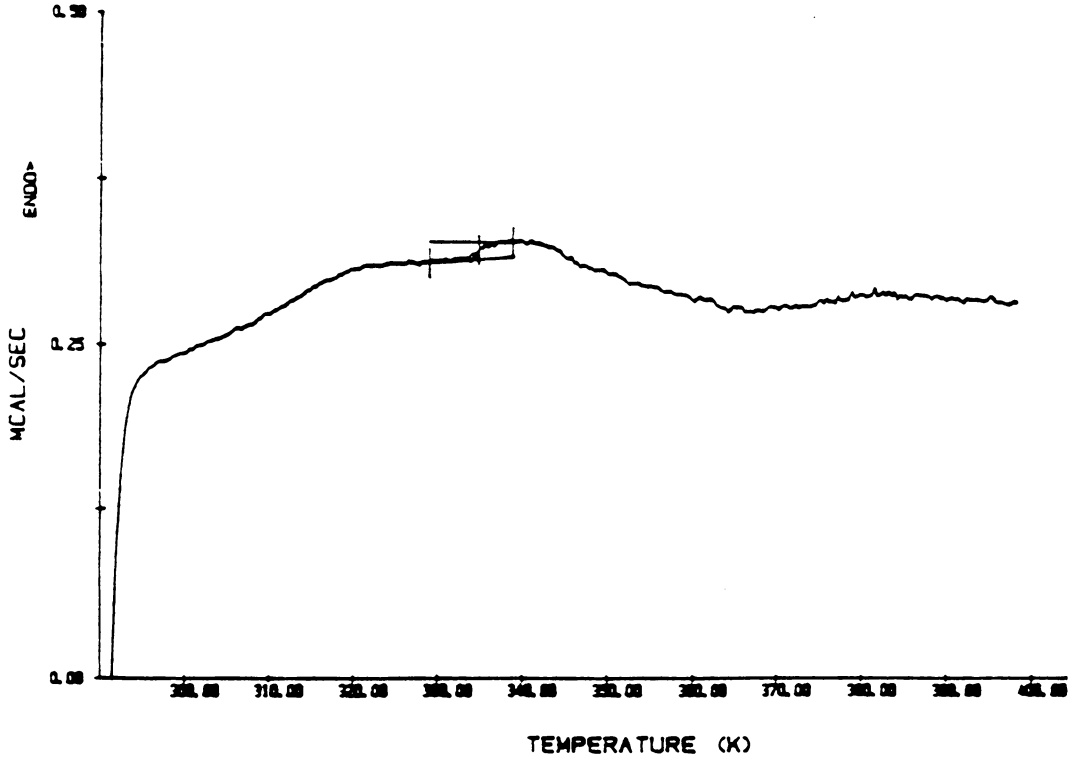

Figure 2.10. D.S.C. scan of dried nitrocellulose powder (13.5% wt. N).

here α is the temperature independent part of χ (χ_S) and β is the temperature dependent part of χ (χ_H). Hence, at lower temperatures higher χ_{12} values are expected. Giullet et al. have measured χ_{12} values via IGC for polychloroprene, polybutadiene-acrylonitrile, poly(ethylene-vinyl acetate), and polybutadiene at a series of temperatures and found that the χ_{12} values were temperature dependent and decreased with increasing temperature (14). By evaluating χ_{12} for several probe-polymer systems at several temperatures they were able to extrapolate to lower unaccessible temperatures and obtain χ_{12} values at 25 ^{o}C. Using χ_{12} values evaluated at 75 ^{o}C, and extrapolated values at 25 ^{o}C the solubility parameters for the above systems were determined at the two corresponding temperatures. For all the polymers studied the difference in the solubility parameters at 75 ^{o}C and 25 ^{o}C were negligible within the experimental error. Therefore, it seems that although the χ_{12} values may be temperature dependent the solubility parameters calculated are not strongly temperature dependent. In addition, Giullet's calculated values of δ_2 at 75 ^{o}C agreed in all cases with those reported in the literature for the same systems at 25 ^{o}C.

2.3.4 Method of Group Contributions for δ_2

As discussed in the introduction the solubility parameter can be calculated from knowledge of the molecular structure. Nitrocellulose has the structure shown in Figure 2.11,where x is either a hydroxyl group (OH) or a nitro group (ONO_2). The following equation gives the %N as a function of the number average degree of substitution, <x>

$$\% N = \frac{14.01 \langle x \rangle}{45 \langle x \rangle + 162.16} \qquad [2\text{-}19]$$

Hence, the substitution of one, two, or three OH groups would yield nitrocellulose of 6.76, 11.11, and 14.14 %N respectively. In the calculation of the solubility parameter as a function of %N the above equation was used to determine the number average of OH and ONO_2 groups per repeat unit. The solubility parameters of nitrocellulose were calculated from the group contribution

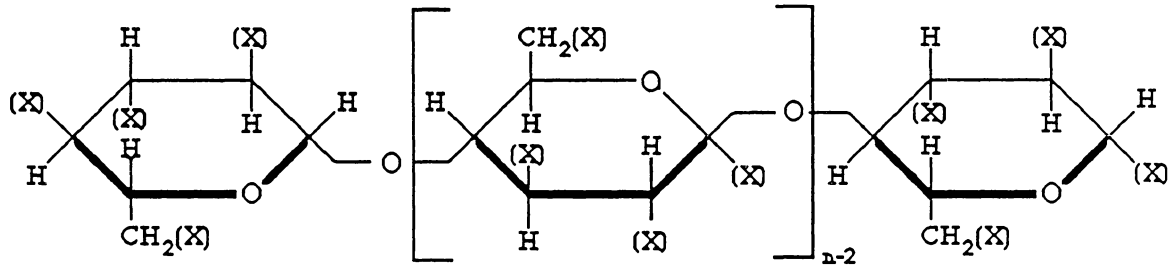

Figure 2.11. Chemical structure of nitrocellulose.

data compiled by Fedors whose values are reproduced in the appendix (4). While several authors have compiled group contribution data, the quality of any calculation determined by additivity methods will be dependent on the authors whose values are used. In addition, one must use a self consistent set of group contribution values for the calculations to be valid.

The calculated solubility parameters at three different levels of nitration are given in Table 2.7, and although the standard errors are not given the uncertainty expected in the values is 10%. Figure 2.12 compares the experimental values of δ_2 with those predicted by the group contribution method. The values are in close agreement, yet, there is a difference in the sensitivity of δ_2 with respect to %N. Reasons for the differences are not clear but it may indeed be that some degradation did occur especially with the higher nitrated material.

2.4 Summary

The solubility parameters of nitrocelluloses at three different nitration levels were determined by Inverse Gas Chromatography. The results revealed that as the nitration level is decreased the solubility parameter is increased within the range studied. Experimental results are in agreement with those calculated by additivity methods and values reported in the literature.

Table 2.7. Theoretical solubility parameters for nitrocellulose as determined by the method of Fedors.

Nitrocellulose Sample	Solubility Parameter $(cal/cm^3)^{1/2}$
6.76 %N	17.29
11.11 %N	14.73
14.14 %N	12.79

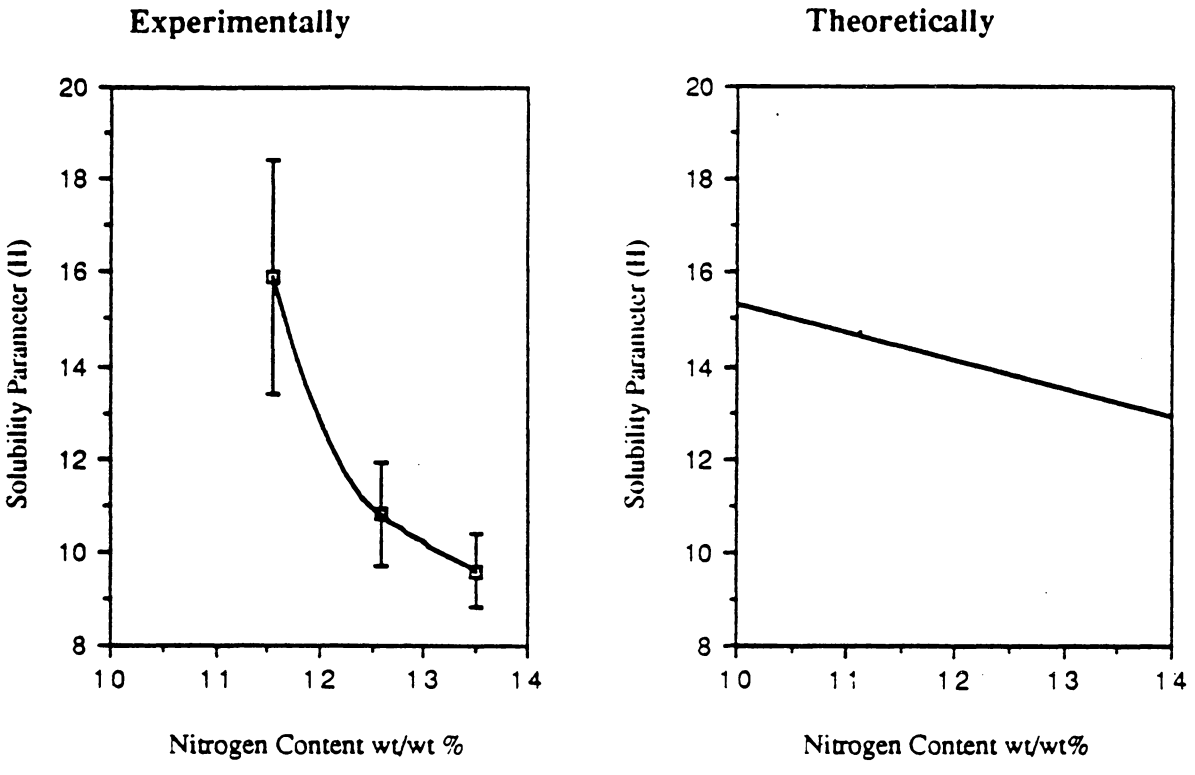

Figure 2.12. Hildebrand Solubility Parameter as a function of nitration level both calculated from theory and experimentally determined via Inverse gas Chromatography.

2.5 Appendix

2.5.1 Theory of Gas Liquid Partition Chromatography

Equation 2-8 expresses the activity coefficient of a vapor solute in an IGC experiment in terms of solute parameters and the IGC datum, Vg. Its derivation arises from dilute solution thermodynamics and "infinite- dilution" variables pertinent to gas chromatography.

From Raoult's law the activity of a component in an *ideal solution* can be expressed as

$$a_i = P_i/P_i^o = x_i \qquad [2\text{-}20]$$

where P_i^o is the vapor pressure of the pure component, P_i is the vapor pressure over the solution and x_i is its mole fraction solution. Correcting for non-ideality Equation 2-20 becomes

$$a_i = P_i/P_i^o = \gamma_i x_i \qquad [2\text{-}21]$$

where γ_i is the corresponding activity coefficient of the solute. Equation 2-21 is simply Henry's law for *ideal dilute solutions* . Equation 2-21 can be used as a starting point to develop an expression for γ_i in terms of basic gas chromatography variables.

Littlewood defined the specific retention volume, Vg, corrected to 0 ^oC as

$$Vg = (273.2/Tw)V'_N \qquad [2\text{-}22]$$

where V'_N is the net retention volume corrected for the pressure drop throughout the column, T is the column temperature, and w is the weight of polymer in the column (16). In addition, a basic relationship in gas chromatography defines the partition coefficient, β, which in the infinite dilution region is

$$\beta = q/c \qquad [2\text{-}23]$$

where q is the probe concentration in the stationary phase in (mol/g), and c is the probe concentration in the vapor phase in (mol/ml). Combining Equation 2-22 and 2-23 one obtains

$$V_g = (273.2/T)\beta \qquad [2\text{-}24]$$

An expression for the activity coefficient of the probe can easily be obtained with above equations.

When equilibrium *absorption* is the dominant mechanism of retention then Equation 2-21 can be used to define the activity coefficient of the solute-probe:

$$\gamma_i = P_i/P_i^0 x_i \qquad [2\text{-}25]$$

Under infinite-dilution conditions the number of moles of solute, n_1, are much less than the number of moles of stationary phase, n_2. Applying this limit and assuming ideal gas behavior of the vapor probe Equation 2-25 can be expanded as

$$\gamma_1 = \frac{P_1}{P_1^0 x_1} = \frac{cRT}{P_1^0 \frac{n_1}{W_2} M_2} = \frac{RT}{P_1^0 \beta M_2} \qquad [2\text{-}26]$$

where c and b are defined by Equation 2-23. Substituting Equation 2-24 for β leads to

$$\gamma_1^\infty = \frac{273\ R}{V_g M_2 P_1^\circ} \qquad [2\text{-}27]$$

Instead of P_i^0, the fugacity, f_i^0, of the pure solvent should be used according to the equation

$$\ln f_i^0 = \ln P_i^0 + (B_{11} - V_1) P_i^0/RT \qquad [2\text{-}28]$$

where V_1 and B_{11} are the molar volume and second virial coefficient of the probe respectively; Equation 2-28 becomes

$$\ln \gamma_1^\infty = \ln \frac{273\ R}{V_g M_2 P_1^\circ} - \frac{(B_{11} - V_1)}{RT} P_1^\circ \qquad [2\text{-}29]$$

This equation is valid for normal GLC where the stationary phase is a low molecular weight compound; but, in IGC M_2 is large resulting in unrealistic γ_1^∞ values. This problem can be circumvented by considering Equation 2-25 where the activity coefficient has been expressed on a mole fraction basis (γ_1). Under infinite dilution conditions the activity coefficient on a weight fraction basis (Ω_1) can be written as :

$$\Omega_1 = \frac{P_1}{P_1^{\circ} w_1} = \frac{P_1 M_2}{P_1^{\circ} \frac{n_1}{n_2} M_1} = \gamma_1 \left(\frac{M_2}{M_1}\right) \qquad [2\text{-}30]$$

where w_1 is the weight fraction of solute or probe in the solution and M_1 and M_2 are the corresponding molecular weights of the components. The final expression for the activity coefficient from gas chromatography variables becomes

$$\ln \Omega_1 = \ln \frac{273\,R}{V_g M_1 P_1^{\circ}} - \frac{(B_{11} - V_1)}{RT} P_1^{\circ} \qquad [2\text{-}31]$$

2.5.2 Thermodynamics of Polymer Solutions: The Flory-Huggins Theory

For solutions whose components are low molecular weight compounds the *ideal solution* is one in which Raoult's law is obeyed and where the entropy change for the mixing is given as

$$\Delta S_m^{ideal} = -R(x_1 \ln x_1 + x_2 \ln x_2) \qquad [2\text{-}32]$$

More specifically, Equation 2-32 is the entropy change arising soley from combinatorial considerations. The *ideal solution* is commonly used as a reference state for which thermodynamic properties of *real solutions* can be compared; thus, defining "excess" thermodynamic quantities that descibe the deviation of real solutions from the ideal state.

In the case where one component of the solution is a high molecular weight compound (as exists for polymer solutions) the i*deal solution* can no longer be used as a convenient reference state. Here, real solution behavior deviates too much from the ideal state. The reference state commonly used for polymer solutions is one for which the heat of mixing is zero (athermal solution) and the combinatorial entropy change is given by the Flory-Huggins lattice model/theory (17). In the theory, a lattice field is defined as the framework of the solution; furthermore, the volume of each site within the lattice is defined by the molar volume of the solvent which is assumed to be the same as that of the polymer repeat unit. By considering the number of possible lattice configurations for a mixture of polymer and solvent molecules the entropy of mixing per total number of moles is statistically determined to be:

$$\Delta S_m = -R(x_1 \ln\phi_1 + x_2 \ln\phi_2) \qquad [2\text{-}33]$$

where ϕ_i is the volume fraction of component i. One notes that the difference between Equation 2-32 and 2-33 is that in Equation 2-33 mole fractions have been replaced by volume fractions within the logarithmic term. For comparison, the combinatorial entropy change predicted by Equation 2-32 with x_2 equal to 0.4 is 0.67R; whereas, for a solution of identical fractional concentration where one component is a polymer (with a number average degree of polymerization of 500) the combinatorial entropy change predicted by Equation 2-33 is 2.7R (18). This difference in behavior of polymer solutions is why separate thermodynamic theories must be used for polymer solutions.

From Equation 2-33 the free energy of mixing can be obtained as

$$\Delta G_m = -RT(x_1 \ln\phi_1 + x_2 \ln\phi_2) \qquad [2\text{-}34]$$

In the full Flory-Huggins treatment for *real solutions* consideration is also given to a noncombinatorial (or thermal) free energy of mixing term. The lattice field continues to be the theoretical framework but the focus now is with the enthalpy changes accompanying the interchaging of species within the lattice sites. Moreover, only pairwise interactions are considered; hence, the notation for the chemical reaction upon mixing is given as

$$(1,1) + (2,2) \rightarrow 2(1,2)\,; \qquad \Delta h_{ij} = e_{ij} \qquad [2\text{-}35]$$

where 1 and 2 refer to the solvent molecule and polymer repeat unit respectively. It is the exchange energy in the above reaction for the i^{th} and j^{th} lattice site that gives rise to a heat of mixing, and by considering the above reaction for all sites within the lattice one obtains

$$\Delta H_m = zeN\phi_1\phi_2 = \chi_H RTN\phi_1\phi_2 \qquad [2\text{-}36]$$

where z is a coordination number of the lattice to account for the restriction of occupying certain sites adjacent to a polymer repeat unit (this is due to inherent connectivity of a polymer chain), N is the total number of sites within the lattice, ϕ_i is the volume fraction of component i and χ_H is the enthalpic part of the Flory-Huggins chi parameter The total free energy of mixing for *real solutions* now becomes

$$\Delta G_m = RT[\chi N\phi_1\phi_2 - (x_1 \ln\phi_1 + x_2 \ln\phi_2)] \quad [2\text{-}37]$$

where χ_H has been replaced by χ to include the entropic contribution to the free energy that arises from intermolecular interactions. By differentiating the above equation with respect to the number of moles of component 1 the change in chemical potential for the solvent is obtained as

$$\Delta\mu_1 = \mu_1 - \mu_1^o = RT[\ln(1 - \phi_2) + (1 - 1/i)\phi_2 + \chi\phi_2^2] \quad [2\text{-}38]$$

where i is the degree of polymerization. The thermodynamic activity is defined as

$$\ln a_i = (\mu_1 - \mu_1^o)/RT \quad [2\text{-}39]$$

and the activity of the solvent from the Flory-Huggins Theory now becomes

$$\ln a_i = \ln(1 - \phi_2) + (1 - 1/i)\phi_2 + \chi\phi_2^2 \quad [2\text{-}40]$$

2.5.3 The Hildebrand- Scatchard Theory of Regular Solutions

A *regular solution* is one for which the free energy of mixing is defined solely by: 1.) a combinatorial entropy term and 2.) an enthalpy term. It differs from an *ideal solution* only in that it contains a heat of mixing term. The intermolecular interactions that lead to a heat of mixing term must not be so large as to disrupt a random molecular disribution in the solution; consequently, *regular solutions* are best exemplified by systems limited to London dispersion forces. Table 2.8 characterizes the various types of solutions and their pertinent thermodynamic variables (19).

It was Heitler who first showed that the excess free energy of mixing (or ΔH_m) for *symmetrical regular solutions* could be given by

$$\Delta G_m^{ex} = (n_a + n_b)\, x_a\, x_b\, \varepsilon \quad [2\text{-}41]$$

where n_i and x_i are the number of molecules and mole fraction of species, i respectively, and ε is the exchange energy (20). It is interesting that in the derivation of the above equation - like that of Equation 2-37 - a lattice field was used as the framework of the model. In addition, because the mixing process results in a random distribution of molecular species, it easy to understand the origin of the $x_a\, x_b$ term in the above equation since $x_a\, x_b$ is simply the probability of a-b

Table 2.8. Various types of possible Thermodynamic Solutions.

Type of Solution	$H_1 - H_1^o$	$S_1 - S_1^o$	Remarks
Ideal	0	$-R\ln x_1$	$a_1 = x_1$
			$V_1 \sim V_2$
Regular	+	$-R\ln x_1$	$a_1 > x_1$
			$V_1 \sim V_2$
Athermal, nonideal	0	$> -R\ln x_1$	$a_1 < x_1$
			$V_2 >> V_1$
Associated (1 component)	+	$> -R\ln x_1$	$a_1 > x_1$
Solvated	-	$< -R\ln x_1$	$a_1 < x_1$

neighboring interactions within the lattice site, while the $n_a + n_b$ term considers the total number of sites within the lattice.

The above equation is well suited for the mixing of species of approximately the same size. When size dissimilarities exist between components one can intuitively recognize that the probability term should correct for this disparity. Scatchard, in 1931, extended Equation 2-41 to *unsymmetrical regular solutions* and derived an expression for the free energy of mixing as

$$\Delta G_m^{ex} = V\phi_1\phi_2\,\varepsilon' \qquad [2\text{-}42]$$

where V is the total volume of the solution and ϕ_i is the volume fraction of component i in solution. The Hildebrand-Scatchard equation now takes its form by considering the exchange energy term, ε'. In the derivation of an expression for ε', Hildebrand considered the mixing of two components resulting in a chemical reaction of the type given by Equation 2-35 ;therefore, ε' is given as

$$\varepsilon' = \varepsilon'_{11} + \varepsilon'_{22} - 2\varepsilon'_{12} \qquad [2\text{-}43]$$

Furthermore, Hildebrand made the assumption that ε'_{12} could be given as

$$\varepsilon'_{12} = (\varepsilon'_{11}\varepsilon'_{22})^{1/2} \qquad [2\text{-}44]$$

which is analogous with the geometric mean approximation used by London in the treatment of dispersion forces. Equation 2-42 becomes

$$\Delta G_m^{ex} = V\phi_1\phi_2\,[\,(\varepsilon'_{11})^{1/2} - (e'_{22})^{1/2}\,]^2 \qquad [2\text{-}45]$$

In Hildebrand's formalism ε' has dimensions of (energy)/(volume) and is therefore referred to as the cohesive energy density, e_{coh}, and results from the fact that in the derivation of Equation 2-45 it was assumed that intermolecular forces acted between the **centers** of the molecules (which is why ε has been primed to differentiate it from ε used in the chi parameter definition) (15). In its more familiar form Equation 2-45 appears as

$$\Delta G_m^{ex} = \Delta H_m = V\phi_1\phi_2\,[\,(\delta_1) - (\delta_2)\,]^2 \qquad [2\text{-}46]$$

The derivation of Equation 2-13 is now straight forward, by substituting Equation 2-36 into Equation 2-46 for ΔH_m and by recognizing that χ is defined by a temperature dependent term (χ_H) and temperature independent term (χ_S) or more specifically

$$\chi = \chi_H + \chi_S \qquad [2\text{-}47]$$

2.5.4 Estimation Methods for Chemical Properties (12)

2.5.4.1 Estimation of P_1^o

The equation used for the estimation of P_1^o has its basis with the Antoine Equation. In its final form it gives P_1^o for a pure compound as

$$\ln P_1^o = \frac{\Delta H_{vb} (T_b - C_2)^2}{\Delta z_b R T_b^2} \left[\frac{1}{(T_b - C_2)} - \frac{1}{(T - C_2)}\right] \qquad [2\text{-}48]$$

where ΔH_{vb} is the heat of vaporization at the boiling point, T_b is the boiling point, R is the gas constant, Δz_b is assumed to have a value 0.97, and C_2 is given by

$$C_2 = -18 + 0.19 T_b \qquad [2\text{-}49]$$

The average error using this method is 2.7%.

2.5.4.2 Estimation of V_1^L

Graine's method was used to estimate the liquid density of the probes at the column temperature. The method gives the liquid density of a compound as

$$\rho_L = M \rho_{Lb} [3 - 2(T/T_b)]^n \qquad [2\text{-}50]$$

where M is the molecular weight of the compound, ρ_{Lb} is the liquid density at the at the boiling point, T_b, T is the temperature of interest and the value of the exponent n depends on the chemical class of the compound. It is either equal to 0.25, 0.29, 0.31 if it is an alcohol, hydrocarbon, or other organic compounds respectively. The error in ρ_L is within 3-4%.

2.5.4.3 Estimation of δ_1 at 100 ^{o}C

δ_1 values were calculated using Equation [2-1]. The estimation of ΔH_v at 100 ^{o}C was done by using the Thiesen correlation which gives

$$\Delta H_v = \Delta H_{vb}\left[\frac{1-\left(T/T_c\right)}{1-\left(T_b/T_c\right)}\right]^n \qquad [2\text{-}51]$$

where ΔH_{vb} is the heat of vaporization at the boiling point, T_b, T_c is the critical temperature, T is the temperature of interest and n is an exponent whose value depends on the ratio of T_b/T_c. The general accuracy of the method is 2%.

2.5.5 Method of Group Contribution by Fedors for Calculation of δ

Using Fedors' method the solubility parameter is given by Equation 4 with the following values for the group contributions :

Group	E_{coh} (J/mol)	V (cm^3/mol)
$-CH_3$	4710	33.5
$-CH_2-$	4940	16.1
$\backslash CH- /$	3430	−1.0
$\backslash C / / \backslash$	1470	−19.2
$H_2C=$	4310	28.5
$-CH=$	4310	13.5
$\backslash C= /$	4310	−5.5
$HC\equiv$	3850	27.4
$-C\equiv$	7070	6.5
Phenyl	31940	71.4
Phenylene (o, m, p)	31940	52.4
Phenyl (trisubstituted)	31940	33.4
Phenyl (tetrasubstituted)	31940	14.4
Phenyl (pentasubstituted)	31940	−4.6
Phenyl (hexasubstituted)	31940	−23.6
Ring closure 5 or more atoms	1050	16
Ring closure 3 or 4 atoms	3140	18
Conjugation in ring for each double bond	1670	−2.2
Halogen attached to carbon atom with double bond	−20% of E_{coh} of halogen	4.0
−F	4190	18.0
−F (disubstituted)	3560	20.0
−F (trisubstituted)	2300	22.0
$-CF_2-$ (for perfluoro compounds)	4270	23.0
$-CF_3$ (for perfluoro compounds)	4270	57.5
−Cl	11550	24.0
−Cl (disubstituted)	9630	26.0
−Cl (trisubstituted)	7530	27.3
−Br	15490	30.0
−Br (disubstituted)	12350	31.0
−Br (trisubstituted)	10670	32.4
−I	19050	31.5
−I (disubstituted)	16740	33.5
−I (trisubstituted)	16330	37.0
−CN	25530	24.0
−OH	29800	10.0
−OH (disubstituted or on adjacent C atoms)	21850	13.0
−O−	3350	3.8
−CHO (aldehyde)	21350	22.3
−CO−	17370	10.8
−COOH	27630	28.5
$-CO_2-$	18000	18.0
$-CO_3-$ (carbonate)	17580	22.0
$-C_2O_3-$ (anhydride)	30560	30.0

...Method of Group Contribution by Fedors for Calculation of δ

Group	E_{coh} (J/mol)	V (cm^3/mol)
HCOO– (formate)	18000	32.5
$-CO_2CO_2-$ (oxalate)	26790	37.3
$-HCO_3$	12560	18.0
–COF	13400	29.0
–COCl	17580	38.1
–COBr	24150	41.6
–COI	29300	48.7
$-NH_2$	12560	19.2
–NH–	8370	4.5
	4190	–9.0
–N=	11720	5.0
$-NHNH_2$	21980	–
$-NNH_2$	16740	16
–NHNH–	16740	16
$-N_2$ (diazo)	8370	23
–N=N–	4190	–
	20090	0
–N=C=N–	11470	–
–NC	18840	23.1
$-NF_2$	7660	33.1
–NF–	5070	24.5
$-CONH_2$	41860	17.5
–CONH–	33490	9.5
	29510	–7.7
	27630	11.3
HCONH–	43950	27.0
–NHCOO–	26370	18.5
–NHCONH–	50230	–
	41860	–
	20930	–14.5
NH_2COO-	37000	–
–NCO	28460	35.0
$-ONH_2$	19050	20.0
	25120	11.3
–CH=NOH	25120	24.0
$-NO_2$ (aliphatic)	29300	24.0
$-NO_2$ (aromatic)	15360	32.0
$-NO_3$	20930	33.5
$-NO_2$ (nitrite)	11720	33.5
$-NHNO_2$	39770	28.7

References

1. Seymor, R.B., "Macromolecular Solutions Solvent-Property Relationships in Polymers", Seymor, R.B., (Ed.), Pergamon Press, New York, 1982.

2. Barton, A.F.M., Polymer Yearbook, 1st ed., Elias, H.G., and Pethrick, R.A. (Ed.), Harwood Academic, New York, 1984.

3. Rudin, A., "The Elements of Polymer Science and Engineering", Academic Press, New York,p. 432, 1982.

4. Van Krevelen, D. W., "Properties of Polymers" , 2nd edition, Elsevier Scientific Publishing Company, New York, 1976.

5. Hansen, C. M., "Macromolecular Solutions Solvent-Property Relationships in Polymers", Seymor, R.B. (Ed.), Pergamon Press, New York, 1982.

6. Guillet, J. E., "New developments in Gas Chromatography," Howard, P., (Ed.), Wiley, New York, 1973.
7. Guillet, J.E., and Lipson, J.E.G., "Development in POlymer Characterization", 3 rd ed., Dawkins, J.V. (Ed.), Applied Science, England, 1982.

8. Koning, P.A., Ph.D. Thesis, Virginia Polytechnic Institute and State University, 1988.

9. Ward, T.C., Class Notes Chem. #6671, Virginia Polytech. Inst. and Sttate Univ., 1987.

10. Aspler, J.S., "Pyrolysis and GC in Polymer Analysis", Dekker,1985.

11. Smith and Srivastava, "Thermodynamic Data for Pure Compounds", Elsevier Scientific Publishing Company, New York, 1986.

12. Lyman, W.J., Reehl, W.F., and Rosenblatt, D.H., "Handbook of Chemical Property Estimation Methods", Mc Graw Hill, New York, 1980.

13. Dymond, J.H., and Smith, E.B., "Virial Coefficients of Pure Gases and Mixtures', Clarendon Press, Oxford, 1980.

14. Guillet, J. E., and Lipson, J. G., J. Polym. Sci.: Polymer Phys. Ed., **19,** 1199-1209, 1981.

15. Barton, A. F., Chemical Reviews, **75**, 731, 1975.

16. Littlewood, A.B., "Gas Chromatography Principles Techniques and Applications", 2nd ed., Academic Press, New York, 1970.

17. Orwoll, R.A., Rubber Chem. and Technol., **50,** p.45,

18. Hiemenz, P.C., "Polymer Chemistry", Dekker, New York, 1980.

19. Hildebrand, J.H., and Scott, R.L., "The Solubility of Non-electolytes", 3rd ed., Dover Publications Inc., New York, 1964.

20. Lewis, G.N., Randall, M., "Thermodynamics", 2nd ed., Mc Graw Hill, New York, 1961.

CHAPTER 3

NITROCELLULOSE BLENDS

3.1 Background

Plasticizers are frequently added to polymers to either aid in processing or to lower their glass transition temperature. They are generally low molecular weight compounds that act to increase the free volume in a polymeric solid; therefore, a plasticized polymer will have a lower modulus, tensile strength and T_g but will have a higher impact strength and elongation (1). Yet, in certain cases - where intermolecular association is prominent- the addition of plasticizer can lead to antiplasticization effects; hence, while the T_g is lower and the local free volume is higher at elevated temperatures (where it has not been excluded by polymer-polymer association) for the overall system, specific intermolecular associations lead to an increased rigidity of the matrix material and a lower free volume at less elevated temperatures. Thus, a "cross-over" effect is seen, which may also be caused by stress.

The addition of a plasticizer to a polymer can have pronounced effects on the dynamic mechanical properties of the polymer. Referring to Figure 3.1 (2), when polyvinyl chloride is plasticized with diethylhexyl succinate there is a dramatic change in the shear modulus and damping (the significance of the damping factor, tan δ, is discussed in the next chapter). Specifically, the modulus curves and damping peaks are shifted to lower temperatures. It is also generally observed that the damping peak broadens with plasticizer addition, being broader for plasticizers that are poor solvents for the polymer as compared to those which are good solvents. Also, from Figure 3.1 one notes that plasticization tends to extend the rubbery plateau region. Thus, while plasticizers act to broaden and shift the transition region to lower temperatures, they also led to a compromise in the mechanical properties of the polymer. In addition, the volatility of a low molecular weight plasticizer may be a problem.

a)

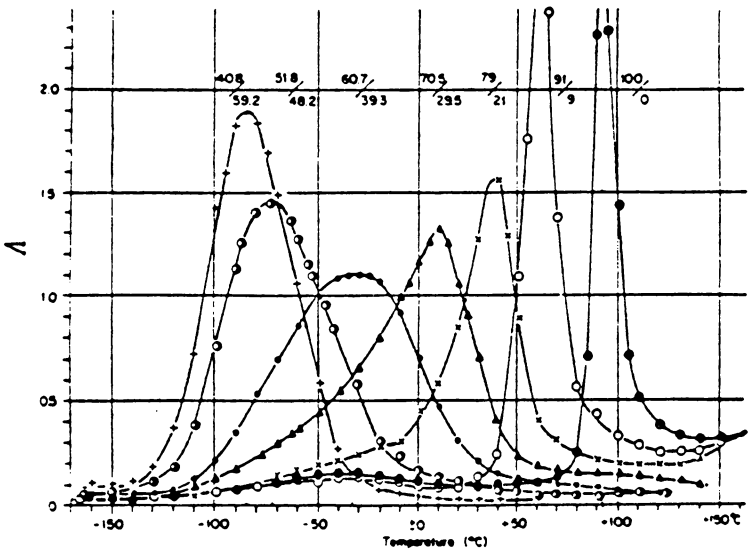

b)

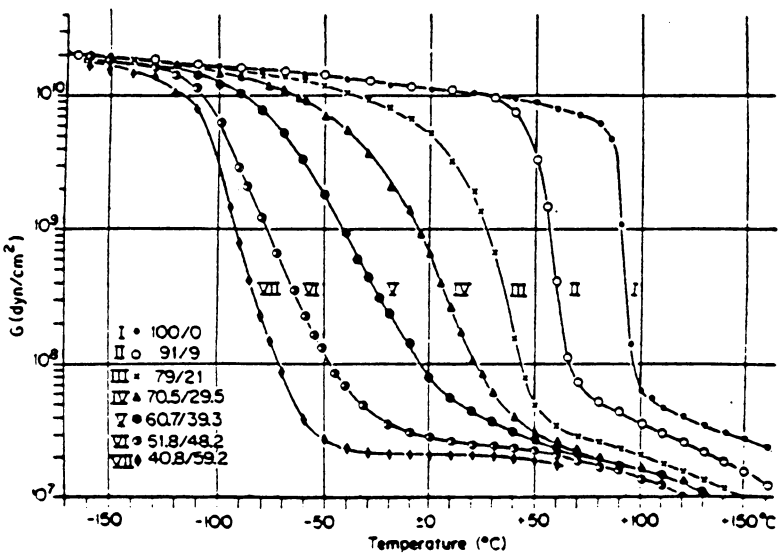

Figure 3.1. a). Damping response (Λ) of polyvinyl chloride (PVC) plasticized with diethylhexyl (DHS) succinate at various ratios of PVC to DHS
b). Effect of plasticizer on shear modulus of PVC at various compositions (2).

Polymer blends on the other hand offer the advantage that if the resultant blend is a one phase system, one may obtain a polymer mixture whose properties may be superior to its constituents. Clearly, blending offers versatility since it may be possible to obtain an array of properties that would be unique to a given pair of constituents. These resultant properties, of a polymer mixture, can usually be obtained from semi-empirical rules of mixtures. For many properties such as the glass transition temperature, density, refractive index, dielectric constant, surface tension and elastic moduli, the following relationship is found to hold for a quasi-binary miscible blend

$$P = P_1\phi_1 + P_2\phi_2 + I\phi_1\phi_2 \qquad [3\text{-}1]$$

where P is the property of interest of the blend, ϕ the concentration and I is an interaction term (2).

Yet, the fact is that most polymers are immiscible (here miscibility is characterized by a single phase with only one main transition, T_g) because the entropy of mixing for polymer blends approaches zero for high molecular weight polymers. This situation has directed the chemists to devise various synthethic methods for enhancing miscibility. These include not only block and graft copolymerizations but the formulation of interpenetrating networks. These methods are extensively discussed elsewhere (3).

There exist several thermodynamic theories aimed at describing miscibility (or phase separation) over a temperature and concentration domain. These are again discussed elsewhere (3), but the Hildebrand approaches will be introduced due to the discussions from the previous chapter.

For binary polymer blends the Gibbs free energy of mixing per unit volume is given as

$$\Delta G_{mix} = \phi_2\phi_3 (\delta_2 - \delta_3)^2 \qquad [3\text{-}2]$$

where δ_2 and δ_3 are the corresponding solubility parameters (2). The above equation implies that a difference in solubility parameters is a thermodynamically unfavorable situation and that for miscibility the polymers should have equivalent solubility parameter values. While the Hildebrand approach is limited in its practical uses, it does offer a convenient way to predict miscibility since it

depends only on the absolute property δ and not on a relative property such as the Flory-Huggins χ_{23} parameter.

3.2 Introduction

In this study several blends of propellant grade nitrocellulose were studied by dynamic mechanical analysis and isochronal stress-strain experiments. The objective was to formulate a system that would exhibit a broad transition over the -50°C to 70°C temperature range with good mechanical strength. The systems studied were based on a novel block copolymer of polydimethyl siloxane and poly(caprolactone). Poly(caprolactone) has been reported to be miscible over the entire concentration range with nitrocellulose (NC) (4,5), but polydimethyl siloxane is not. Hence, the block copolymer offered the miscibility properties of polycaprolactone and the low temperature properties of polydimethyl siloxane. Indeed both binary and ternary NC-based systems were studied with the above block copolymer and suitable plasticizers. Table 3.1 lists all the blend components studied along with their Hildebrand solubility parameter values. Dimethyl phthalate, di-normal propyl adipate and polycaprolactone are all known to be miscible with nitrocellulose and show similar δ values as 13.5% N nitrocellulose. Polydimethyl siloxane though has a low solubility parameter which explains its immiscibility with nitrocellulose. The results from the previous chapter revealed that nitrocellulose of different nitration levels may be blended to offer a resultant material whose solubility parameter may better match that of its blending counterpart; though, this route was not pursued in this study. Only pure 13.5% N nitrocellulose was used in this study.

3.3 Experimental

3.3.1 Sample Preparation

Water packed nitrocellulose of 13.5% nitration level was supplied by Hercules, Inc.. Five grams of wet nitrocellulose was filtered and rinsed with commercial grade ethanol through a Buchner funnel in order to remove excess water. The sample was then dried in a vacuum oven at

Table 3.1. Hildebrand Solubility Parameters of blend components

Sample	Solubility Parameter $(cal/cm^3)^{1/2}$
Poly(dimethylsiloxane)	7.60 (3)
Dinormal-propyl adipate	10.03 (7)
Poly(caprolactone)	9.43 (7)
Dimethyl phthalate	10.70 (8)

50°C for 6-8 hours. Nitrocellulose films of varying blend composition were then prepared from the dry NC.

The $(AB)_n$ block copolymer of caprolactone and dimethyl siloxane (BCP) was obtained from Mercor, Inc.. The overall number average molecular weight was 6080 g/mole and each block had a molecular weight of about 1000 g/mole. The plasticizers used (dimethyl phthalate and di-normal propyl adipate) were obtained from Aldrich.

Blended films were obtained by solution casting from acetone and tetrahydrofuran; in addition, 0.5% stabilizer (Akardit II) was added to all mixtures. Films were cast onto a clean glass surface with a doctor's blade. In order to obtain films with an adequate thickness for study, multiple layers of approximately 5 mils were cast onto one another. Films were dried for 8-12 hours under a watch glass in order to avoid differential evaporation. Finally the films were dried in a vacuum oven at 50°C overnight.

3.3.2 Dynamic Mechanical Analysis

The instrument used was a Dynamic Mechanical Thermal Analyzer (Polymer Laboratories' D. M. T. A.). The D. M. T. A. allows for a variety of clamping modes; with the choice of clamping mode being dictated by the sample dimensions. Scans are normally done over a temperature range at a given frequency; the temperature is monitored via a platinum resistance thermometer mounted behind the sample. The damping (tan δ) range is from 0.0001-9.9999 while the Young's modulus range is from 10^5 N/m^2 to 10^{11} N/m^2.

In a dynamic mechanical test, the material is subjected to a sinusoidal force and the response of the material is measured (strain). From this the dynamic storage modulus and damping factor of the material can be determined. The nitrocellulose samples (and blends) were studied from sub-ambient temperatures to 100°C at a frequency of 1 Hz. Samples were studied in both a single and dual cantililever clamping mode; the method depended on the resultant film thickness. The D. M. T. A. was interfaced to an HP computer which provided for instrument control and data processing.

PL-D. M. T. A. Technique (8)

The D. M. T. A. applies a sinusoidal stress to the sample by supplying a sinusoidal current to a vibrator unit. The displacement of the sample is then monitored by a non-contacting eddy current transducer. Since the experiment is of non-resonance forced vibration type the following equation describes the motion of the system

$$F_p \sin \omega t = M\ddot{x} + \left(\eta + \frac{S''}{\omega} + \frac{kE''}{\omega}\right)\dot{x} + (S' + kE')\,x \qquad [3\text{-}3]$$

where the following terms are defined

F_p = peak force from vibrator (N)

m = vibrating sysem mass (Kg)

E' = storage modulus of sample (Pa)

E" = loss modulus of sample (Pa)

s' = elastic response of suspension (Pa)

s" = viscous response of suspension (Pa)

η = a viscous damping term (mostly due to air of the mechanical spectrometer (Pa.s)

x = axial displacement (m)

K = sample geometry factor (m)

ω = angular frequency = $2\pi f$

t = time (s)

The solution to the above equaton gives both the in phase ($K_a \cos\beta$) and out of phase ($K_a \sin\beta$) response of the entire system as

$$K_a \cos\beta = kE' - M\omega^2 + S' \qquad [3\text{-}4]$$

$$K_a \sin\beta = kE'' + \omega\eta + S' \qquad [3\text{-}5]$$

where $K_a = F_{(peak)}/X_{(peak)}$. The instrument actually measures $K_a\cos\beta$ and $K_a\sin\beta$ and from calibration the values of M, s', s" and η are determined; thus, KE' can easily be obtained (dynamical mechanical analysis of polymers is discussed further in Chapter 4).

3.3.3 Stress-Strain Experiments

Blended nitrocellulose films were cut into dog bone shapes 3 mm in width and 10 mm in length. The samples were dried in a vacuum oven for 3 hours at 50°C. The samples were then conditioned in a constant humidity chamber (ASTM E104-51) of 50 ± 0.2% relative humidity for 24 hours. Three samples from each film were studied on an Instron Universal Tester. The load deformation data was averaged then compiled to stress-strain curves for each film. The draw rates were at 10 mm/min, chart speed was at 500 cm/min and full scale load was 5 kg. In addition, all samples were tested at room temperature conditions.

3.4 Results and Discussion

3.4.1 Dynamic Mechanical Analysis

Because the blends were based on the BCP, initial interest was in attaining the minimum BCP content required to yield a broad transition over the -50 to 70°C temperature range. Figure 3.2 is the tan δ versus temperature plot for the BCP/NC system. The composition range studied was 5-40 wt/wt % BCP. From the figure one notes that at least 40% BCP is required to yield a broad transition; yet even at 40 wt/wt% BCP the transition does not extend lower than room temperature. In the subsequent studies the blending constituents were limited to a 40% concentration since the original goal was to keep these to a minimum.

A blended film of dimethyl phthalate (DMP) at a composition of 40 wt/wt% was run for comparison of performance to that of the 40 wt/wt % BCP; the results are shown in Figure 3.3. The glass transition is at 22°C which is 25°C lower than that of the BCP blend system of the same composition. These results suggested that ternary systems based on not only the BCP but also on a

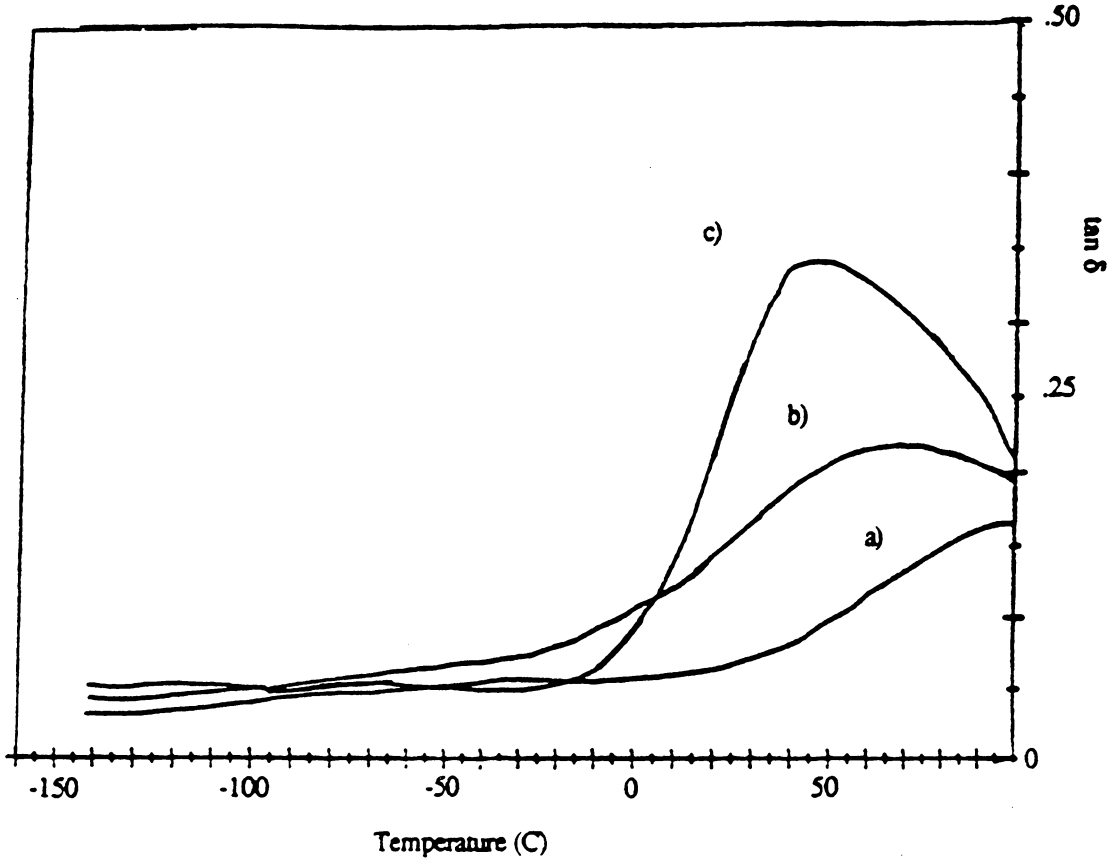

Figure 3.2. Tan δ versus temperature plot for blended film of nitrocellulose and BCP at various blend concentrations: a). 5 wt/wt% BCP b). 15 wt/wt% BCP c). 40 wt/wt% BCP

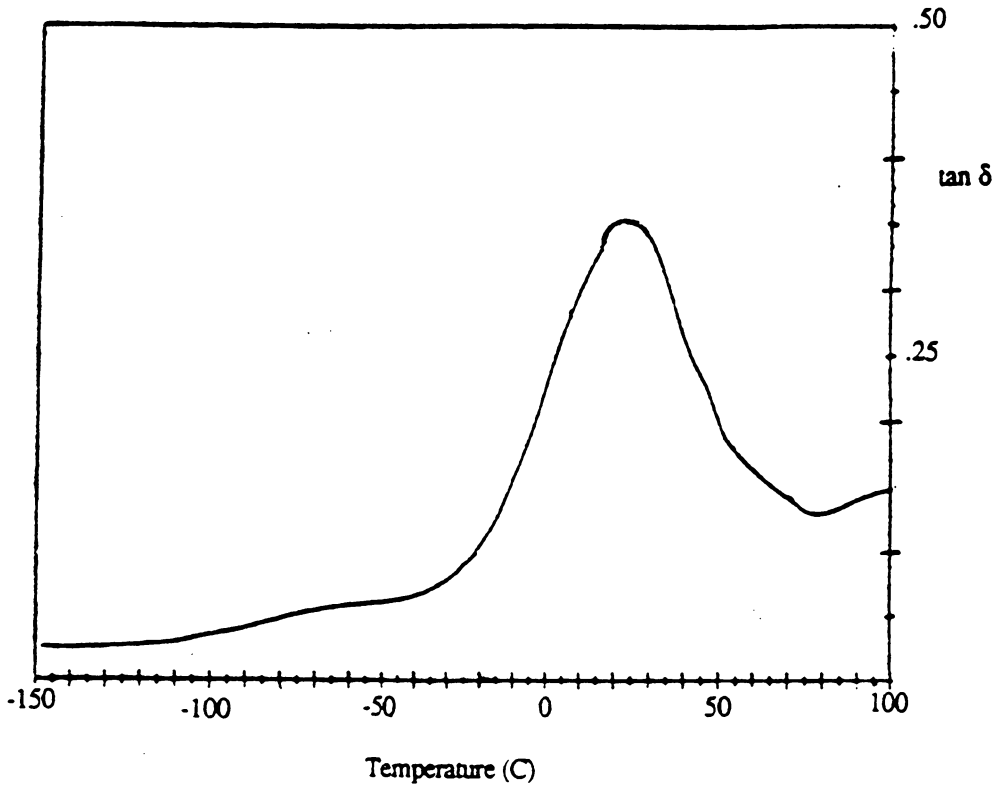

Figure 3.3. Tan δ versus temperature plot for blended film of nitrocellulose and DMP of 40 wt/wt% DMP composition.

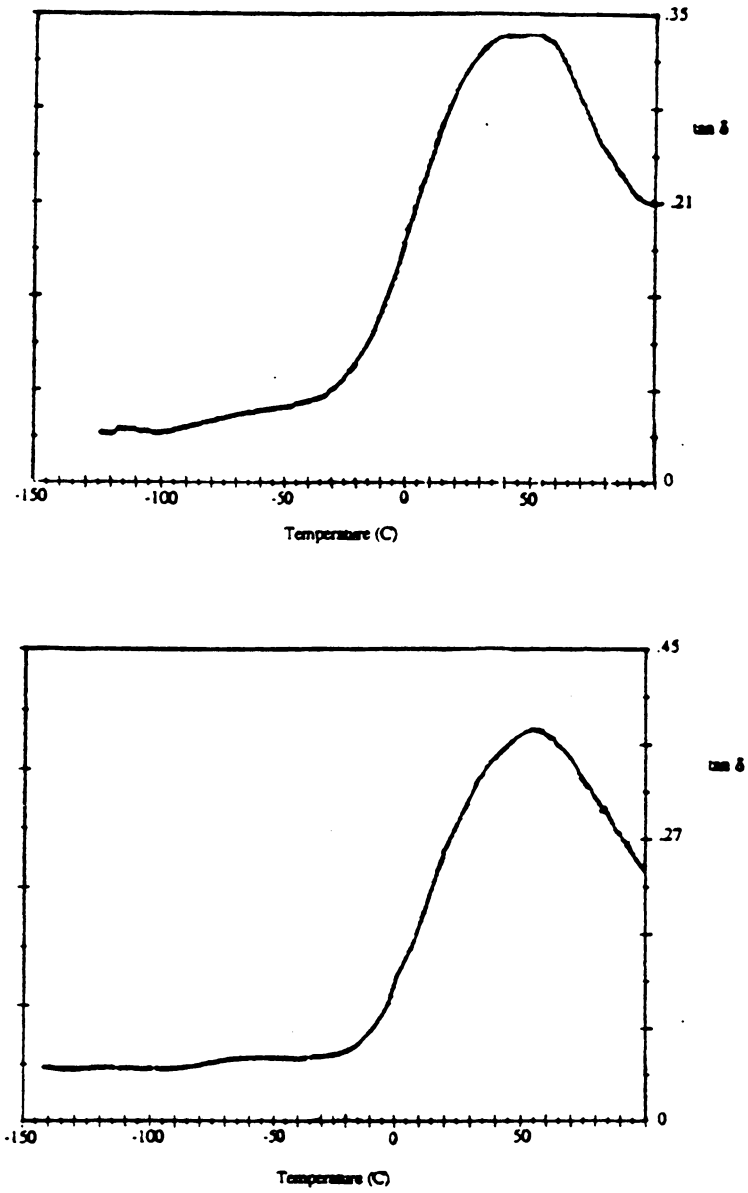

Figure 3.4. Tan δ versus temperature plot for ternary blends of nitrocellulose and BCP : a). 15 wt/wt% Di n-propyl adipate and 25 wt/wt% BCP b). 15 wt/wt% DMP and 25 wt/wt% BCP

low molecular weight plasticizer might offer a better balance of properties, that could extend the transition over a broader temperature range. Indeed two ternary blends studied proved to be effective in broadening the α-transition. Dinormal propyl adipate (15 wt/wt%) and 25 wt/wt% BCP were blended with the 13.5% N nitrocellulose; the results are shown in Figure 3.4a. The T_g for this blend is at about 50°C. Although it is slightly higher than the 40 wt/wt% BCP, the transition is seen to extend to lower temperature. In addition, 25 wt/wt% of BCP and 15 wt/wt% of DMP was blended with nirocellulose. The resultant film exhibited the results shown in Figure 3.4b. This film displayed similar behavior to the film in 3.4a - extending the transition to lower temperatures.

The ternary blend of a 20 wt/wt% DMP and of 20 wt/wt% BCP composition proved to be the best blending composition since it yielded the broadest glass transition extending from -40 ^{o}C to + 100 ^{o}C. The tan δ versus temperature plot for this film is shown in Figure 3.5a.

For comparison, in Figure 3.5b the viscoelastic response of a small sample of propellant is shown. The response of material served as a standard from which the blends studied could be compared. For this film this material exhibits two transtions that overlap with one another extending the low temperature dispersion to -50°C. These results are comparable to those shown in Figure 3.5a.

3.4.2 Stress-Strain Experiments

Isochronal stress-strain experiments were performed on the blended nitrocellulose films. From the stress-strain curves the Young's modulus was determined along with the ultimate properties-the stress and strain at break values. Figure 3.6 shows the stress strain curves for the samples in Table 3.2. From the curves one notes that no sample showed yielding behavior. The Young's modulus was determined from these curves by assuming Hookean behavior in the low strain-linear elastic region of the stress-strain curve.

These results are shown in Table 3.2 along with the stress and strain at break. The Young's modulus for the reference material was the lowest among the films studied, while the blended film

a)

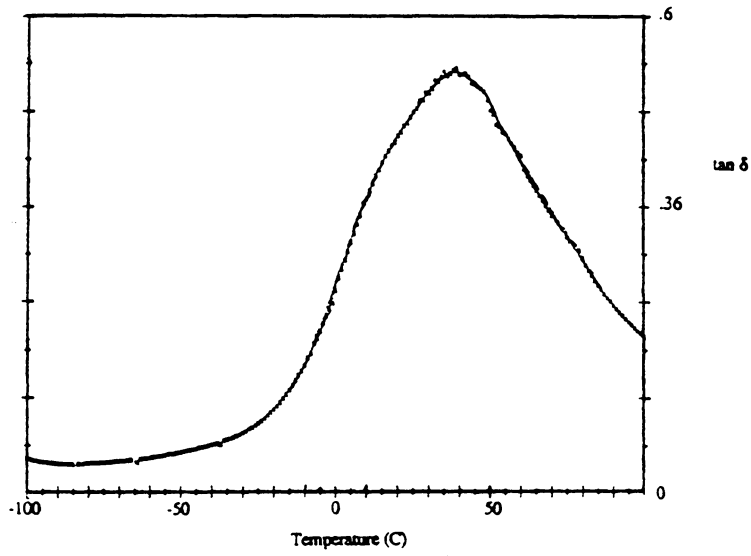

b)

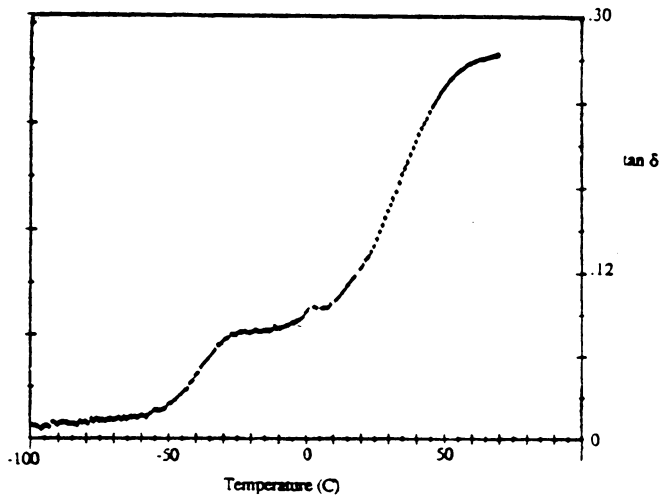

Figure 3.5. Tan δ versus temperature plot for a). ternary blend of nitrocellulose and BCP of 20 wt/wt% DMP and 20 wt/wt% BCP composiltion and b). standard double base propellant material.

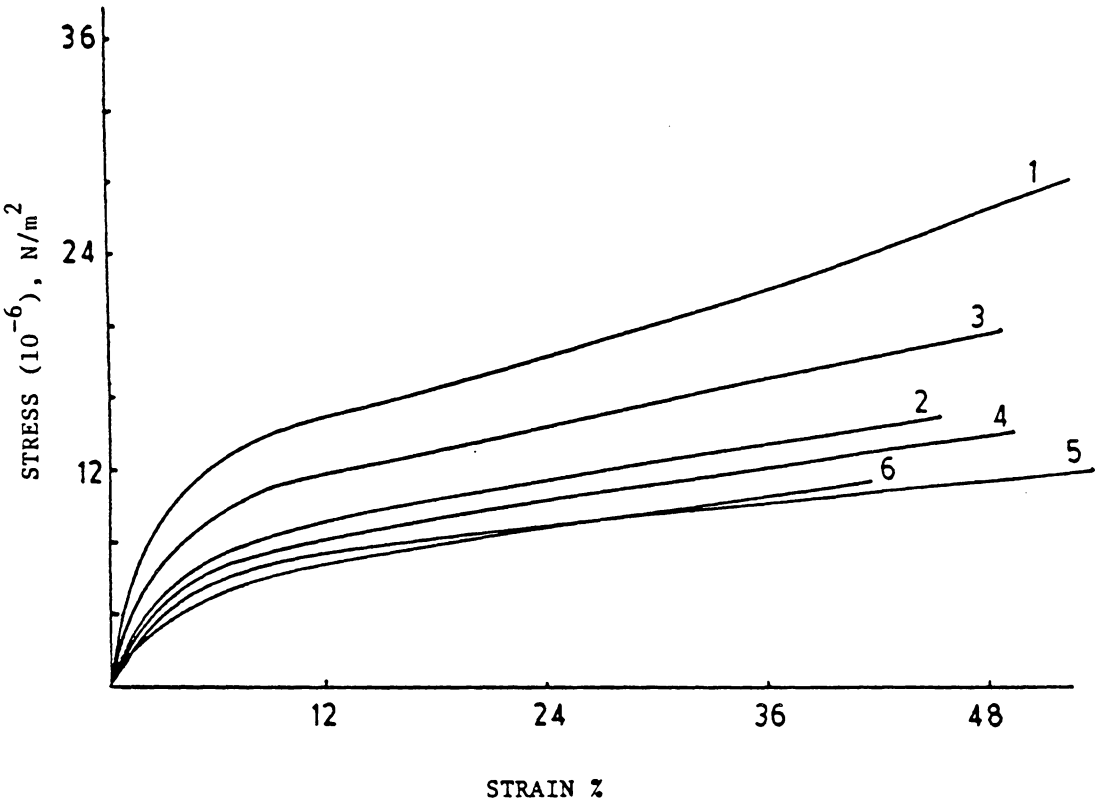

Figure 3.6. Stress-Strain curves for nitrocellulose blends where sample numbers correspond to those listed in Table 3.2.

Table 3.2. Mechanical properties of nitrocellulose blends from the stress-strain curves shown in Figure 3.6.

CONTENT	Sample	Young's Modulus E' N/M^2	Elongation at Break (%)	Stress at Break (N/M^2)
NC w/ 40% BC	1	3.34×10^8	52.30	2.84×10^7
NC w/ 25% BC + 15% DNPA	2	1.91×10^8	45.53	1.52×10^7
NC w/ 25% BC + 15% DMP	3	2.55×10^8	48.70	2.00×10^7
NC w/ 20% BC + 20% DMP	4	1.80×10^8	49.37	1.43×10^7
NC w/ 15% BC + 25% DMP	5	1.41×10^8	53.77	1.24×10^7
RAAP sample	6	9.65×10^7	41.5%	1.14×10^7

of 40 wt/wt% BCP had the highest modulus value. The former film also had the highest stress at break and among the highest strain at break values. From the table, one notes that the binary blend film had superior mechanical performance to either the ternary blends films or the reference material.

Moreover, among the ternary blends studied, the films with only 15 wt/wt% of plasticizer had superior mechanical properties than those with higher plasticizer content (the 20 wt/wt% DMP/20 wt/wt% BCP film). This is consistent with what one would expect.

3.5 Summary and Conclusions

The results revealed that nitrocellulose could successfully be blended with a block copolymer of polycaprolactone and polydimethyl siloxane as solubility parameter theory would predict. Furthermore, ternary blend systems (with the BCP and low molecular weight plasticizer) offered a broader temperature dispersion but yielded materials that had lower modulus and stress at break values than the binary blended film of 40 wt./wt.% BCP. Yet, all the blended films studied had improved mechanical properties compared to the standard material.

REFERENCES

1. Sears, J.K., and Touchette, N.W., Encyclopedia of Chemical Technology, John Wiley, **18**, 111, 1982.

2. Nielson, L.E., "Mechanical Properties of Polymers and Composites", **1**, Dekker, New York, 1974.

3. Olabisi, O., J. of Chem. Ed., **58**(11), 944, 1981.

4. Olabisi, O., Robeson, L.M., and Shaw, M.T., "Polymer-Polymer Miscibility," Academic Press, New York, 1979.

5. Brode G.L. and Koleske, J.V., J. Macromol. Sci. Chem., **6**(6), 1109, 1972.

6. Cooper, S.L. and Hubbell, D.S., J. Poly. Sci. : Polymer Phys. Ed., **15**, 1143, 1977.

7. Van Krevelen, D.W., "Properties of Polymers", Elsevier Scientific Publishing Co., New York, 1976.

8. "Polymer Handbook", 2nd ed., Brandrup, J., and Immergut, E.H., Ed., Wiley, New York, iv-342, 1975.

9. Polymer Laboratories' Dynamic Mechanical Analyser Instruction Manual, Polymer Laboratories Ltd., England, 1986.

CHAPTER 4

RELAXATION PROPERTIES OF THIN FILM COATINGS: THE ROLE OF SURFACE TOPOGRAPHY

4.1 Background

The objective of the following research is to gain insight into the fundamentals of adhesion by examining the relaxation properties of thin film polymer coatings on substrates of various surface topographies. The research is specifically concerned with *adherate properties* in *adhering systems.* Mittal has differentiated the term adherate from adhesive in that an adherate is a material that adheres to one adherend while an adhesive is a specific type of adherate in that it adheres to two adherends (1); in addition, the term adhering system is specific to combinations where an is adherate adhering to one adherend only. The clarification of these definitions serves only to exemplify the extent of situations involved in adhesion where research concerning adhering systems may or may not aid in understanding factors pertinent to practical adhesion in adhesive joints. This is because the behavior of adhesive joints is far more complex than that of adhering systems. Yet, the importance of understanding adherate properties can be justified when one considers that the locus of failure in most adhesive joints is cohesive; either in the adhesive, adherend or in both (1).

4.1.1 Surface Topography

The difficulties involved in understanding factors pertinent to adhesion are manifested in the variety of theories proposed as adhesion mechanisms. These include the mechanical interlocking, adsorption, diffusion, electostatic and chemical bonding theories. Although, all of these theories have been discussed elsewhere, the mechanical interlocking theory will be considered here (2,3). In the mechanical interlocking theory the substrate roughness provides a mechanical locking of the adherate and an increase in surface area for bonding (3). Venables has examined the importance of surface topography in adhesion by high resolution scanning transmission electron microscopy for aluminum epoxy systems where whisker protrusions in the aluminum oxide were found to enhance adhesive bond strengths (4). More recently, Packham has reviewed the role of surface topography

in the adhesion of polymers to metals (5). He reports that the increased adhesion with rougher sufraces can occur by either directing the fracture surface along a more tortuous path or by changing the stress distribution at the interface to involve increased volumes of polymer in plastic deformation during fracture. Specifically, Packham looked at the adhesion of polyethylene hot melts onto anodized aluminum surfaces. The anodization of the aluminum with acids such as sulphuric or phosphoric resulted in a porous oxide surface with a close-packed hexagonal array of oxide cells which extend from the top surface to the metal (5). The morphology of the resulting oxide depended on the anodizing conditions and electrolyte used, while the thickness of the oxide porous layer was a function of the current density and time of anodization. It was found that the porous oxide layer could be on the order of a micron or more in thickness. A characteristic structure of an anodic oxide film formed on aluminum in 10% phosphoric acid at 10V for 25 minutes, as proposed by Venables is shown in Figure 4.1 (4). The fibrous projections of the oxide at the edges were noted to be less prevalent with pure aluminum. In the case of the polyethylene melts on anodized aluminum, Packham observed that adhesive failure occurred within the polymer, which showed cold drawing on the fracture surface. He proposed that the pores in the anodic film provided discontinuities on the substrate surface which resulted in nuclei for plastic yielding of the adherate. This in turn resulted in higher peel strengths. In addition, the interpenetration of polymer into the porous oxide was noted to contribute to bond durability; the resulting resin-metal oxide composite interphase was proposed to be the reason. Other suface topographies were examined by Packham (such as surfaces with fiber-like topography) and were cited as cases where adhesion was improved by the roughness of the adherend. Yet, one must realize that surface roughness can lead to poorer adhesion especially when bonding is accompanied by incomplete wetting. Here, surface roughness can lead to uncoated areas or voids which can act as stress concentrators leading to centers of failure.

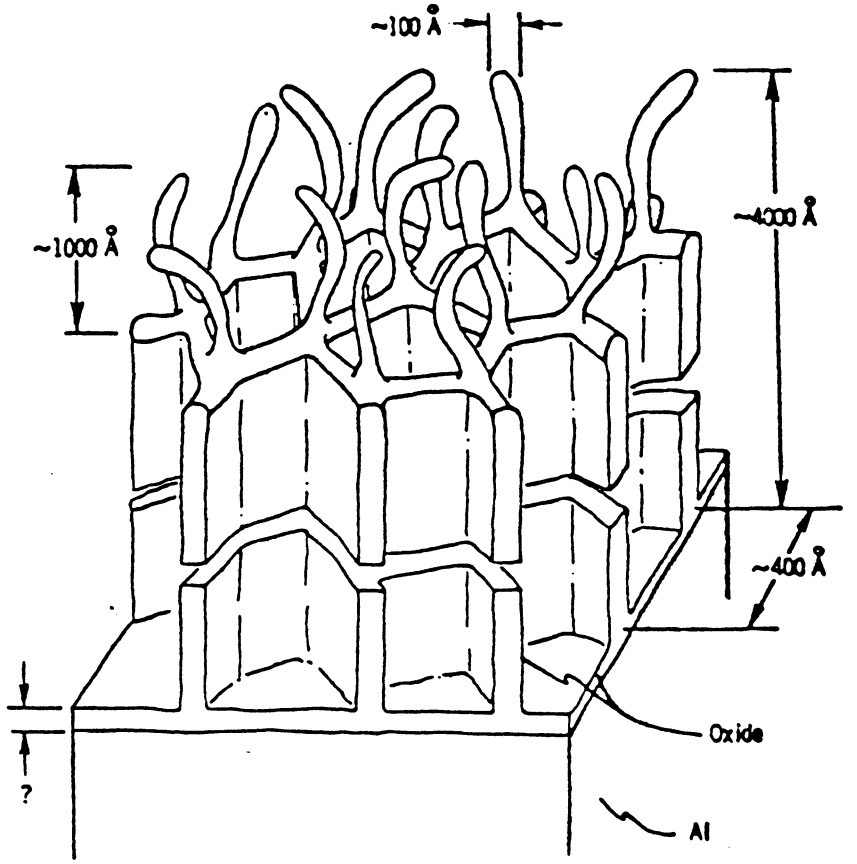

Figure 4.1. Proposed structure for anodic aluminum oxide layer(4).

4.1.2 Interphase Region

The case of an adhering system (i. e. coatings and paints) can be viewed as a special case of composites in general, where fibers or fillers are interdispersed in a polymeric matrix. Thus, one may wonder whether effects or anomalies observed in composite material behavior might be observed in the case of adhering systems. In particular the questions as to whether the linear viscoelastic properties of a composite are affected by the filler volume and the degree of adhesion between filler and polymer may also be pertinent in the case of adhering systems.

In the case of particle composites, mathematical models have been developed to describe their linear viscoelastic properties and the influence that a defined interphase (between filler and polymer) can have on the resulting composite properties. Throughout the text "interphase" will refer to region between two phases while interface will refer to a plane between two phases. By introducing the concept of an interphase Theocaris and Spathis were able to explain the effect of fillers on the glass transition temperature, T_g, of the composite (6). Their premise was that a phase, which has different properties than the bulk matrix material, is created from matrix material surrounding each particle of the filler. Specifically, they proposed that the interphase region possessed different viscoelastic properties than the bulk material, namely in the glass transition temperature. The T_g of the interphase was thought to depend on the adhesion between filler and matrix, with higher T_g's occurring for higher degrees of adhesion. The T_g of the resultant composite was therefore determined by the combination of the T_g of the interphase and T_g of the bulk matrix. Their arguments were supported by work done by Yim, Chahal and St. Pierre on polydimethylsiloxane, polystyrene and polyethylene glycol where a direct correlation between the increase in T_g by silica filer (measured by dielectric relaxation) and filler-polymer interaction energy (obtained by heats of adsorption) was obtained (7). Figure 4.2 is an example of their results. In addition, there are other property modifications caused by filler dispersion which have been noted.

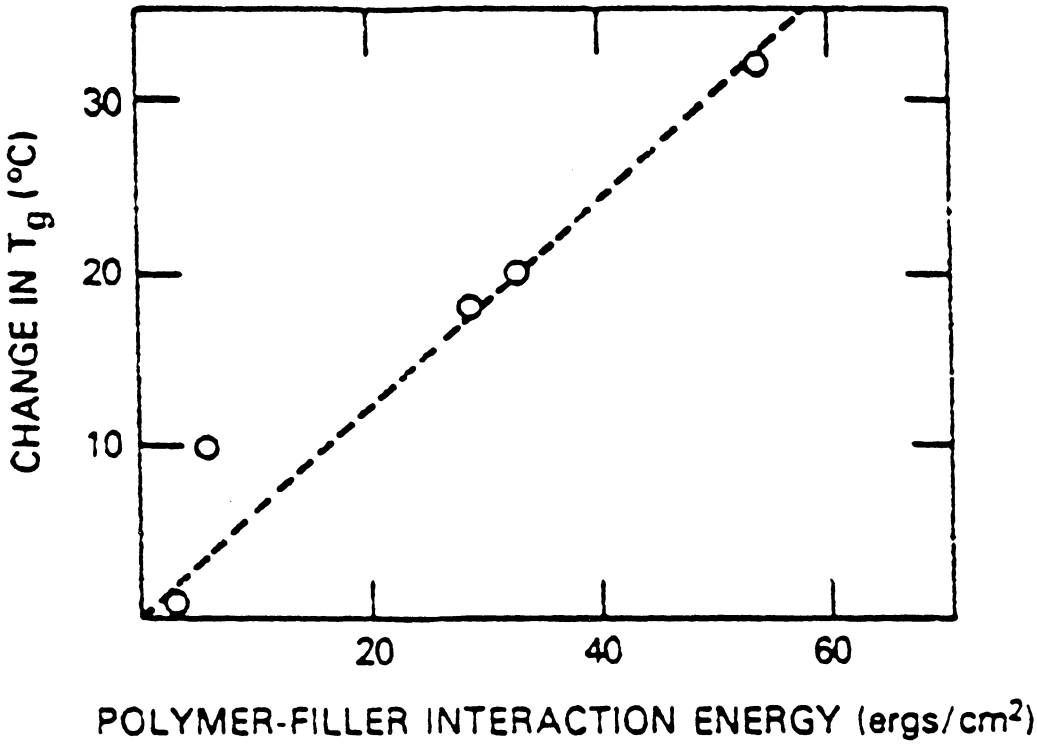

Figure 4.2. Relationship between change in T_g (compared to unfilled material) and filler-polymer interaction energy (5).

evidence,as reviewed by Peyser, also showed that an increase in T_g and longer relaxation times are observed in composites due to filler effects (8).

The consequences arising from the concept that polymer properties can be altered in the vicinity of the polymer-filler interface are crucial especially in the area of adhesion, where the role of filler is taken by the adherend (usually a metal substrate). Since adhesive bond and failure models are usually based on the assumption that the mechanical properties of an interfacial adhesive layer are constant throughout the interphase, the importance of the interphase region is obvious and leads to several important questions two of which are: (1) Is there a gradient in material properties as one progresses from the adherend to the adhesive?, and (2) How do surface pretreatments affect the properties in the vicinity of the interphase region?

4.1.3 Material Property Gradients

There have been attempts at answering these questions in the case of thermoset adhesives. Knollman and Harthog at Lockheed Research Laboratories have used the technique of ultrasonic Rayleigh waves to determine the shear modulus of an Epoxylite 810 and FM73 epoxy adhesive as a function of adherate thickness (9,10,11). They found that a shear modulus gradient existed which extended out to about 250 μm from the adherend surface where the adherate properties resembled those of the bulk. In another study, Knollman and Harthog found that the extent of the material property gradient was dependent on the substrate pretreatment for an FM73-aluminum adhering system (12). These results are shown in Figure 4.3. The three pretreatments of the aluminum substrate include a Forest Products Laboratory acid etch (FPL), a surface treatment for aluminum bonding (STAB which is an alkaline pretreatment), and Boeing Aircraft Company phosphoric acid anodization (BAC). From the figure, one notes that the BAC pretreatment lead to a larger gradient extending out about 60 μm further than the other pretreatments. In addition to mechanical property gradients observed in thermoset adhering systems, dielectric relaxation gradients have been

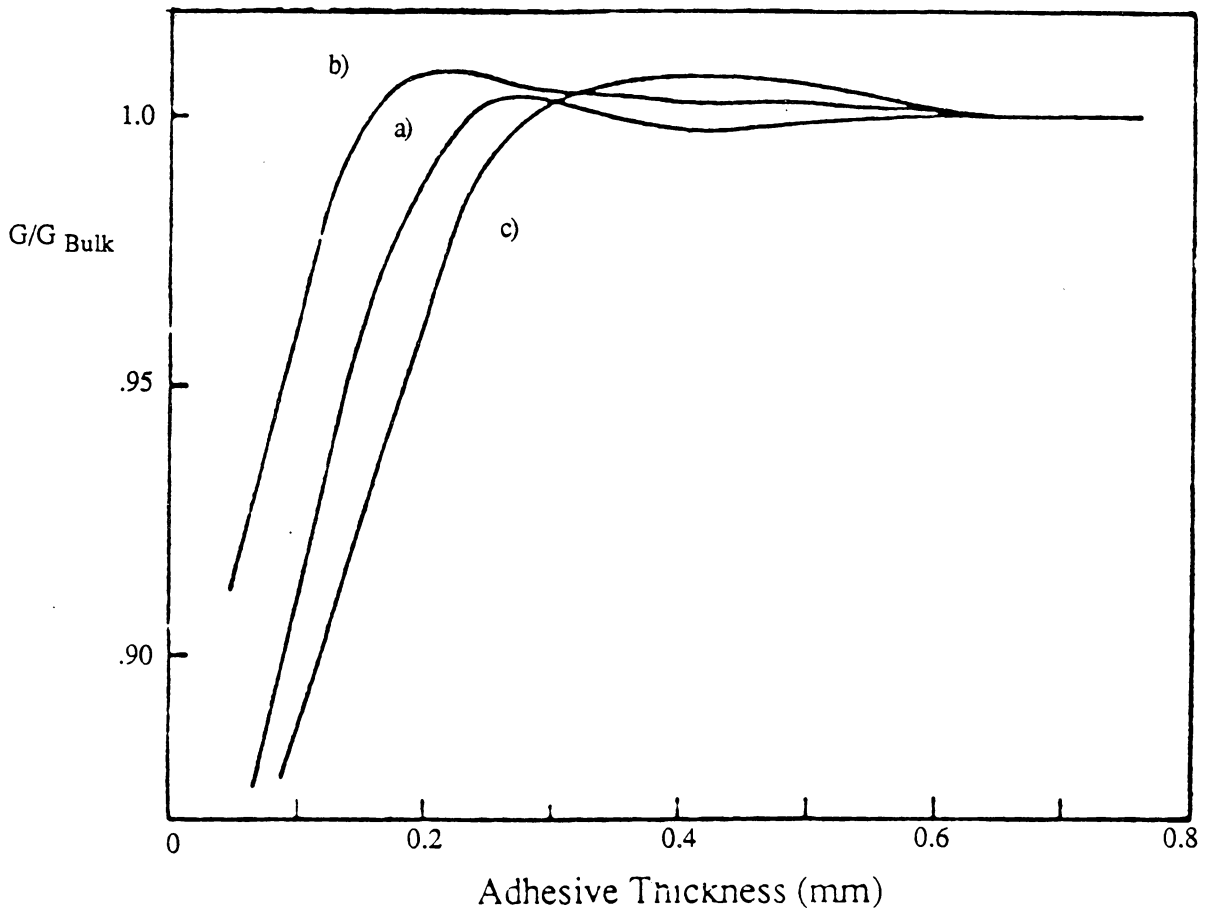

Figure 4.3. Normalized shear moduls vesus adhesive bond thickness for an FM 73 adhesive (4 hr. cure at 120 ^{o}C) for : a). FPL pretreatment, b). STAB pretreatment, and c). BAC pretreatment (12).

observed for filled epoxy adhering systems. Crowley and Jonath have used Thermally Stimulated Dielectric Relaxation, TSDR, to probe the microsturctural relaxation in an aluminum-epoxy bond (13). Their research was aimed at a possible explanation for why with Mode II (shear) failure, the fracture surface is found within the adhesive but near the adhesive-adherend interface, whereas with Mode I failure (opening) the fractured surface occurred at the center of the bondline. Crowley and Jonath. found that a dipole density gradient existed in the aluminum-epoxy systems, and that the gradient extended out to 200 μm from the adherend surface. The authors offered two possible explanations for the phenomena: (1) differences in the chemical composition near the interphase as compared to the bulk of the adhesive; or (2) immobilization of dipoles in the interphase due to a chemical bonding process. Yet, from the work done by Knollman and Crowley et al., the origin of the material property gradients is not clear, since in both cases the research was on thermosetting systems whose cure anomalies near the interface could have given rise to their observations.

4.1.4 Importance of Sample History

One is lead to the recognition that in order to gain a fundamental understanding of properties near the adhesive-adherend interface, the influence of sample history must be factored out of the analysis. Indeed, the importance of sample history cannot be overstated especially where viscoelastic properties are concerned. Peyser and Bascom studied the effect of thermal history on particle composites of polystyrene filled with silica (14). They found that the change in T_g by filler depended on whether the sample had been annealed and on the cooling rate. Their work emphasized the importance of thermal history and kinetic effects. To further complicate matters, physical aging effects can also affect the viscoelastic response of a polymeric material. There are adequate reviews of the physical aging phenomena in glassy systems (15,16) and it is reasonable to assume that such behavior of glassy systems (with respect to physical aging) would be different in a neat material when compared to a bonded material in adhering or adhesive joints.

4.2 Introduction

The sections reviewed above, namely, surface topography, the interphase region and material property gradients demonstrate the complexities involved in understanding adhesion and serve to explain why an interdisciplinary approach was taken to address adhesion problems and phenomena. From the point of view of this research, concern was with the viscoelastic properties of thin polysulfone coatings on both a smooth and porous aluminum surface as compared to the bulk material properties. Since polysulfone is an amorphous thermoplastic, it was hoped that chemical and morphological inhomogeneities near the interphase would be avoided. The viscoelastic techniques employed were dynamic mechanical and dielectric thermal analysis. Surface analysis included x-ray photoelectron spectroscopy (XPS) and scanning electron microscopy (SEM) which provided information of the interphase chemistry and morphology respectively. In addition to examining the role of surface topography on the viscoelastic properties of adhering systems, studies of the Arrhenius activation energy (ΔH^*) and its dependence on adhesive thickness were done to elucidate whether a gradient of viscoelastic properties existed in the coated systems.

4.2.1 Dynamic Experiments of Polymers

The viscoelastic nature of polymers arises from the fact that polymers are neither completely elastic nor viscous in behavior. Hence, in the realm of small mechanical deformations their behavior is neither represented by Hooke's law nor in the realm of low rates is their behavior represented by Newton's law of viscosity. Polymer behavior, therefore, is similar to both that of viscous liquids and elastic solids, and because of this there is a time and temperature dependence of the mechanical and physical properties of polymers. Considering the glass transition temperature, one will find that as the time scale of the experiment is decreased the apparent T_g will increase. As a result of this time dependence (of polymer properties) there exists several experimental methods to probe the viscoelastic properties of polymers. If one is interested in long time results of hours or days, transient experiments such as creep and stress relaxation would be suitable, on the other hand

information regarding short time response (seconds to milliseconds) can be obtained from dynamic experiments such as dynamic mechanical and dielectric techniques.

Of the often used techniques in characterizing viscoelastic materials, dynamic mechanical thermal analysis (D. M. T. A.) and dielectric thermal analysis (D. E. T. A.) can provide information on changes in molecular motions and material property transitions. Dynamic experiments differ from transient experiments in that the sample perturbation is periodic. If for instance a small sinusoidal stress is applied to a viscoelastic sample then the strain is monitored. Although the strain will also respond in a sinusoidal manner, it will generally lag the stress by some phase angle, δ, which will be temperature and frequency dependent. Figure 4.4a illustrates this principle schematically for a dynamic mechanical experiment (17). This lag in response of the material is caused by energy dissipative molecular motions (of diffusional character) that couple with the imposed stress energy at a given frequency (f) and temperature (T). While many types of molecular relaxation processes may be detected in dynamic mechanical analysis, only relaxation processes associated with dipole reorientations are seen in a dielectric experiment. In the latter experiment an alternating electric field is imposed on the sample between two electrodes causing polarization to occur within the sample. The internal polarization arises from the molecular orientation of dipoles within the sample. For a viscoelastic sample, the magnitude of this polarization (as measured by the dielectric constant) will be temperature and time dependent. Figure 4.4b illustrates the experimental principles involved in a dielectric experiment. One notes that as an ac voltage is applied to the sample, the internal charge displacement (polarization) Q, is followed as a current dQ/dt which will lag the applied voltage by an angle δ. The dielectric technique was well suited for polysulfone whose storage part of the dielectric permittivity was measured to be 2.7 at room temperature.

In practice the tangent of δ is usually monitored, which can be formally defined as the ratio of energy lost (dissipated as heat) per cycle to the energy stored (or recovered) per cycle; in addition,

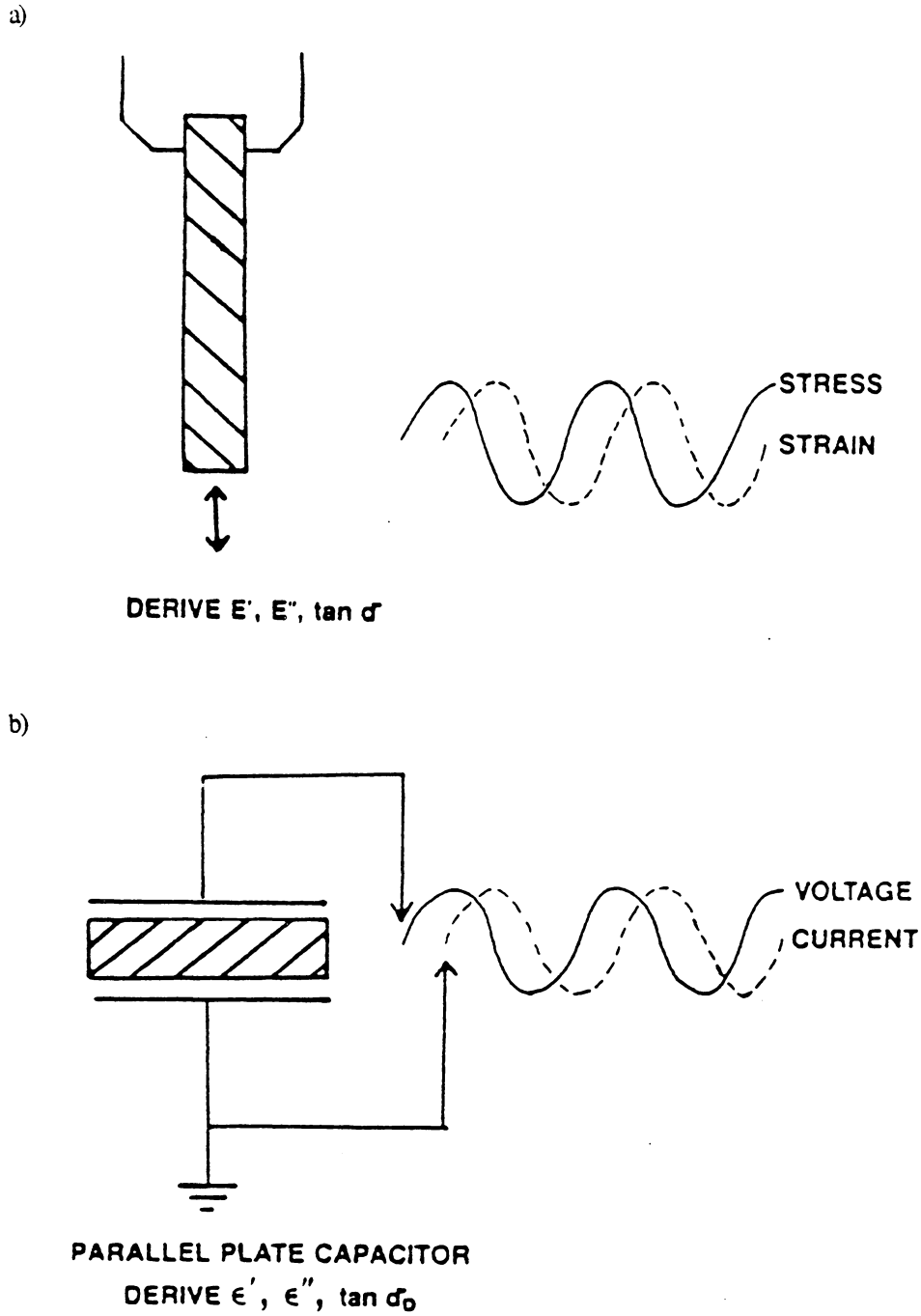

Figure 4.4. Schematic of the operating principles in a). dynamic mechanical experiment, and b). dielectric thermal analysis.

the imaginary and storage part of the complex modulus and dielectric permittivity can be obtained depending on the type of experiment performed.

Tan δ is usually referred to as the dampening or loss factor since it is a direct measure of the material's ability to dissipate energy through molecular motions and changes in material structure. Because of this, dynamic mechanical and dielectric techniques are considered forms of relaxation spectroscopy where both temperature and frequency are the variables which reveal the relaxation mechanisms.

In dynamic mechanical and dielectric thermal analysis temperature scans are done at various preset frequencies. Figure 4.5 illustrates the relaxation in polyethylene terephthalate, as measured by tan δ, for both a dynamic mechanical analysis and a dielectric thermal analysis. One notes that dielectric experiments employ higher frequencies than those used in dynamic mechanical experiments and that as the frequency of the experiment is increased the relaxation spectrum is shifted to higher temperatures.

This frequency dependence of the relaxation spectrum discussed in section 4.5 arises from the fact that the relaxation processes are thermally activated processes (18). Hence, as the imposed frequency is increased, the components of the molecular motions that must couple with the imposed stress field must also increase in frequency, which requires an input of a greater amount of thermal energy (kT).

Another characteristic of tan δ is that it is an extensive property of a material and therefore usually responds in a systematic manner with the volume fraction of the relaxing phase (18). This arises because tan δ is a measure of the energy lost due to the irreversible entropy production originating from diffusional type motions. Figure 4.6 illustrates this for a semi-crystalline poly(vinyl alcohol)-zinc chloride system. One notes that as the volume fraction of amorphous phase is increased (due to the incorporation of $ZnCl_2$ which disrupts the crystallinity) there is a systematic increase in tan δ.

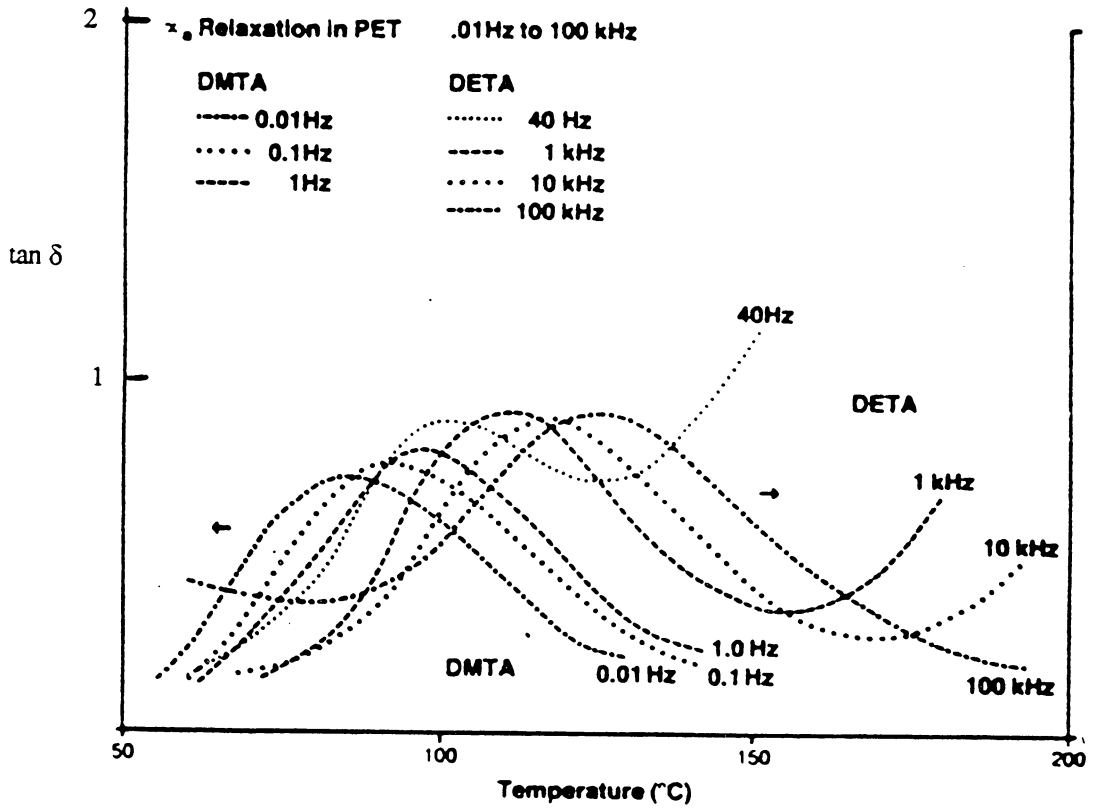

Figure 4.5. Relaxation in poly(ethylene terephthalate) as measured by tan d for both a dynamic mechanical thermal analysis and dielectric thermal analysis at various frequencies (17).

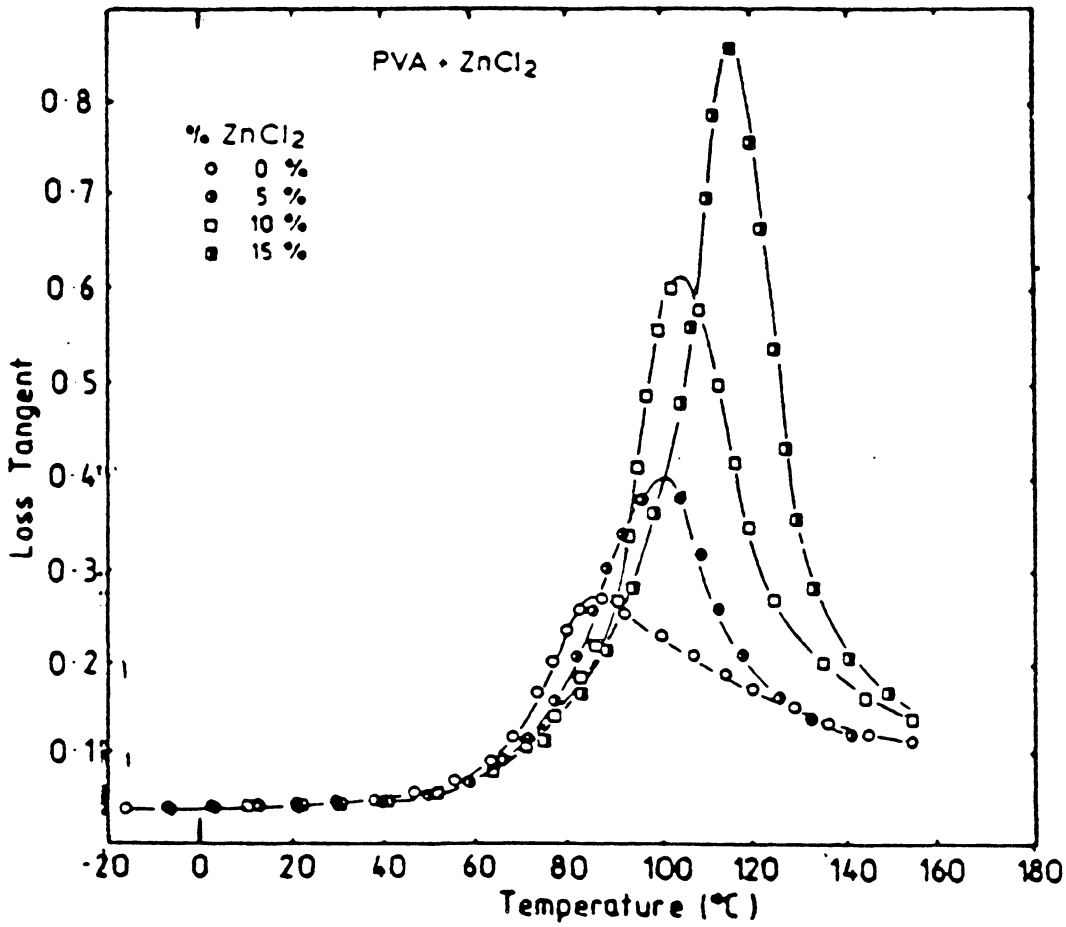

Figure 4.6. Tan δ versus temperature plot for poly(vinyl alcohol) with various amounts of $ZnCl_2$ (18).

4.2.2 Dynamic Experiments in Adhesion

One would anticipate the use of the viscoelastic quantity tan δ in the study of adhesive systems since it is not only a measure of the ability of the system as a whole to dissipate energy but is also sensitive to features which affect the relaxation mechanisms occurring in an adhesive system. An understanding of dissipative process occurring in an adhesive joint can also yield valuable information that could be correlated to bond durability and strength.

Lap shear bonded metal joints of several thermoset and thermoplastic adhesives have been studied by members of our laboratories (19). Results indicated broader relaxation dispersions occurring at higher temperatures and much lower damping values (tan δ) for the bonded systems as compared to the neat films of the adhesive. The adhesive film thicknesses in these studies were greater than 300 μm which resulted in small surface area of substrate to volume of polymer ratios; therefore, with respect to the relaxation behavior of the bonded assemblies, no conclusions could be made as to the role of the interphase region.

A more recent study, by Chua, of glass fiber reinforced polysester systems, correlated the quantity tan δ at the T_g of the composite (tan δ_{Tg}) with the interfacial shear strength (τ_{12}) of the fiber reinforced polyester (20). Chua found an inverse relation between the interfacial shear strength and tan δ_{Tg}, with lower values of tan δ_{Tg} associated with higher interfacial adhesion. Figure 4.7 shows the inverse relation between τ_{12} and tan δ_{Tg}. This study demonstrated how a direct assessment of the quality of adhesion could be attained using the linear viscoelastic quantity tan δ. Hence, the use of dynamic experiments can be a powerful technique for the study of composites and adhesive joints.

With the caution that sample history can affect the linear viscoelastic properties of adhesive joints and composites, it is evident from the above review that the viscoelastic response of these systems can be altered due to adhesion mechanism at the interface. The effect of adhesion

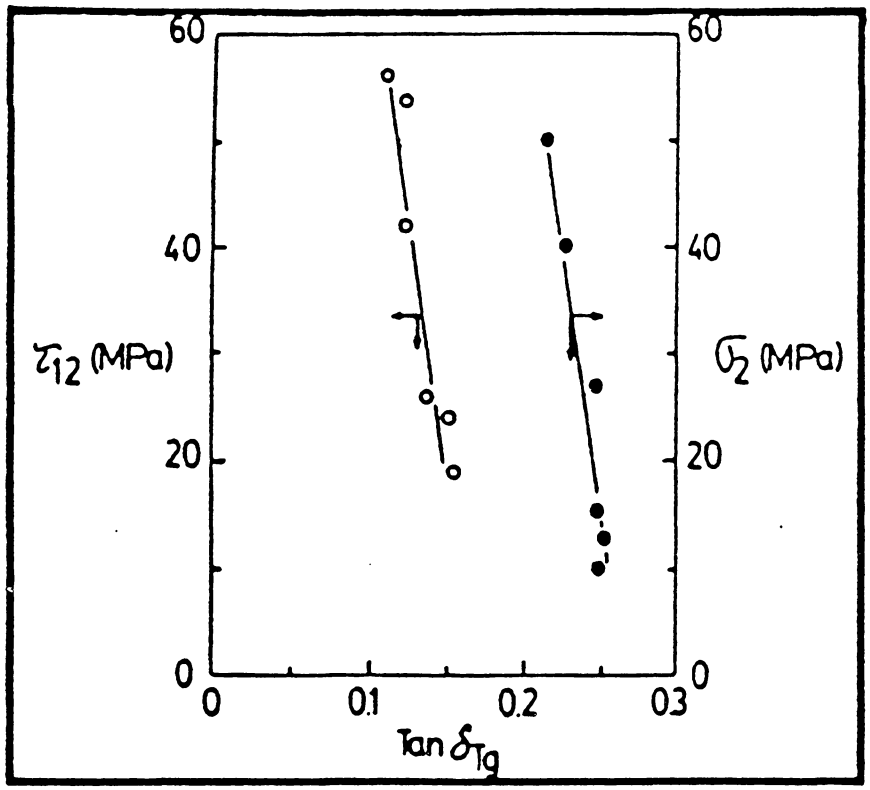

Figure 4.7. Relationship between interfacial shear strength (τ) and tan δ at the T_g (20).

mechanisms on the viscoelastic properties of an adhesive near the interphase must be understood if one is to attain a comprehensive understanding of the factors that are crucial to good adhesion.

4.3 Experimental

4.3.1 Sample Preparation

4.3.1.1 Preparation of Neat Polysulfone Films

Udel P-1700 polysulfone (PSF) was used as the thermoplastic adhesive resin. The number average molecular weight of the polysulfone was 31,000 g/mole, with a polydispersity of 2.5, which was calculated by the method of universal calibration using a Waters 150C GPC with an online Viscotek differential viscosity detector. A neat film of approximately 260 μm was prepared by compression molding at 290 ^{o}C and subsequent annealing at 220 ^{o}C for one hour in order to eliminate internal stresses due to pressing. This neat film was used in both the dynamic mechanical and dielectric analysis.

4.3.1.2 Preparation of Polysulfone Coatings

4.3.1.2.1 Substrate Preparation

The coating substrate was an aluminum foil from ALCOA, which was pretreated by vapor degreasing in one case and by phosphoric acid anodization (PAA) in another. The vapor degreasing was done with 1,1,1 trichloroethane for 30 minutes. The PAA procedure was ASTM D 3933-80 which consisted of anodization in a 10% phosphoric acid solution for 20 minutes with a current density of 6.5 mA/cm^2 at room temperature. The apparatus used for the anodization was a potentiostat/galvanostat (Model 173 E6&6/Princeton Applied Research), and an electrometer (Model 178 E6&6/Princeton Applied Research) to provide constant current for the anodization.

4.3.1.2.2 Coating Preparation

Thin PSF coatings were prepared by spin coating from solutions in chloroform. Variable thicknesses were obtained by varying both the solution concentration and spin coater speed. The spin coater was a photoresist spinner (Model 1-EC101D-R485/Headway Research Inc.). Samples

were annealed for one hour at 220 ^{o}C prior to the experiment and immediately analyzed in order to avoid results characteristic of the sample preparation.

4.3.2 Characterization of Coating Thicknesses

4.3.2.1 Ellipsometry

Ellipsometry was used to indirectly determine the film thicknesses of the polysulfone coatings used in the dynamic mechanical analysis. The apparatus used was a Gaertner L116A dual mode automatic ellipsometer equipped with a 1 mW helium-neon laser (632.8 nm) as the incident light source.

A calibration curve of film thickness versus solution concentration was obtained using the highly reflective ferrotype plate as the substrate. This calibration curve is shown in Figure 4.8; the spin coater speed was held at a constant 3000 rpm. In the generation of the calibration curve, maesurements on the ellipsometer were done with an incidence angle of 70 ^{o} and repeated several times. It was assumed that the coating thickness obtained on the ferrotype surface would be characteristic of those obtained the an aluminum surface.

4.3.2.2 Scanning Electron Microscopy (SEM)

Scanning electron microscopy was used to determine the film thickness of the PSF coatings used in the dielectric thermal analysis. The procedure consisted of preparing the coatings as described above upon which the adhering system was immersed in a 5 wt % NaOH solution. After several minutes the aluminum substrate had dissolved leaving the intact PSF film. The resulting PSF films were then fractured in liquid nitrogen, sputter coated with gold using an Edwards sputter coater S150B and viewed using an ISI-SX-40 SEM.

4.3.3 Characterization of Substrate Surface Topography by High Resolution Scanning Electron Microscopy (HSEM)

HSEM pictures were obtained on a Philips EM-420T electron microscope. Thin aluminum samples were used and coated with Pd-Pt about 2 nm thick. Properly deposited this layer does not

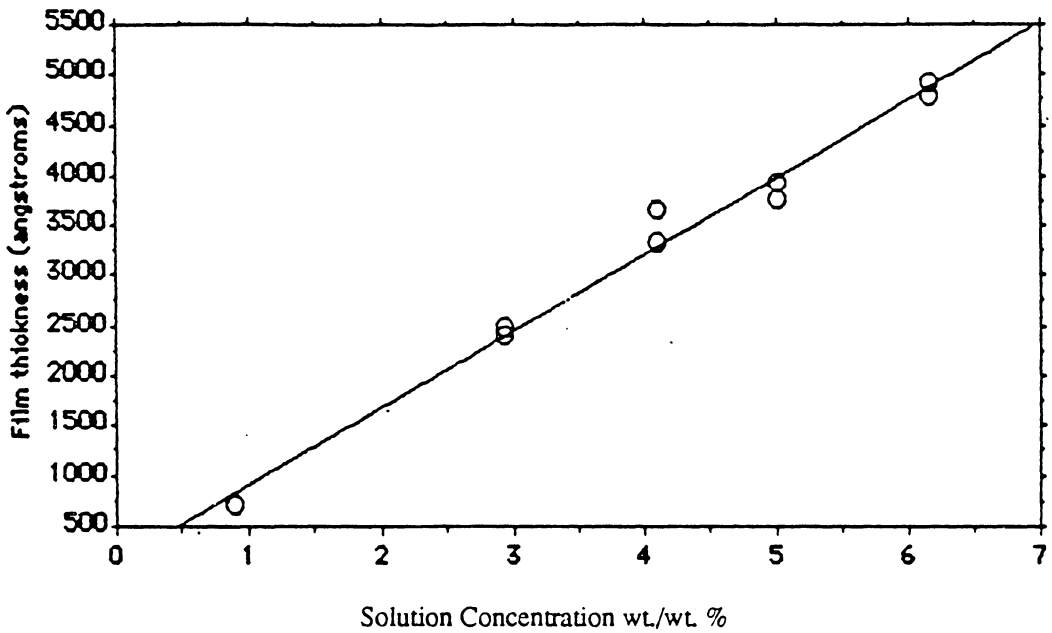

Figure 4.8. Calibration curve as determined by ellipsometry for film thickness versus solution concentration at a spin coater speed of 3000 rpm.

alter the surface topography as detected within the resolution of the microscope.

4.3.4 Characterization of Polysulfone Coatings and Neat Films

4.3.4.1 X-ray Photoelectron Spectroscopy (XPS)

XPS studies were done using a Physical Electronics ESCA 5300 electron spectometer with a magnesium anode (1.254 KeV). All samples were punched as 1.0 cm disks and scanned from 0 to 1100 eV. Major photopeaks were scanned repetitively to obtain the atomic fraction of elements on the sample surface. Both the PSF coatings and neat film surfaces were characterized with XPS. An argon ion beam was used for depth profiling in order to study the chemical composition of the interphase region. Ion sputtering was done with 3 kV energy beam of argon ions having a beam current of 30 μA for successive periods of five minutes. Sputtering on the coatings was continued until both the Al2p and S2p photopeaks were detected. Sputtering was done on the neat film only for comparison.

4.3.4.2 Dynamic Mechanical Thermal Analysis (D.M. T. A.)

The mechanical loss factor, tan δ, was followed as a function of temperature at a series of frequencies with a Polymer Laboraories MKII D. M. T. A.. The operation principles of the D. M. T. A. were given in Chapter 3.

All samples were analyzed in a single cantilever clamping mode with a free unclamped length of 5 μm. The strain amplitude, corresponding to the peak to peak displacement, was 16 μm of the sample, and the heating rate ws 1^{o}C/min for the multifrequency analysis routines.

4.3.4.3 Dielectric Thermal Analysis (D. E. T. A.)

The dielectric loss factor, tan δ was followed as a function of temperature of various frequencies with a Polymer Laboratories D. E. T. A.. The dielectric bridge allows for measurement of tan δ, with a resolution of 0.0001, at various preset frequencies with a variable applied field ranging from 5 mV to 1.275 V. Temperature was measured with a 100 ohm platinum resistance thermometer mounted adjacent to the bottom electrode. In this study, all samples were analyzed

with an applied field of 0.1 volt and scanned at 5 deg/min from 160 to 250 °C with a multifrequency (0.1-100 kHz) analysis routine.

PL D. E. T. A. Operating Principles (21)

The Polymer Laboratories D. E. T. A. utilizes the transformer ratio arm bridge as its basis for measuring dielectric relaxation in polymers. The advantage of bridge methods is the broad range of frequencies that are attainable; the PL-DETA has a range from 0.02-100 kHz.

The PL-DETA measures the voltage across the sample cell and a standard resistor carrying the same current as the cell specimen. Normally eight voltage measurements are made for each parameter calculated; thus, each single measurement (or data point) represents an averaged value over eight measurements. A phase sensitive detector is used to obtain the phase relationships between the reference signals and measured signals. hence, the capacitance and tan δ are calculated directly by a microprocessor from the voltage measurements and the predetermined frequency.

4.4 Results and Discussion

4.4.1 High Resolution Scanning Electron Microscopy

The degreased aluminum surface and the PAA aluminum surface was studied with HSEM in order to determine the surface topography. The resulting HSEM micrograph for the degreased aluminum surface shown in Figure 4.9a, at 25,000x, revealed that pretreatment by just vapor degreasing resulted in a smooth surface with a few machine rolling marks. The phosphoric acid anodization resulted in a surface topography shown in Figure 4.9b. The micrograph at 50,000x shows the fully porous oxide layer with a pore diameter of approximately 100 nm.

4.4.2 XPS

XPS was used to study the interphase chemical environment of the PSF coatings both on the smooth aluminum (sm-Al) surface and the porous aluminum (p-Al) surface. Knowledge of the interphase chemistry was required since the objective of this work was to examine the effect of substrate topography and not chemistry on the relaxation properties of adhering systems. The PSF

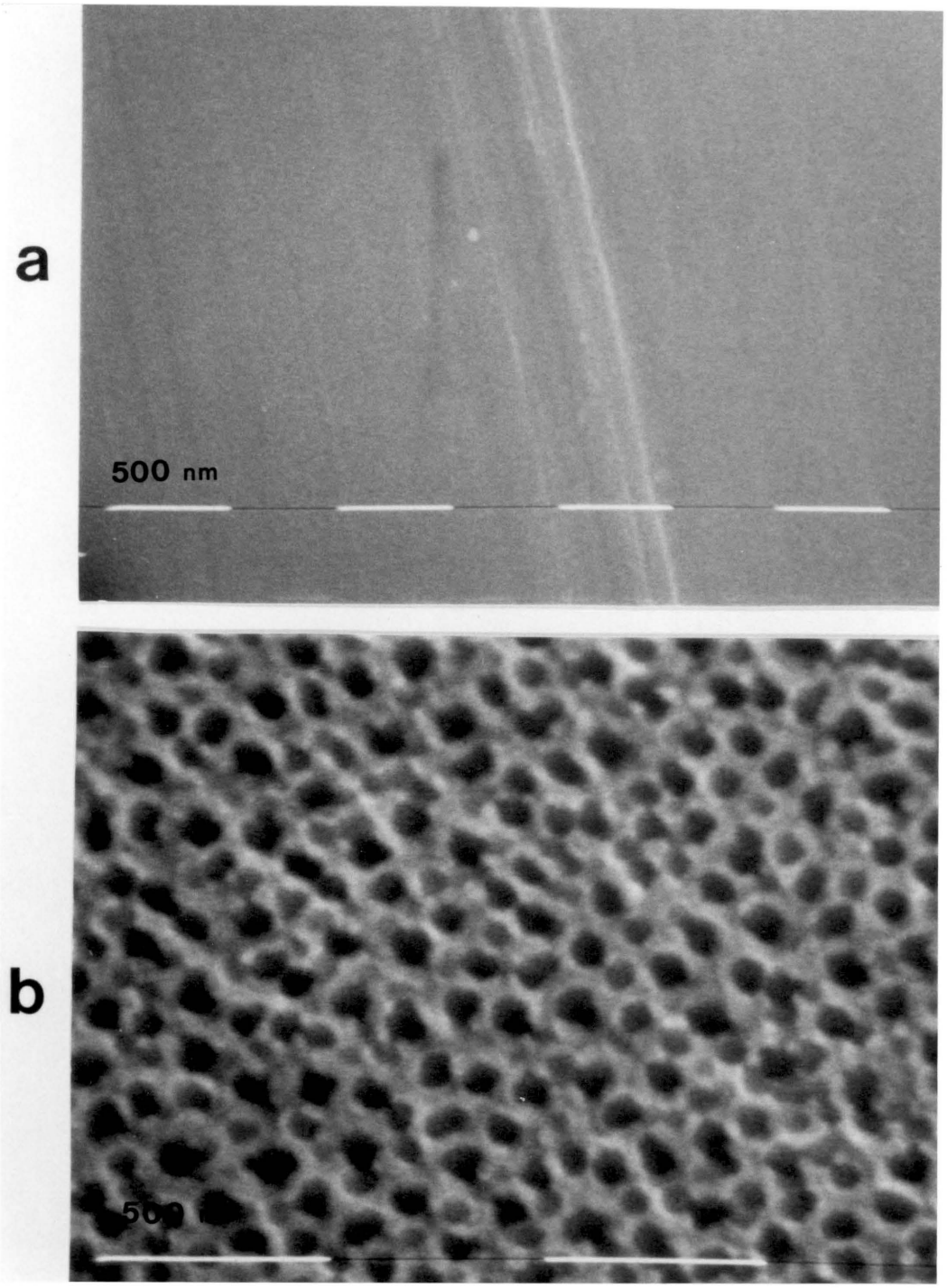

Figure 4.9. HSEM micrographs of pretreated aluminum surfaces : a). A vapor degrease pretrement at 25,000 x, and b). Phosphoric acid anodization at 50,000 x.

coatings (<100 Å) were analyzed both before and after an argon ion sputter. This allowed for a comparison to be made between the bulk chemistry and interphase chemistry. In addition, a neat PSF film was analyzed both before and after sputtering and was used as the reference sample.

The results are shown in Table 4.1 and in Figures 4.10-4.12 where the narrow scan spectra for the oxygen 1s and sulfur 2p photopeaks are shown for all the samples: the neat film, the PSF coating on the sm-Al surface and the PSF coating on the p-Al surface.

Referring to Figure 4.10 and Table 4.1 for the neat film, one notes that before sputtering the oxygen 1s (O 1s) photopeak is a doublet with a peak at 533.2 eV corresponding to the S=O oxygen and the peak at 531.9 eV corresponding to the C_6H_4--O-- oxygen. In addition, the sulfur 2p (S 2p) photopeak is at 167.8 eV. After argon ion sputtering the neat film, the O 1s photopeak becomes a single peak and the S 2p peak is shifter toward a lower binding energy at 163.8 eV. Two explanations exist for the shifting of the sulfur 2p peak: (1) a surface charging effect induced by the sputtering process or (2) alteration of the sulfur to a different chemical state (probably a reduced state) caused by the sputtering. The first explanation seems less likely since surface charging should lead to a shifting of all peaks in the spectrum of the same extent; the carbon 1s and oxygen 1s photopeaks did not shift after sputtering (2). The second explanation would seem more plausible. This is supported by the observation that the atomic fraction of O 1s decreased from 0.18 to 0.04 (Table 4.1) with the argon ion sputter, keeping with the thought that a chemical reduction of the sulfur had occurred.

In Figure 4.11 and Table 4.1, the results for the PSF coating on the sm-Al surface are shown. Before argon ion sputtering the XPS results are similar to those of the neat PSF film before sputtering. Hence, the presence of the aluminum substrate did not alter the chemical state of any of the elements studied. This leads to the conclusion that any chemical "effects" (strong intermolecular interactions or reactions) at the interphase could be ignored. After argon ion sputtering, the XPS

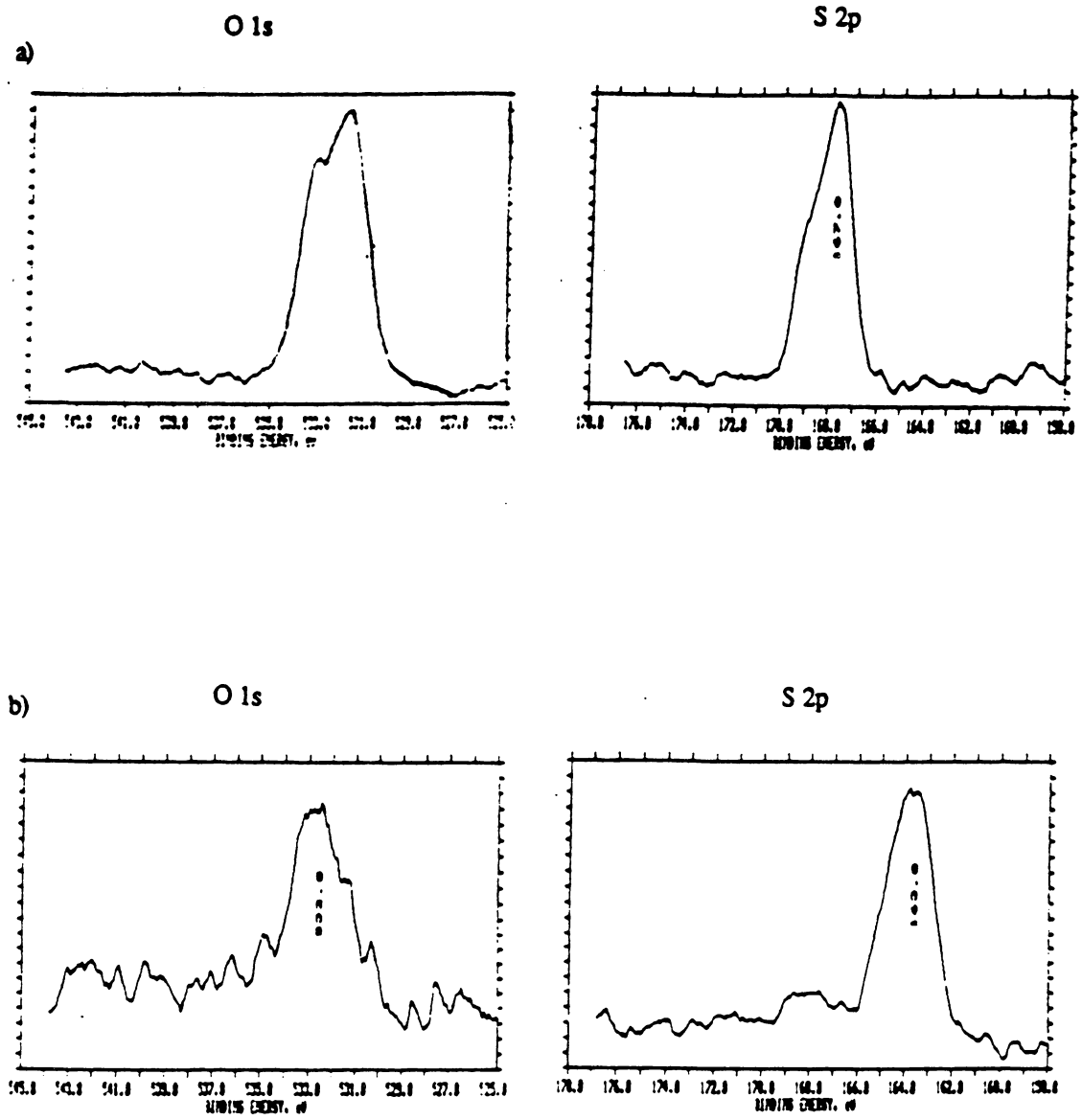

Figure 4.10. **Neat PSF film** -narrow scan XPS specrum for O 1s and S 2p photopeaks : a). before argon ion sputter, and b). after argon ion sputter.

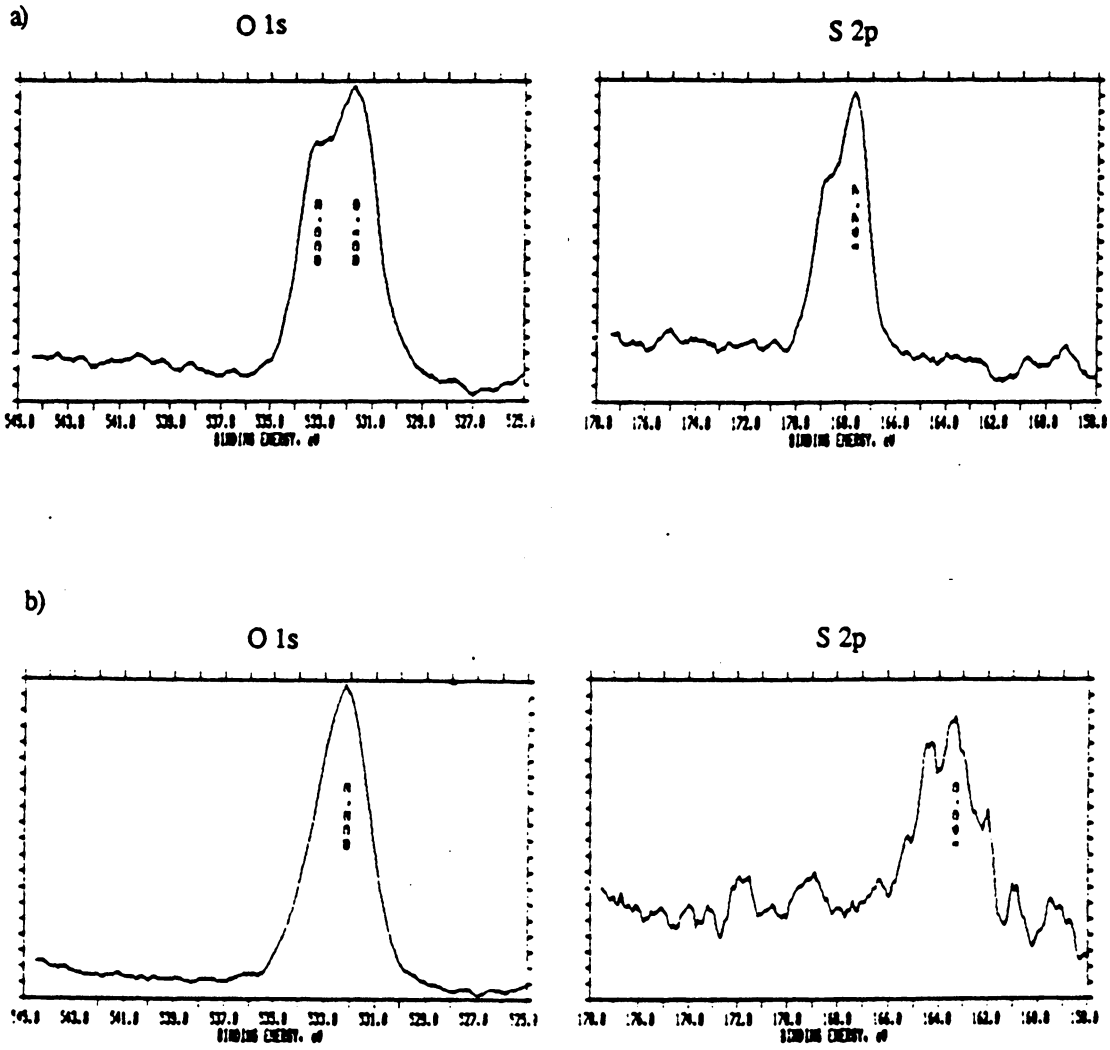

Figure 4.11. **PSF coating on sm-Al** -narrow scan XPS specrum for O 1s and S 2p photopeaks : a). before argon ion sputter, and b). after argon ion sputter.

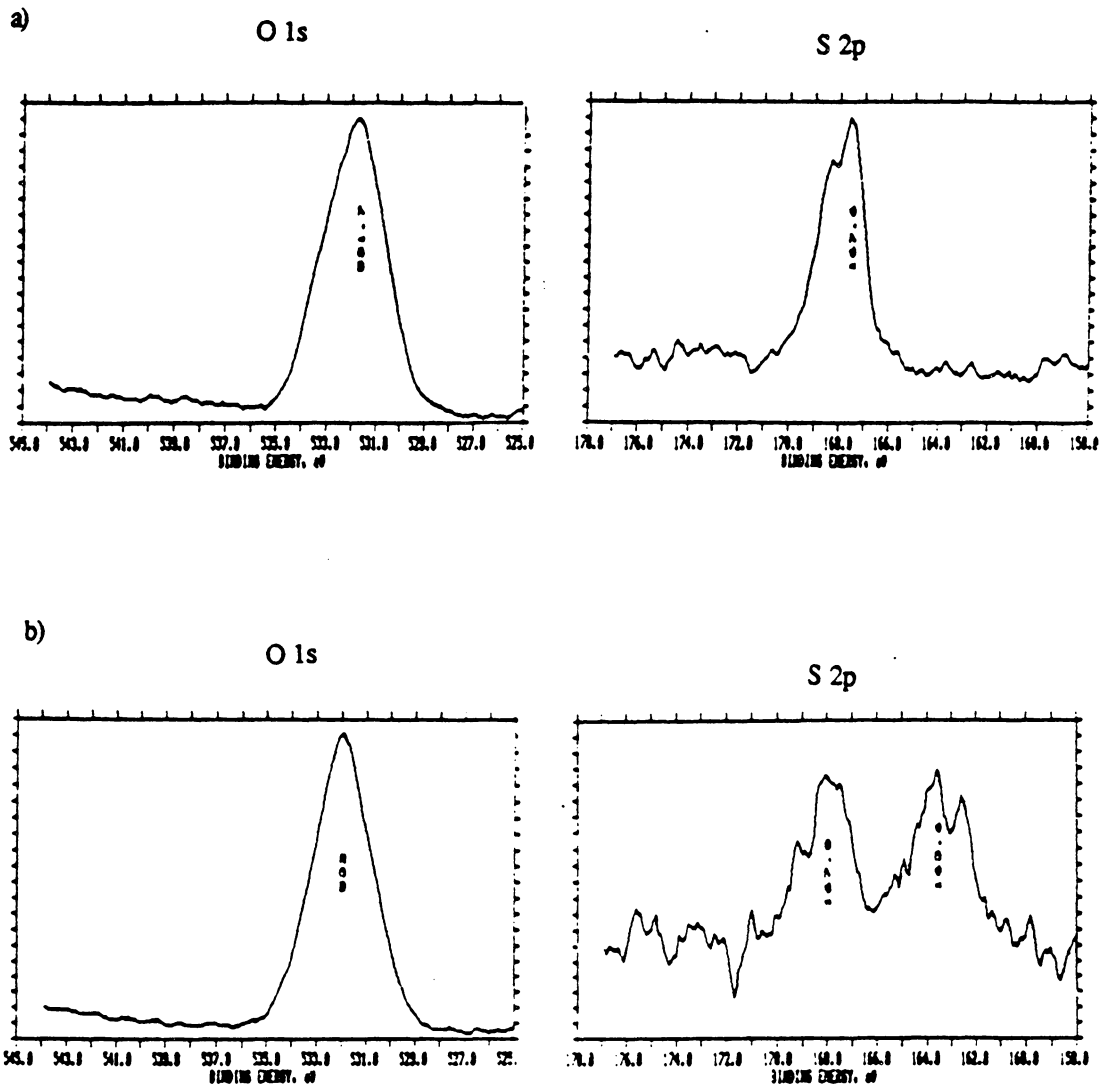

Figure 4.12. **PSF coating on PAA-Al** -narrow scan XPS specrum for O 1s and S 2p photopeaks : a). before argon ion sputter, and b). after argon ion sputter.

Table 4.1. XPS results for PSF film and coatings - atomic fractions and binding energies.

	PSF film			
	Before Ar ion sputter		After Ar ion sputter	
Photopeak	B.E. (eV)	A.F.	B.E. (eV)	A.F.
C 1s	284.6	0.79	284.6	0.94
O 1s	533.2	0.18	532.5	0.04
	531.9			
S 2p	167.8	0.025	163.8	0.02
	PSF coating on degreased Al.			
C 1s	284.6	0.72	284.6	0.52
O 1s	533.2	0.21	532.2	0.27
	531.8			
Al 2p	74.4	0.04	75.4	0.19
S 2p	167.7	0.028	163.3	0.013
	PSF coating on PAA Al.			
C 1s	284.6	0.56	284.6	0.40
O 1s	531.7	0.31	532.0	0.40
Al 2p	74.5	0.11	74.7	0.18
S 2p	167.6	0.02	167.9	0.01
			163.6	
P 2p	134.6	0.01	134.9	0.01

results of the PSF film on the sm-Al surface is again similar to that of the neat film after sputtering; hence, the aluminum substrate did not alter the sputtering effects observed for the S 2p photopeak.

The XPS results for the PSF film on the p-Al surface are shown in Figure 4.12 and Table 4.1. From Table 4.1 one notes the presence of a phosphorous (P) 2p photopeak at 134.6 eV which is due to the phosphoric acid used in the pretreatment. Aside from the P 2p photopeak, the results are similar to the results for the PSF film on the sm-Al surface. After argon ion sputtering, the XPS results for the film on the p-Al surface are similar to those for the film on the sm-Al surface in all photopeaks except the sulfur 2p photopeak where there exists two separate peaks, one at 167.9 and another at 163.6 eV. While the peak at 163.6 eV is due to the sputtering process (as before with the neat film and coating on the sm-Al surface), the new peak at 167.9 eV was thought to be due polysulfone within the oxide pores which was not affected by the argon ion beam sputter; this was confirmed in latter experiments (SEM) to be the case.

4.4.3 Dynamic Mechanical Analysis of PSF Coatings and Neat Films

Initial interest in examining the mechanical relaxation properties of adhering systems drew from results of R. E. Wetton at Polymer Laboratories (22). Wetton's results on poly(vinyl chloride) (PVC) coatings demonstrated the sensitivity of the D. M. T. A. where the limit of detection of very thin films was found to be between 100 and 500 Å. The sensitivity of the D. M. T. A. was confirmed in our laboratories as shown in Figure 4.13a where a 1500 Å coating of PVC on a 0.05 mm steel shim was easily detected. The steel alone, of course, produced a horizontal straight line in this test. Work on the PVC coatings also demonstrated that a difference existed between the response of the coatings and the neat material. This is shown in Figure 4.13b where the T_g is 9 ^{o} C higher and also broader for the 1500 Å coating than the neat PVC film. These initial interests proved to be exciting since it seemed possible to truly probe interphase properties, but when efforts turned to the polysulfone-aluminum systems, limitations to the limit of detection were found. These limitations were found to be a function of the substrate used, since the substrate had

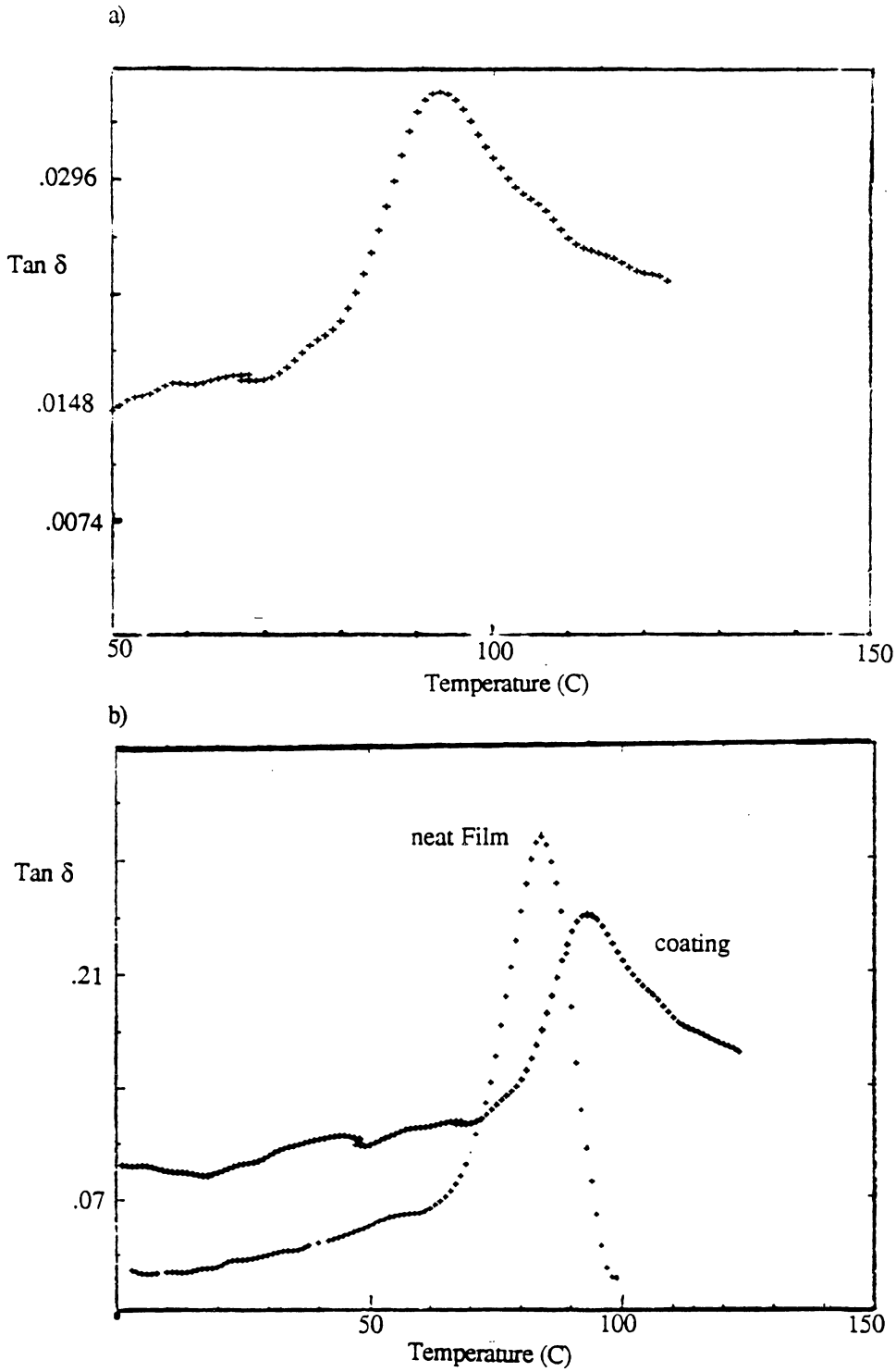

Figure 4.13. Dynamic mechanical analysis of PVC: a). 1500 Å coating, and b). 1500 Å coating and neat film.

to fulfill two criteria: 1) low compliance with respect to the forces exerted by the D.M. T. A. and 2) moderate stiffness (dictated by the thickness of the substrate/shim) values such that the D.M.T.A. vibrator drive could strain the coating system, while maintaining an adequate volume fraction of polymer on the coated system. Aluminum proved to be a problem since thin shims (0.1 mm to 0.3 mm) were too ductile and were capable of permanent deformation by the D. M. T. A. forces. This led to a lower signal to noise as shown in Figures 4.14a and 4.14b where the top (4.14a) graph is the response of 2500 Å PSF coating on a 0.2 mm aluminum shim. Figure 4.14b is a PSF film of the same thickness (2500 Å) but cast onto 0.12 mm titanium foil, higher damping values and less noise was noted for this sample. For both cases, the nominal peak to peak displacement was 16 microns -- chosen to avoid effects of non-linear behavior.

In order to prevent permanent deformation of the aluminum, thicker foils were chosen along with thicker coatings. The best compromise was a 0.32 mm aluminum foil coated with a 3500 Å PSF film analyzed at a peak to peak displacement of 16 microns. The results for the dynamic mechanical analysis of the coatings on the sm-Al and p-Al surface are shown in Figures 4.15 and 4.16 respectively at various frequencies. The detection of these 3500 Å films was good as can be seen from the figures. In Figure 4.17, a comparison is made between the neat film, 4.17a, and the PSF film on the p-Al surface, 4.17b. The PSF film on the p-Al surface has a broader dispersion shifted to higher temperatures. This was also true of the film on the sm-Al surface. The higher T_g values for the coatings could be due to an interphase contribution, where if the polymer chains are reduced in mobility or becoming anisotropically conformed, entropy would be reduced and the T_g raised. Differences in relaxation behavior between the coatings were not significant, except for the scans done at low frequencies (less than 0.33 Hz). In Figure 4.18, the tan δ versus temperature curves for both the film on the sm-Al surface and p-Al surface are compared, which are the results of five overlays. While there is a slight shift in the dispersion to higher temperatures for the film on the p-Al surface, there is no other significant difference between the relaxation behavior of the films.

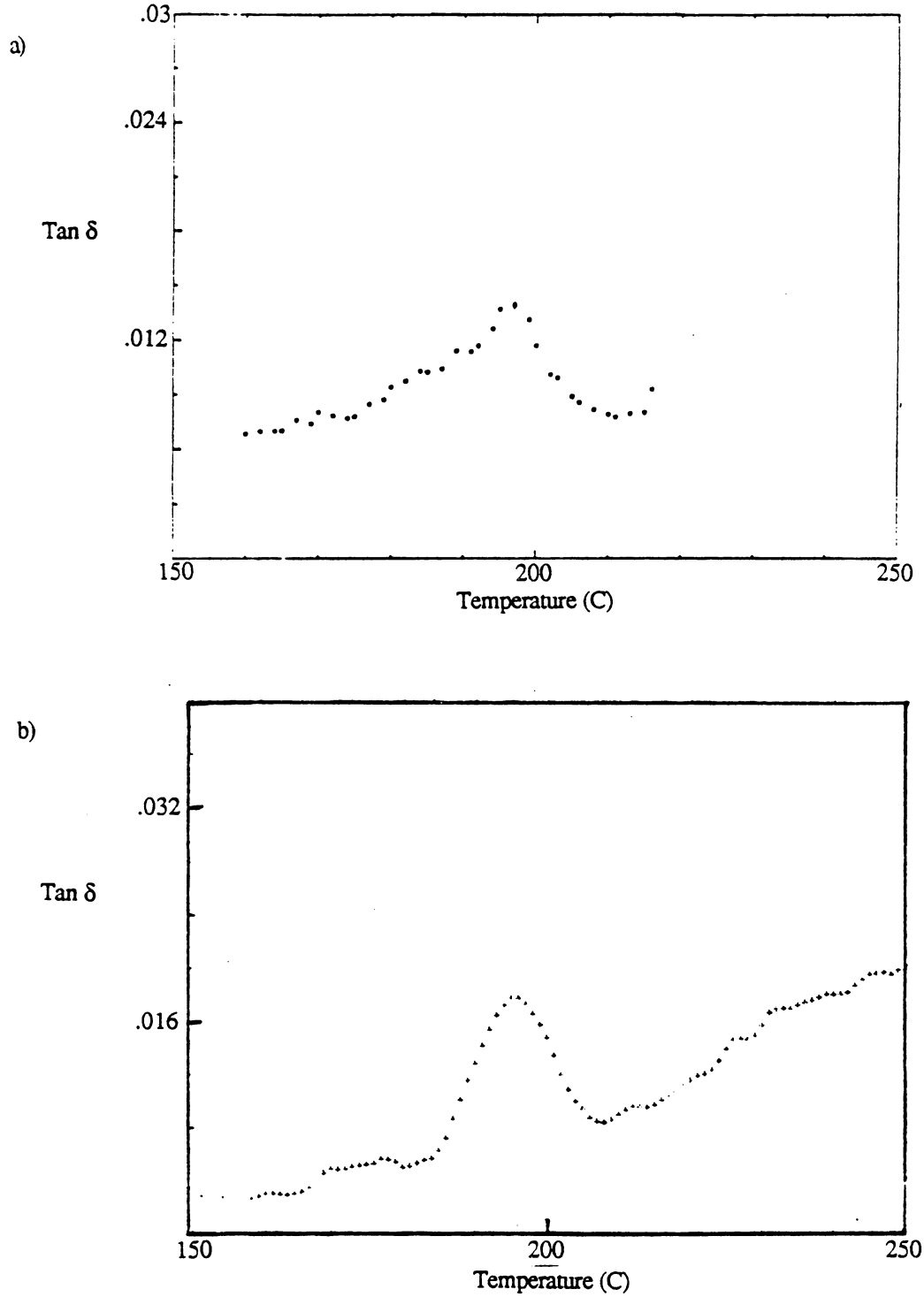

Figure 4.14. Dynamic mechanical analysis of 2500 Å PSF coatings : a). on an aluminum foil substrate, and b). Titanium foil substrate.

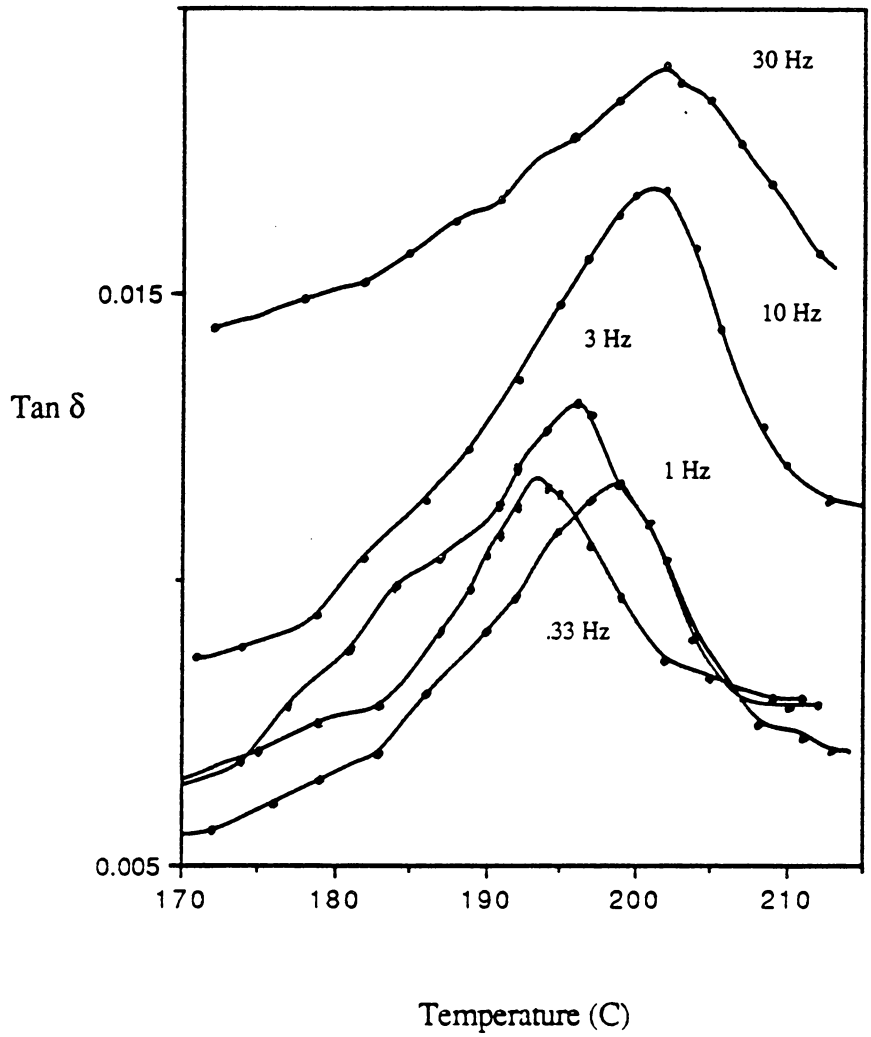

Figure 4.15. Multifrequency-dynamic mechanical analysis of 3500 Å PSF coating on a smooth aluminum surface

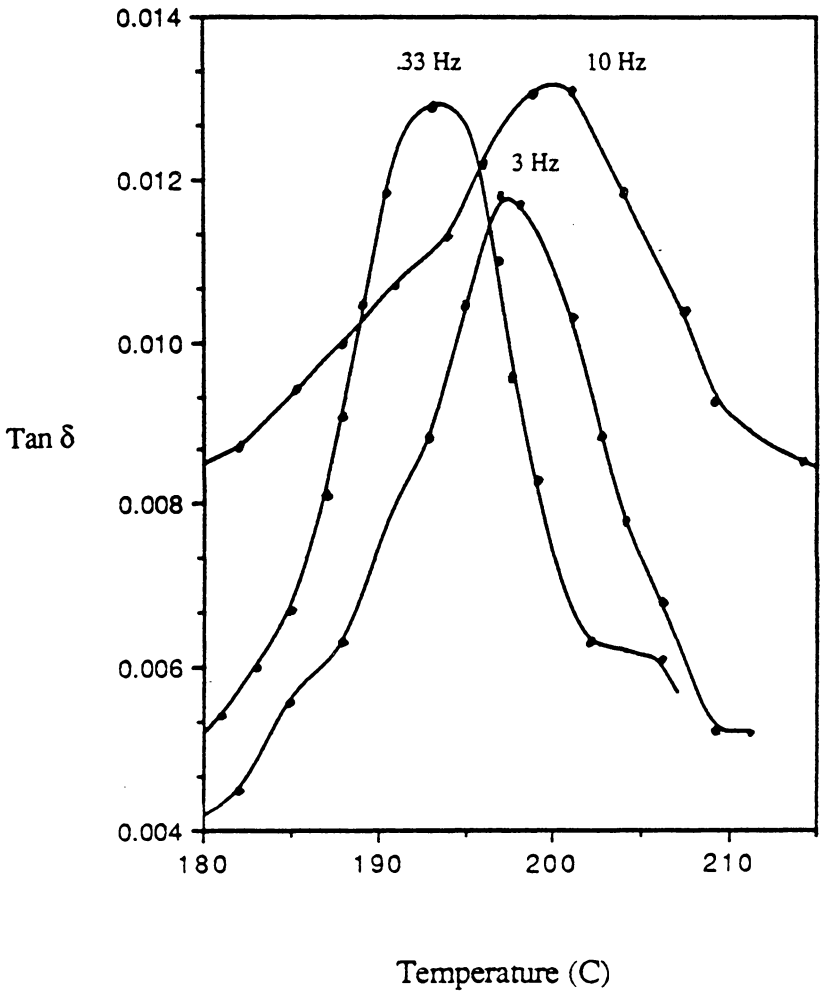

Figure 4.16. Multifreqency-dynamic mechanical analysis of 3500 Å PSF coating on a PAA aluminum surface

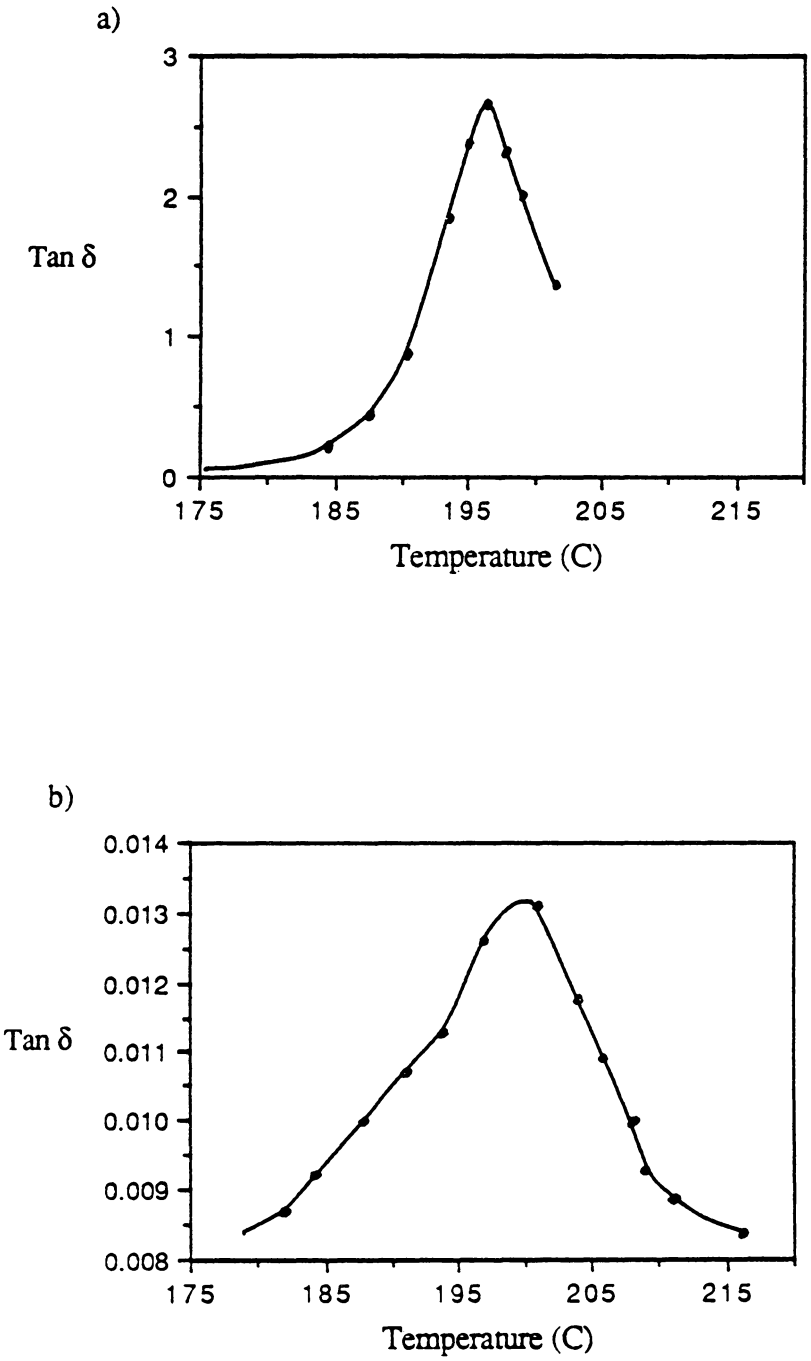

Figure 4.17. Dynamic mechanical analysis at 10 Hz of PSF : a). neat PSF film, and b). 3500 Å coating on a PAA aluminum surface.

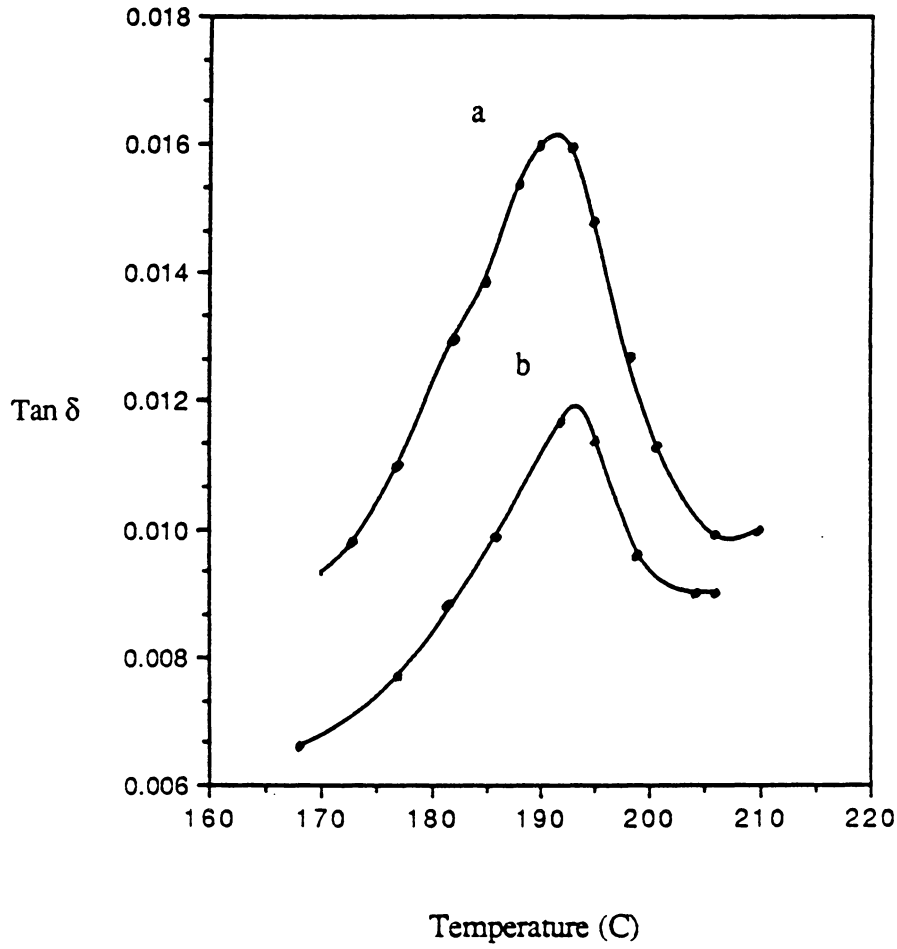

Figure 4.18. Dynamic mechanical analysis at .1 Hz of PSF : a). on smooth aluminum surface, and b). on a porous aluminum surface.

In Table 4.2 the glass transition temperatures are given for all films. All reported T_g values were reproducible within ± 0.5 °C and were obtained from the temperature at which tan δ was a maximum. The differences in the T_g's between the coatings at lower frequencies can be understood if one considers the kinetics of the relaxation process.

When viscoelastic properties (ex. tan δ) are presented on a temperature plane, the dispersions are seen to shift with frequency (as was shown in Figure 4.5). It is common to represent this frequency dependence in terms of an Arrhenius expression, where the activation enthalpy (ΔH^*) for the relaxation mechanism is given as

$$\Delta H^* = R\ln(f_2/f_1) / (1/T_1 - 1/T_2) \qquad [4\text{-}1]$$

where T_1 and T_2 are the tan δ_{max} temperatures at frequencies f_1 and f_2 respectively (18). Hence, the frequency dependence of T_g is defined in terms of the temperature independent value of ΔH^*. Moreover, ΔH^* is an average activation energy for the entire relaxation process which arises from the consideration of the intra- and inter- molecular fields of force governing each relaxaton mechanism. A discussion concerning activation energies and relaxation times is presented in Section 4.5 of the Appendix.

Activation energies for the three films studied were calculated from the above equation. In Figure 4.19 the Arrhenius plots of log f versus $1/T_g$ for the three films are shown; the plots are linear as expected based on the above equation. From the slopes of these lines the average activation energy was calculated for all the films. Table 4.3 gives the ΔH^* values with the least squares errors. Two points can be made from the table: 1) The coatings have higher activation energies than that of the neat film and 2) the film on the p-Al surface has a higher activation energy than the film on the sm-Al surface.

Considering the first point, that higher activation energies were obtained for the coatings, this can be explained if one accepts that interphase properties are still being sensed at a film thickness of 3500 Å. Hence, the activation energies calculated for the coatings can be thought to arise from an

Table 4.2. Glass transition temperatures for PSF neat film and coatings (0.35 μm) at various frequencies as determined by dynamic mechanical analysis.

Frequecy (Hz)	On Smooth - Al	On PAA - Al	Neat PSF
0.1	190.5	193.0	-
0.33	193.0	194.0	188.0
1.0	195.0	195.0	-
3.0	197.0	197.0	191.0
10.0	200.0	199.5	196.5
30.0	202.0	-	198.5

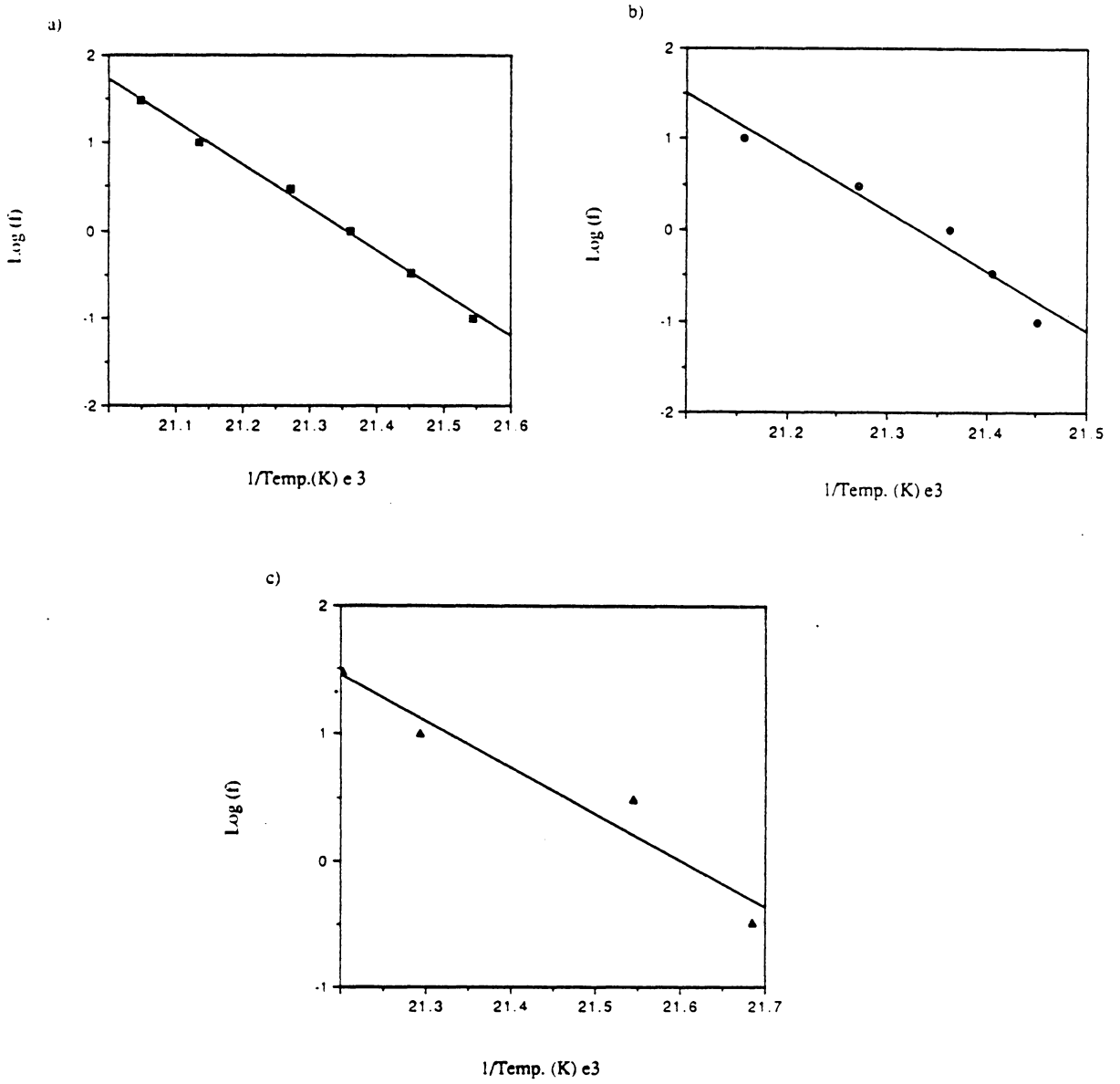

Figure 4.19. Arrhenius plots, as determined from the dynamic mechanical analysis, for : a). PSF on smooth aluminum surface, b). PSF on porous aluminum surface, and c). neat PSF film.

Table 4.3. Arrhenius activation energies for PSF of various film states.

Film State	ΔH* kJ/mol
Smooth - Al	933 ± 27
Porous - Al	1250 ± 150
Neat film	699 ± 160

interphase contribution and a bulk contribution. This is analogous to methodology used by Theocaris et al. in Section 4.1.3 in explaining the T_g variation in particle composites. Furthermore, if interphase properties are influencing the activation energy of the coatings, one would expect the average activation energy within the interphase region to be higher than that within the bulk region. This situation would be expected to arise because within the interphase region, enthalpies of adsorption contribute to the thermally activated mechanisms. These energies of adsorption can be on the order of 20-200 kJ/mole depending on the mechanism of adsorption (physisorption and/or chemisorption) (23). Several authors have examined the influence of long range forces emanating from a solid phase and found that these force fields can extend into the bulk of the adsorbate. Derjaguin and co-workers have looked at the boundary viscosity of poly(dimethylsiloxane) liquids and found that thin films on a metallic substrate exhibited a viscosity profile where at thicknesses of less than 200 Å, the viscosity was found to be greater than the bulk value by 40% (24). In other studies as reviewed by Bascom, Derjaguin et al. reported anomalous behavior of thin film to occur at distances of 20-10,000 Å (25). Another example is that of lubricatng oils where films several thousand angstroms thick have viscosities ten times that of the bulk (26). Thus, the suspicion that interphase properties are being sensed at 3500 Å film thickness is not mere hypothesis. In addition, if one considers that higher activation energies are associated with longer relaxation times and thus larger scale interactions(see Section 4.5) the results in Table 4.3 are consistent with the findings above of Derjaguin, since longer relaxation times are also associated with higher viscosity values (27). Considering the second point, that the film on the p-Al surface had a higher activation energy than the film on the sm-Al surface, this can be understood by noting that the exposed surface area is greater in the case of p-Al surface; therefore, the extent of the interphase is also greatest with this sample.

4.4.4 Dielectric Thermal Analysis

It was thought that the dielectric relaxation properties of the thin films would be more sensitive to interphase effects than the mechanical relaxation properties. In the dielectric experiment the relaxation of polar groups is important and indeed the interaction of these polar groups with the metal substrate could lead to anomalous behavior of the dielectric relaxation properties at the interphase.

A series of seven samples were investigated by dielectric thermal analysis. These included: 1) A neat film labelled sample A. 2) Three coatings on the sm-Al surface of increasing thickness labelled sample B1, B2 and B3 respectively. 3) Three coatings on the p-Al surface of increasing thickness labelled sample C1, C2 and C3 respectively.

Scanning electron microscopy was used to determined the film thicknesses of the coatings and the morphology of these films on the aluminum surface. This was done, as discussed in the Experimental section, by dissolving away the aluminum substrate and observing the resulting films. Figure 4.20 shows the results from samples B1 (Figure 4.20a) and from sample C1 (Figure 4.20b) at 5000x. Sample B1 is observed to have a film thickness of approximately 0.8 microns. Sample C1 is seen to be comprised of two distinct layers: 1) a 2.2 μm thick whisker layer comprised of individual whisker like structures with diameters of about 100 nm, which are a result of the interpenetration of the PSF into the porous aluminum oxide (this is consistent with the XPS results cited), and 2) an overlayer of about 0.2 μm in thickness which is the PSF residing above the metal oxide. Figure 4.21a and 4.21b shows the additional results obtained for samples B3 and C2 respectively. The interpenetration of PSF into the p-Al surface occurred for all samples studied. Table 4.4 lists the corresponding film thicknesses for all coatings. The thicknesses reported for the films on the p-Al surface are for overlayer only, since all these films had a whisker layer of about the same thickness (2.0-2.2 μm).

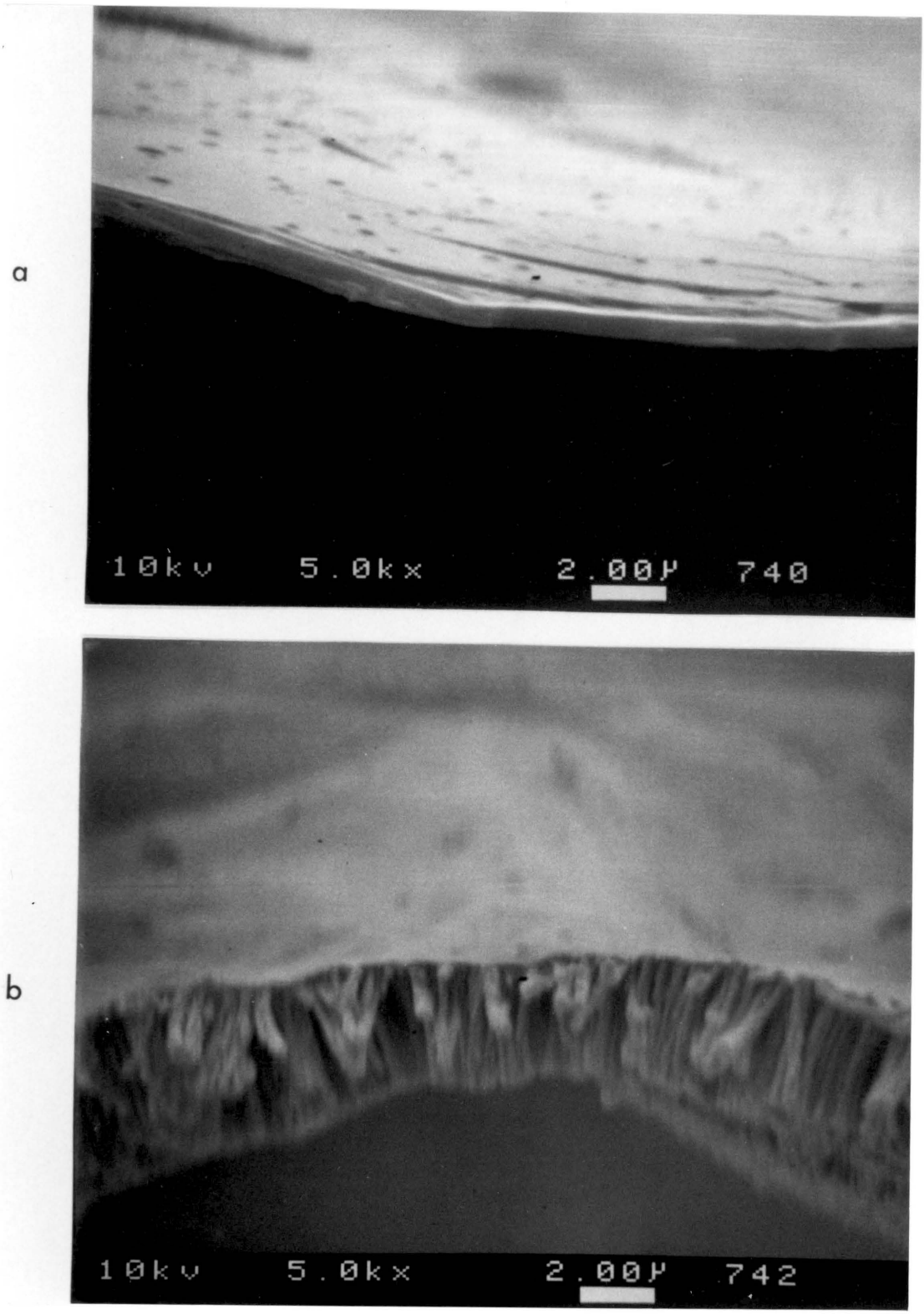

Figure 4.20. SEM of PSF film coatings after removal of aluminum substrate : a). film coated onto a smooth aluminum surface (sample B1), and b). film coated onto porous aluminum surface (sample C1).

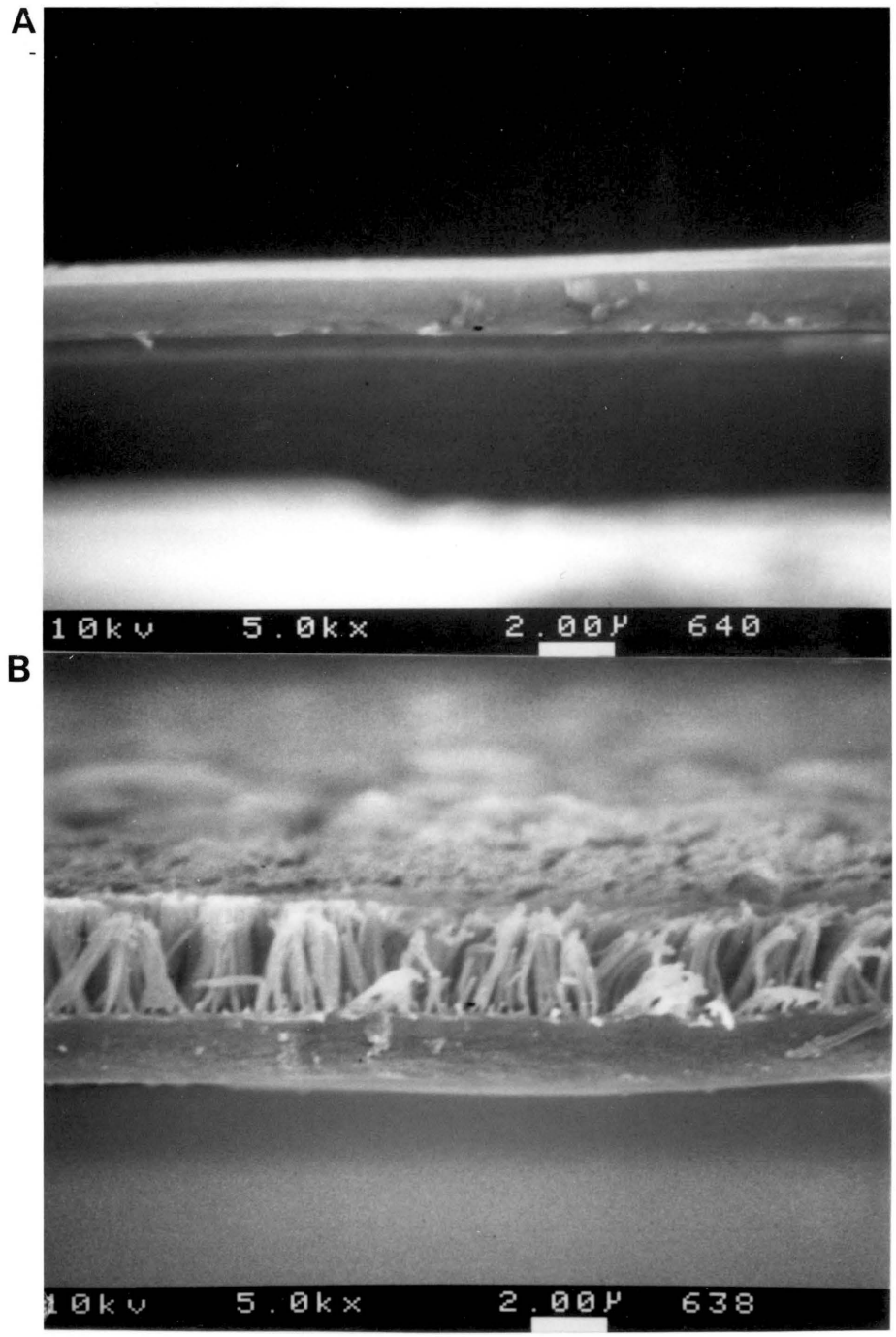

Figure 4.21. SEM of PSF film coatings after removal of aluminum substrate : a). film coated onto a smooth aluminum surface (sample B3), and b). film coated onto porous aluminum surface (sample C2).

Table 4.4. PSF coating thicknesses as determined by SEM for coatings on smooth aluminum surface (samples B1, B2, and B3) and coatings on porous aluminum surface (samples C1, C2, and C3).

Sample	Coating Thickness (μm)
B1	0.8
B2	1.4
B3	1.8
C1	0.2
C2	2.0
C3	5.0

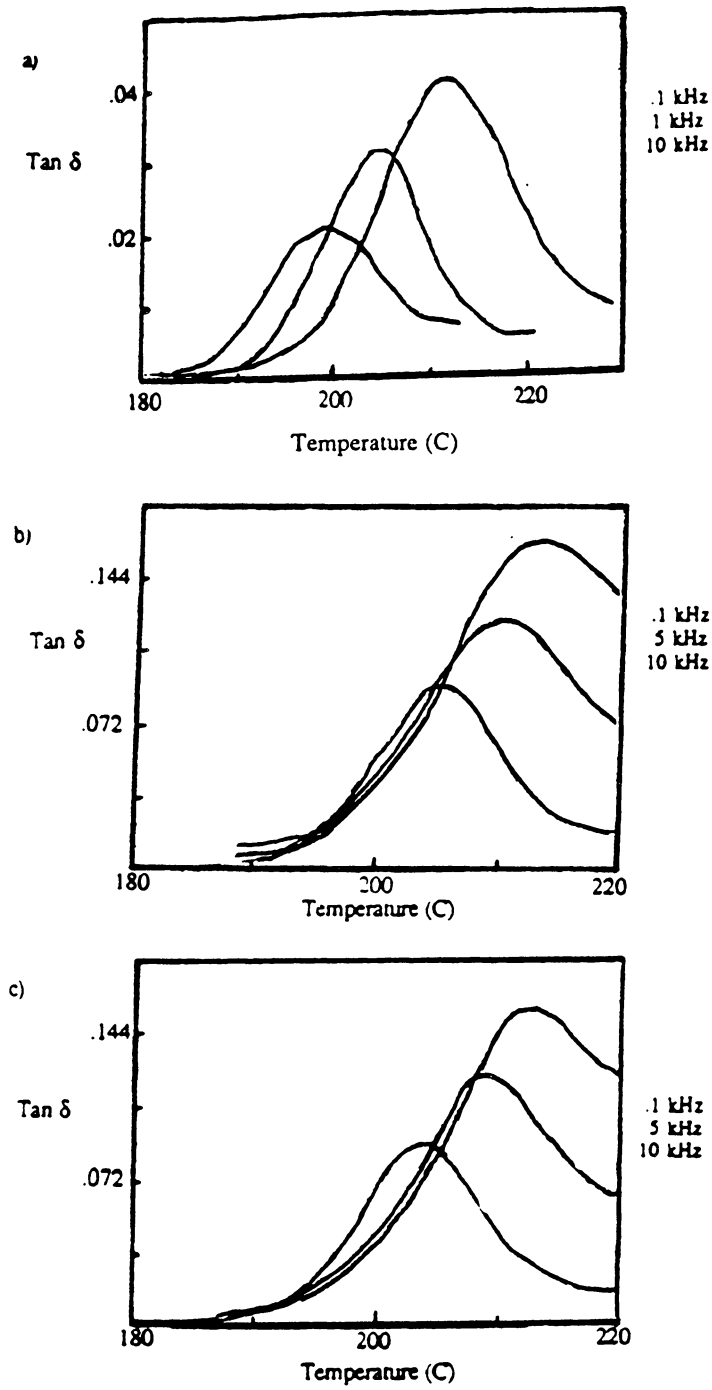

Figure 4.22. Multifrequency-dielectric thermal analysis results for PSF coatings on smooth aluminum substrate of a). 0.8 μm coating, b). 1.4 μm coating, and c). 1.8 μm coating.

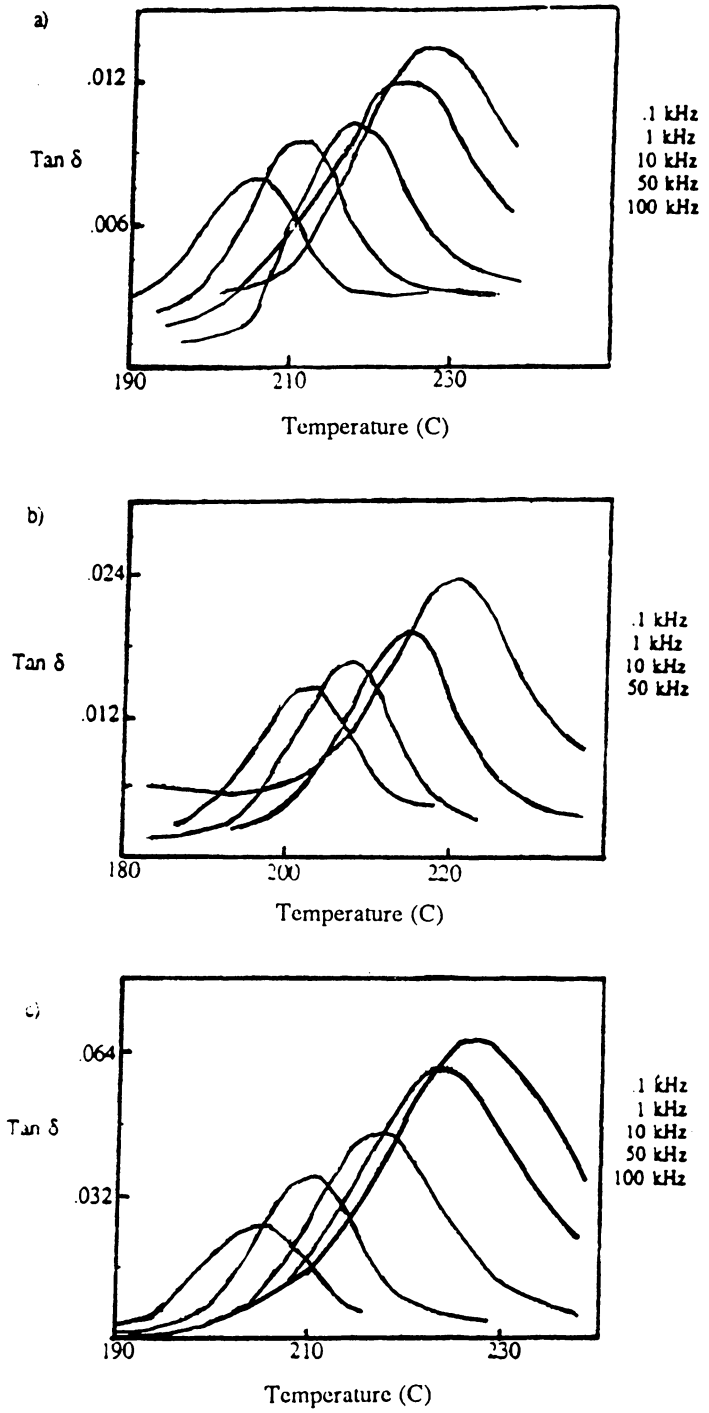

Figure 4.23. Multifrequency-dielectric thermal analysis results for PSF coatings on porous aluminum substrate of a). 0.2 μm coating, b). 2.0 μm coating, and c). 5.0 μm coating.

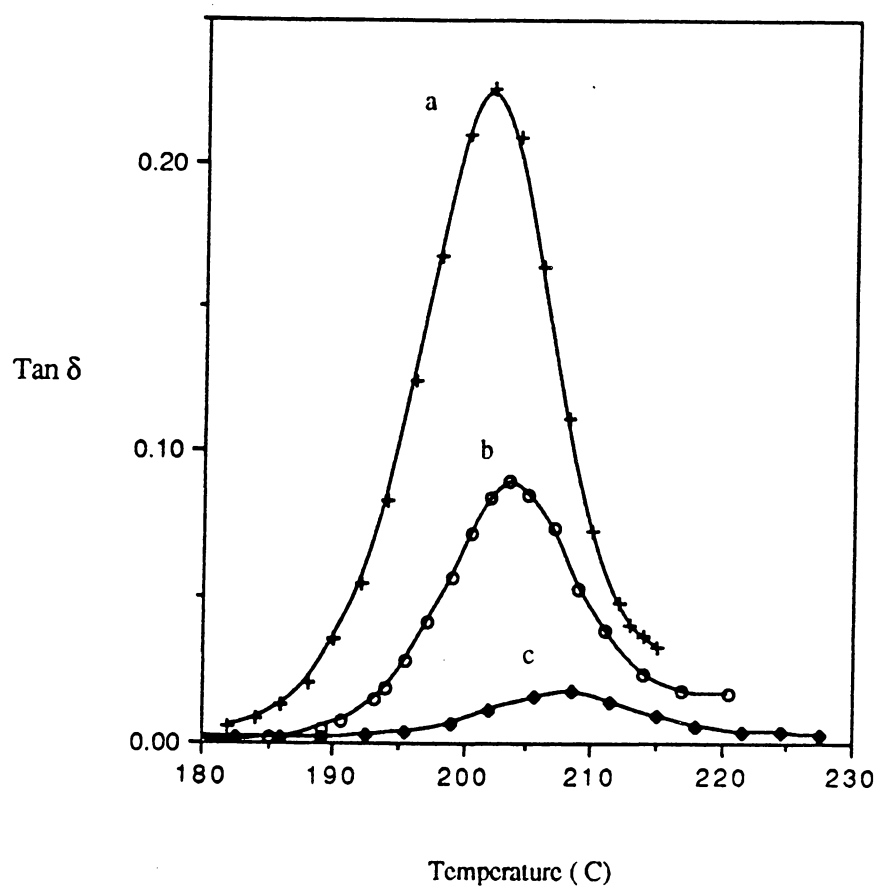

Figure 4.24. Comparison of the dielectric loss factor (tan δ) -temperature curves at 1 kHz for PSF : a). neat film , b). 1.8 μm film on smooth aluminum surface, and c). 2.0 μm film on porous aluminum surface.

In Figure 4.22 and 4.23 the dielectric thermal analysis results are given for all films on the sm-Al surface and on the p-Al surface respectively. The limit of detection for these films was about 6000 Å where the sample can no longer withstand the ac voltages being applied. In Figure 4.24, the dielectric loss factor, tan δ, at 1 kHz is plotted against temperature for both the neat PSF film (sample A) and the PSF coatings shown in Figure 4.21 (these were samples B3 and C2). The coatings show a different response than that of the neat film, both in the magnitude of tan δ values and in the glass transition temperatures. These results are consistent with the dynamic mechanical analysis. The lower tan δ values for the coatings are due to the lower volume fractions of polymer present with the coatings (see Figure 4.6); while the higher T_g values for the coatings are thought to arise again from an interphase response where adhesion mechanisms lead to a higher T_g for the interphase (see Section 4.1.2 and Figure 4.2) region.

In addition to the differences between the neat film and coatings, there was a difference in the dielectric relaxation behavior between the coatings themselves. Referring to Figure 4.21, one notes that the difference between the films cast onto the p-Al surface and those cast onto the sm-Al surface is the whisker layer present when the p-Al is the coating substrate. Yet, from the dielectric thermal analysis, one finds three distinct differences between the dielectric response of the coatings: 1) the magnitudes of tan δ are always lower for the films on the p-Al surface, 2) the glass transition temperature is always highest for the coatings on the p-Al surface, and 3) the breadth of the glass transition is always broadest for the coatings on the p-Al surface. In the dynamic mechanical analysis the latter two points were not observed while the first point was only observed at lower frequencies. It would therefore seem that the dielectric experiment is more sensitive to interphase anomalies than was the dynamic mechanical.

Considering the first point, the lower values of tan δ at the T_g, tan δ_{Tg}, for the coatings on the p-Al surface was interesting since one would expect higher tan δ_{Tg} values for the films on the p-Al surface compared to the films on the sm-Al surface. This is because the magnitude of tan δ

generally increases as one increases the volume fraction of the relaxation phase, and from Figures 4.20 and 4.21 one notes that the volume fraction of PSF is greater for the coatings on the p-Al surface due to the added whisker layer. However, the lower magnitudes for the coatings on the p-Al surface could be interpreted as resulting from higher interfacial shear strengths (τ_{12}). This is consistent with the work done by Chua (Figure 4.7), where there was an inverse relationship between τ_{12} and tan δ_{Tg} for the glass fiber reinforced polyester systems.

With respect to the second point, -the higher T_g values for the films on the p-Al surface- these differences are again attributed to the larger extent of interphase region present for the coatings on the p-Al surface; hence, the interphase influence is greatest with these samples where the surface area of substrate to volume of polymer ratios are high.

In Table 4.5, the glass transition temperatures and tan δ_{Tg} values for all samples are given at both a low and high frequency; in addition, Figure 4.25 summarizes these data at 1 KHz for both coating types.

Considering the last point, the broad transitions that arise for the films on the p-Al surface (which is especially pronounced for the thinner films) can be attributed to a larger dispersion of relaxation times. Since each characteristic relaxation time is a function of the fields of force that control that particular relaxation mechanism, a broader distribution of relaxation times for the PSF on the p-Al surface is not surprising. On the p-Al surface there probably exist more surface heterogeneities (both physical and chemical) due to the anodization; where each of these "heterogeneous" or "active" site has associated with it a particular field of force having the potential to alter the relaxation behavior of an adsorbed species.

Arrhenius activation energies were calculated from the frequency dependence of the glass transition temperature. These results are listed in Table 4.6 for all the samples studied. The activation is again different between the neat films and coatings and between the coatings

Table 4.5. Glass transition temperatures and tan δ_{Tg} values for PSF of various film states as determined by dielectric thermal analysis.

NEAT PSF FILM

Tg	Frequency (kHz)	tan δ_{Tg}
202.0	1.0	0.23
219.0	100.0	0.25

PSF FILM ON POROUS-Al

1 kHz			50 kHz		
film thickness(μm)*	Tg	tan δ_{Tg}	film thickness (μm)*	Tg	tan δ_{Tg}
0.2	211.5	0.0097	0.2	225.5	0.012
2.0	209.0	0.017	2.0	221.5	0.024
5.0	210.0	0.034	5.0	223.5	0.060

PSF FILM ON SMOOTH-Al

1 kHz			10 kHz		
film thickness(μm)	Tg	tan δ_{Tg}	film thickness (μm)	Tg	tan δ_{Tg}
0.8	205.0	0.030	0.8	212.0	0.041
1.4	205.0	0.087	1.4	213.0	0.160
1.8	203.5	0.092	1.8	211.5	0.170

* film thickness of the overlayer only

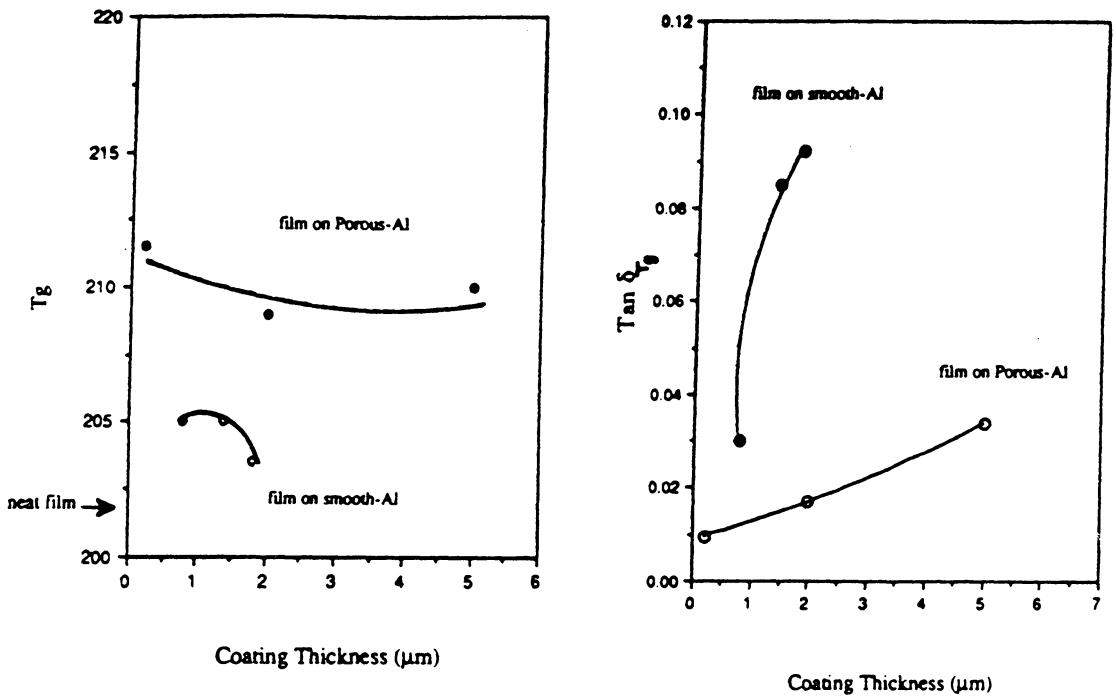

Figure 4.25. a.) Variation of the glass transition temperature with coating thickness for films on the sm-Al and p-Al surface b) Variation of the tan δ_{Tg} with coating thickness for film on the sm-Al and p-Al surface.

Table 4.6. Arrhenius activation energies for PSF coatings on a smooth and porous aluminum surface of various coating thicknesses - as determined by dielectric thermal analysis.

On Smooth Al		On Porous Al	
Film Thickness (μm)	ΔH* (kJ/mol)	Film Thickness (μm)	ΔH* (kJ/mol)
0.8	699 ± 43	0.2	644 ± 48
1.4	563 ± 19	2.0	631 ± 37
1.8	558 ± 44	5.0	606 ± 33

* neat film : $\Delta H^* = 530 \pm 30$ (kJ/mol)

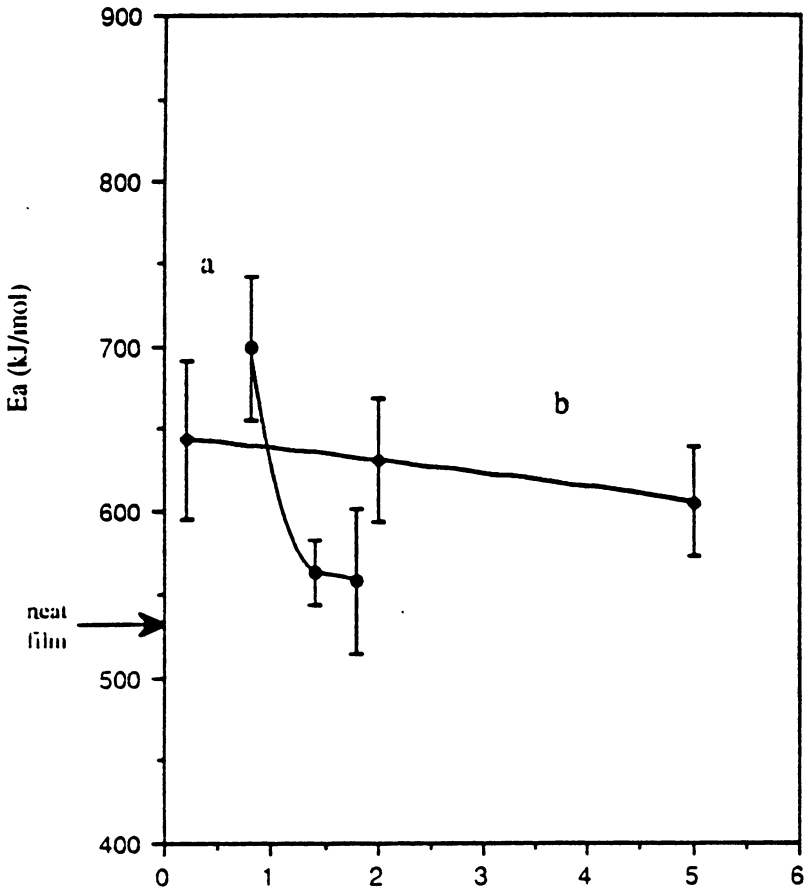

Figure 4.26. Arrhenius activation energy versus film thickness for PSF on : a). smooth aluminum surface , and b). porous aluminum surface.

themselves -- as was observed in the dynamic mechanical analysis. Within a sample series (i. e. B or C series) there is also a difference in the activation energy, with the activation energy decreasing as film thickness increases. In Figure 4.26 the Arrhenius activation energy is plotted as a function of film thickness for films on the p-Al surface and sm-Al surface. These data were obtained from the slope of Log (f) versus 1/T plots (as shown in Figure 4.19), while the errors given are for the standard deviation in the corresponding slopes. From Figure 4.26 it is evident that there is a decrease in the activation energy which approaches that of the neat (530 kJ/mole) at 1.4 μm for the PSF film on the sm-Al surface. The PSF coating on the p-Al substrate seems fairly independent of film thickness even out to thickness of 5 μm; yet, there was a higher activation energy than for the coatings on the sm-Al surface or the neat film. Since all samples were annealed prior to analysis, the differences in the Arrhenius activation energy with coating thickness suggest a gradient of relaxation properties near the interphase region.

4.5 Summary and Conclusions

The goal of this study was to correlate the observed relaxation properties of thin PSF coatings with the chemical composition and topographical features of the aluminum substrate. From this investigation the following highlights were noted:

1. The aluminum surface that was pretreated by just vapor degreasing was smooth whereas the phosphoric anodized surface was porous with pore diameters of about 100 nm.
2. The XPS results revealed that the interfacial chemistry between the polysulfone and the aluminum oxide surface was the same for both the sm-Al surface and p-Al surface.
3. The SEM results showed that the PSF uniformly coated on the smooth substrate, whereas the PSF migrated into the porous oxide on the porous aluminum substrate and resulted in whisker like structures.

4. Dynamic mechanical analysis revealed that the activation energy was highest for the films on the p-Al surface, while glass transition temperatures were different for these films (as compared to those on the sm-Al surface) only at low frequencies.
5. In the dielectric analysis, the dielectric loss factor was greatest for the neat film and lowest for the film on the porous-aluminum surface and the breadth of the alpha transition was broadest for the PSF coating on the porous aluminum surface.
6. The glass transition temperatures for the polysulfone were highest for the films on the porous aluminum surface for all samples and at all frequencies in the dielectric analysis; however only at low frequencies was this true in the dynamic mechanical analysis.
7. The Arrhenius activation was highest for the films on the porous-aluminum surface for both the dynamic mechanical and dielectric experiments.
8. The dielectric experiments revealed a possible gradient of relaxation properties - namely in the Arrhenius activation energy - for both coatings.
9. The influence of surface topography on the viscoelastic relaxation properties was most significant in the dielectric experiments versus the dynamic mechanical experiments. This was true even of the thicker films studied in the dielectric experiments.

These conclusions though cannot dismiss that other possible explanations exist for the anomalous behaviour of the PSF coatings such as space charge effects within the coatings and chemical interactions at the interface.

Space charge effects have been described for metal/atactic polystyrene coatings which results in a space charge region that extends 2-4 μm into the bulk of the polymer from the metal-polymer interface (28). This in part could explain why the dielectric experiments revealed a greater difference - in the relaxation behavior between the PSF coatings - than the dynamic mechanical experiments. Here, an internal charge within the coating layers could lead to a greater imobilization of dipoles; therfore, when comparing the relaxation properties between the coatings on the sm-Al

surface to those on the p-Al surface, one would expect differences on the premise that there is a larger surface area for the films on the p-Al surface and hence a greater extent of space charge region. For this reason the applied voltage in the dielctric experiments was controled in order to provide a set of consistent results.

In addition, Inverse Gas Chromatography studies in our laboratories have revealed the basic nature (in the Lewis acid/base sense) of polysulfone (29), which could lead to acid/base interactions between the PSF coating and the partially acidic anodized aluminum surface; although, the XPS results seemed to have dismissed this possiblity since there was no shifting in the binding energies with surface pretreatment - though this interpretation is complicated by the Argon ion sputtering done in these experiments. Further studies on the surface free energies and acid /base nature of the polymer and aluminum pretreated surfaces would be required in order to understand the role of any chemical aspects in this study.

These points only serve to show that the differences in relaxation behavior between the film and coatings themselves cannot be fully understood by these simple experiments and that more controlled studies could be pursued to further elucidate those factors which affect the viscoelastic properties of adhesives near the interphase.

4.6 Appendix

4.6.1 The Relaxation Time, τ

The time dependent nature of polymers arises from the fact that even in the solid state polymer molecules are highly mobile. Thus, when a stress (electrical or mechanical) is imposed onto a polymeric sample conformational rearrangements occur within the sample that establish new equilibrium arrangements to respond to the applied stress.

The rate of change to the new equilibium state can be represented by linear relaxation theory (a pseudo first order process). For the single relaxation time model, if δ is a measure of the deviation from equilibrium then the rate of change to the new equilibrium state can be written as

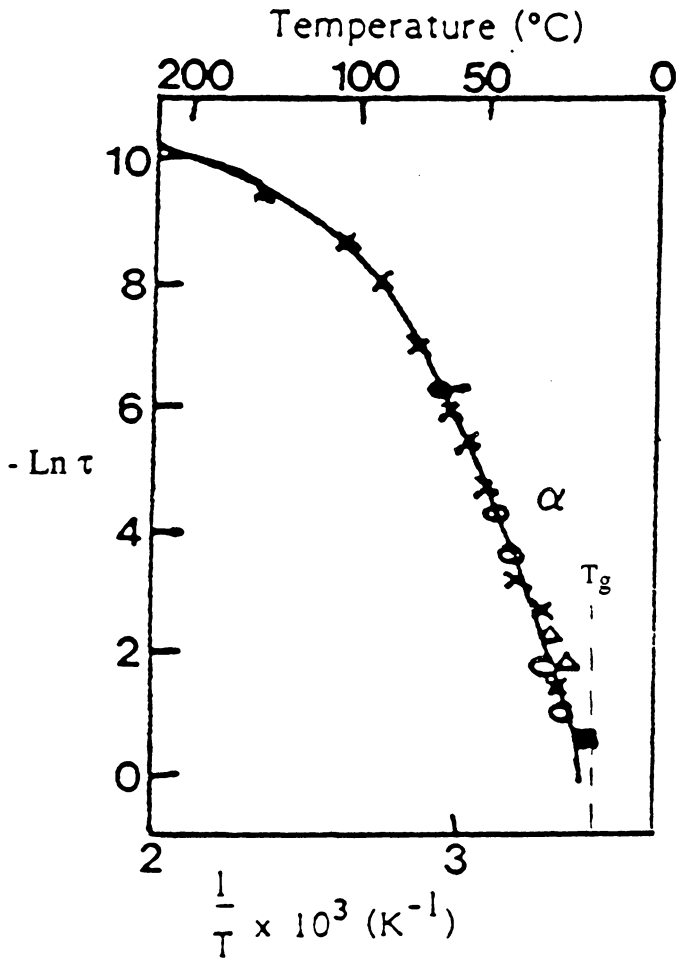

Figure 4.27. Temperature dependence of the relaxation time t for relaxation processes in the α-relaxation region. Shown here for poly(methyl acrylate) (18).

$$\text{Rate} = \partial\delta/\partial t = k\delta = \delta/\tau \qquad [4\text{-}2]$$

where τ is the relaxation time. Macroscopically it is the viscoelastic material properties (i.e. E', E", J(t), ε', . . .) that are changing with time, and Equation [4-2] can be used to define the time dependence of these properties as the system approaches equilibrium. This is done by simply substituting the appropriate equilibrium value for the experiment under study and then solving the above differential equation -which is analogous to solving for the rate law in chemical kinetics (30).

4.6.2 Temperature Dependence of τ

Experimentally, one finds that there is a temperature dependence of τ. For the relaxation processes occurring in the α-transition this dependence is represented as shown in Figure 4.26 for poly(methyl acrylate). One notes that at higher temperatures the plot is fairly linear, while at lower temperatures, as one approaches the Tg of the material (as would be obtained in an infinitely slow dilatometery study), the plot becomes curved. Each of these regions will be considered individually. For now one notes from Figure 4.27 that the effect of changing temperature is a logarithmic shift in τ. This shift, designated as a_T, results in the following definition

$$\ln a_T = \ln \tau_2 - \ln \tau_1 = \ln \tau_2/\tau_1 \qquad [4\text{-}3]$$

4.6.2.1 Arrhenius Region

Considering Figure 4.27, if one is in the linear region (which is true of behavior in the glassy state) the temperature dependence can be written as

$$\ln \tau_2/\tau_1 = \ln a_T = A\,(1/T_2 - 1/T_1) \qquad [4\text{-}4]$$

where A is simply the slope of the line or linear portion of the curve. Moreover, the relaxation processes in this region are thermally activated processes and by analogy with rate theory one can define A as

$$A = \Delta H^*/R \qquad [4\text{-}5]$$

where ΔH^* is the activation energy for the relaxation process. Hence, we see that the temperature dependence of the shift factor in the linear region is given as

$$a_T = \exp(\Delta H^*/RT) \qquad [4\text{-}6]$$

This expression gives both the temperature dependence of τ and the frequency dependence (f) of data on temperature plane (since $t=1/2\pi f$).

4.6.2.2 WLF Region

In the curved region (which is true of behavior in the glass to rubber transition) the shift factor is found to follow the empirical Williams, Landel and Ferry (WLF) equation. This equation is given as

$$\ln a_T = -2.3\left[\frac{c_1(T - T_0)}{c_2 + (T - T_0)}\right] \qquad [4\text{-}7]$$

where the parameters c_1 and c_2 are constants for a given polymer and reference temperature, T_0. In addition, one can define an **apparent** activation energy for a WLF process since ΔH^* is given as

$$\Delta H^* = R\, d(\ln a_T)/d(1/T) \qquad [4\text{-}8]$$

Therefore, differentiation of Equation [4-7] leads to

$$\Delta H^* = \frac{Rc_1c_2T^2}{(c_2 + T - T_0)^2} \qquad [4\text{-}9]$$

However, there is question to the validity of such a variable (ΔH^*) since WLF relaxation processes are <u>not</u> thermally activated processes. Other molecular theories of relaxation (those of Bueche, Cohen and Turnbull) have derived the WLF equation and the basic underlying idea in these theories is that the relaxation processes at temperatures close to T_g (WLF region) are cooperative motions that arise only when there is a local free volume that exceeds some critical value f_c (30). Thus, unlike the thermally activated processes that occur in the linear region of Figure 4.26, the relaxation processes in the curved region of Figure 4.26 are free volume activated processes. Thus, an activation energy of the WLF type is questionable since the basic relationships of rate theory are not followed.

4.6.3 Relaxation Time Distributions

A polymeric solid can rarely be characterized by a single relaxation time. Generally, it is a distribution of relaxation times that lead to the viscoelastic behavior of polymeric materials. If one were to consider that each relaxation time followed Arrhenius behavior then Equation [4-6] could be rewritten as

$$\tau = \tau_0 \exp(\Delta H^*/RT) \qquad [4\text{-}10]$$

where τ_0 is the relaxation time at infinite temperature. From Equation [4-10], a distribution of τ values at a temperature T may arise in three ways: (a) from a distribution of τ_0 values, ΔH^* being the same for every relaxation process; (b) from a distribution of ΔH^* values, τ_0 being the same for each process; (c) more generally from a distribution of both ΔH^* and τ_0 values (31).

Case (a) would be expected to arise for the alpha relaxation exhibited by amorphous polymers; where a large number of polymer chain segments of varying size and complexity would be involved in the relaxation with each segment having a different natural frequency or τ_0. In addition, on an average each moving segment would be surrounded by similar intermolecular fields of force which is tantamount to having the same activation energy. Case (b) would apply to the relaxation behavior of an assembly of molecules of similar size where each molecule or segment was surrounded by a different field of force (for example composites), and case (c) would generally apply to the behavior of semicrystalline polymers. While case (a) results in a distribution of relaxation times whose shape is independent of temperature, cases (b) and (c) will result in a distribution of relaxation times whose shape will be temperature dependent.

For a given polymer system with a distribution of relaxation times following case (c) above, the calculated activation energy from an Arrhenius plot will be an average activation energy formally defined as

$$\Delta H^* = \langle 1/\Delta h^* \rangle^{-1} \qquad [4\text{-}11]$$

where Δh^* is a characteristic activation energy for a given relaxation mechanism.

REFERENCES

1. Mittal, K. L., Polym Eng. Sci., **17**(7), 467 (1977).
2. Brewis, D. M. and Briggs, O., "Industrial Adhesion Problems", Wiley, New York, 1985.
3. Van Ooij, W. J., in Physicochemical Aspects of Polymer Surfaces, Mittal, K. L. (ed.) Plenum Press, New York, Vol. 2, 1983.
4. Venables, J. D., Appl Surf. Sci., **3**(88), 1979.
5. Packham, D.E., "Adhesion Aspects of Polymer Coatings", Plenum Press, p. 19, 1983.
6. Theocaris, P. S. and Spathis, G. D., J. Appl. Polym. Sci., **27**, 3109, 1982.
7. Yim, A., Chalal, R. S. and St. Pierre, L. E., J. Coll. Interface Sci., **43**, 583, 1973.
8. Peyser, P., Polym. Plast. Technol. Eng., **10**(2), 117, 1978.
9. Knollman, G. C. and Harthog, J. J., J. Appl. Phys., **53**(3), 1516, 1982.
10. Knollman, G. C. and Harthog, J. J., J. Appl. Phys., **53**(8), 5514, 1982.
11. Knollman, G. C., Int. J. Adhesion and Adhesives, **5**(3), 137, 1985.
12. Knollman, G. C. and Harthog, J. J., J. Adh., **17**, 251 (1985).
13. Crowley, J. L. and Jonath, A. D., "Adhesion and Absorption of Polymers", Lee,M.L. H. (ed.), Plenum Press, New York, 1979.
14. Peyser, P. and Bascom, W. D., J. Macro. Sci. Phys., **B13**(4), 597 (1977).
15. Wilkes, G. L. and Tant, M. R., Poly. Eng. Sci., **21**(14), (1981).
16. Aklonis, J. J. and Kovacs, A. J., "Contemporary Topics in Poymer Science", Shen, M. (ed.), Plenum Press, New York, 19.
17. Wetton, R. E., Am. Lab., January 1986.
18. Wetton, R. E., "Developments in Polymer Characterization", Vol 5, Dawkins, J. V. (ed.), Elsevier, New York, 1986.
19. Sheridan, M. M., Ph.D. Dissertation, Virginia Polytechnic Institute and State University, October, 1986.
20. Chua, P. S., SAMPE Quarterly, **18**(3), 10, 1987.
21. Polymer Laboratories' Dielectric Thermal Analyzer Instruction Manual, Polymer Laboratories Ltd., England, 1986.
22. Wetton, R. E., Polymer Surfaces and Interfaces Symposium, Durham, U. K., April 1985.

23. Atkins, P W., "Physical Chemistry, Oxford University Press", Great Britan, 1978.

24. Derjaguin, B. U., Trans. Fara. Soc., **1**, 98,1970.

25. Bascom, W. D., J. Coll. Interface Sci., **66**(3), 559., 1978.

26. Adamson, A. W., "Physical Chemistry of Surfaces", 4th Ed., Wiley, New York, 1982.

27. Nielsen, L. E., "Mechanical Properties of Polymers and Composites", Vol. 1, Dekker, New York, 1974.

28. Pochan, J. M. and Gibson, H. W., J. Electrostatics, **8**, 183 , 1980.

29. Bolvari, A., M. S. Thesis, Virginia Polytechnic Institute and State University, 1988.

30. McCrum, N. G., Read, B., E. and William, G., "Anelastic and Dielectric Effects in Polymeric Solids", Wiley, New York, 1967.

31. Read, B. E. and Williams, G., Trans. Fara. Soc., **57**, 1979, 1961.

The vita has been removed from the scanned document